DESIGN, CHARACTERIZATION AND INTEGRATION OF ELECTRICALLY SMALL ANTENNAS

Chua Chee Parng
(B. Eng. (*Hons*) NUS)

A THESIS SUBMITTED
FOR THE DEGREE OF MASTER OF ENGINEERING
DEPARTMENT OF ELECTRICAL AND COMPUTER ENGINEERING
NATIONAL UNIVERSITY OF SINGAPORE
2004

To My Family.

Acknowledgements

There are many people who have helped me throughout my Masters of Engineering (M.Eng.) project and I would like to take this opportunity to express sincerest gratitude to them. Firstly, I would like to thank my NUS supervisor, Professor Leong Mook-Seng for his many suggestions and constant support during this research. I am grateful to him for all the advices he had given me during these two years, as I feel he always had the interest of his students at heart. I am also thankful to Associate Professor Ooi Ban-Leong for the advise and help in chasing vendors for the dielectric resonators I needed so much for fabrication.

Secondly, my co-supervisor Dr. Popov Alexandre Pavlovich from Institute of Microelectronics (IME) has given me tremendous help and insights to make the completion of my master project possible. On several occasions when I seek help from him due to difficulties in designing my antenna, he has been very patient to me. I have learned much from him and the insights he has shared with me, help in many ways to achieve good simulation and measurement results.

Next, I would like to thank Mr. Sing Cheng-Hiong from Microwave Research Laboratory (MRL) and staffs from Microwave Teaching Laboratory (MTL) for their efficient technical support.

Lastly, I would like to thank the friends I have made over these two years. I had the pleasure to work with many fellow Masters and PhD students from MRL. They have been great advisors and supporters in times of difficulties. Among them, Mr. Ng Tiong-Huat and Mr. Ewe Wei-Bin have been pivotal in my understanding of the Finite Element Method (FEM). I am also thankful to my constant laboratory companion Mr. Tham Jin-Yao for his humor, help and advise. He is probably one of the most helpful, dependable and trustworthy friend I have met. I would also like to thank Miss Ang Irene for her help, encouragement and companionship during the most difficult period of my research. She can always make me laugh and has been the brightest spark when times seem gloomy. Without her, my research life would have been more difficult.

Table of Contents

Acknowledgements **iii**

Table of Contents **iv**

Summary **vii**

List of Figures **xi**

List of Tables **xii**

1 Introduction **1**
1.1 Background 2
1.2 Project Objectives 4
1.3 Outline of Concept 5
1.4 Thesis Layout 6
1.5 Original Contributions 7

2 Literature Review **8**
2.1 Dielectric Resonator Antennas Supported by 'Infinite' and Finite Ground Planes 8
2.2 Packaging Technique for Gain Enhancement of Electrically Small Antenna designed on Gallium Arsenide 9
2.3 A Low-Profile Rectangular Dielectric Resonator Antenna 10
2.4 Overview of Analytical Models for Isolated Dielectric Resonator . . . 11
2.5 Computation of Cavity Resonances Using Edge-Based Finite Elements 12

3 Analytical Models for Dielectric Resonator **14**
3.1 Magnetic Wall Model 15
3.1.1 Different excitation modes 16
3.1.2 Resonant frequencies 18
3.1.3 Equivalent magnetic surface currents 19
3.1.4 Field Configuration 20
3.2 Dielectric Waveguide Model 22
3.2.1 Field Configuration 22
3.2.2 Resonant Frequency 23

3.2.3 Q-Factor 23
3.3 Empirical Equations derived from Rigorous Methods 24
3.3.1 Resonant Frequency of Isolated Cylindrical DRs 24
3.3.2 Bandwidth of Isolated Cylindrical DRs 25
3.3.3 Radiation Q-Factor and Eigenvalues of Various Modes 27

4 Full-Wave Analysis of Dielectric Resonator using Finite Element Method 30
4.1 Problem Description 31
4.2 Variational Formulation 32
4.3 Finite Element Numerical Procedures 34
4.3.1 Domain Discretization 34
4.3.2 Elemental Interpolation 36
4.3.3 Tangential Vector Finite Elements 38
4.3.4 Evaluation of Elemental Matrices 40
4.4 Software Implementation 42
4.4.1 Software Overview 42
4.4.2 Code Descriptions 43

5 Design Methodology of the Dielectric Resonator Antenna 46
5.1 Introduction 46
5.2 Conventional DRAs 47
5.3 Fundamental Limitations of a small antenna 48
5.4 Antenna measurement for small antenna 49
5.5 Proposed Antenna Structures 51
5.5.1 Linear and Circular-Polarized Antennas 51
5.5.2 Design Procedures 53

6 Results and Discussions 62
6.1 Comparison of Eigenvalues 62
6.1.1 Test Case: Empty Box 62
6.1.2 Dielectric Resonator in Cavity 65
6.2 Validity of models 69
6.3 Dielectric Resonator Antennas Fabricated 72
6.3.1 Comparison of Cylindrical and Rectangular Dielectric Resonator Antennas 72
6.3.2 Comparison of Antennas using High and Low Permittivity Dielectric Resonator 85
6.3.3 Comparison of Linear and Circular-Polarized Cylindrical Resonator Antennas 93
6.3.4 Comparison of Two Methods for Measurement of DRAs Radiation Efficiency 102

7 Conclusions and Recommendation for future work **106**
7.1 Conclusions 106
7.2 Limitations of TVFE method 107
7.3 Recommendation for future work 108

References **109**

A Derivations of a_j^e, b_j^e, c_j^e and d_j^e **113**
A.1 Determinant of any order n 113
A.2 Comparison of Coefficients 115

B Matlab Codes implementing FEM **121**
B.1 Main 121
B.2 Define global edges 125
B.3 Global edges for each elements 127
B.4 Edges on the boundary 129

Summary

In this thesis, electrically small dielectric resonator antennas have been designed, characterized and fabricated successfully. A robust and reliable method using Tangential Vector Finite Element (TVFE) method has been proposed to compute eigenvalues of an isolated dielectric resonator (DR). To obtain better insight and appreciation of the isolated resonator problem, a FEM code (TVFE) was developed from scratch and the results derived from it are compared with those of Ansoft High Frequency Structure Simulator (*HFSS*). Accurate characterization of the eigenmodes is critical to achieve high radiation efficiency and can provide a good initial guess to the antenna's operating frequency. Predicted eigenvalues using the written codes are within 1% of error from measured values.

When the feed design is incorporated, *HFSS* is used to optimize the antenna. The proposed feed structure for linear polarization comprised of a complementary pair of magnetic dipole and magnetic loop [1], modified to exclude the ground plane. For circular polarization, the feed structure comprised of a meandering magnetic dipole. This compact structure overcomes the impact of a finite "ground plane" and has a unidirectional radiation pattern away from the ground plane. Hence, the ground plane's impact on the antenna parameters is significantly reduced allowing a compact design of the antenna system. The feed structure has metallization on all sides to prevent possible electromagnetic interference from the antenna on the RF circuitry. A probe is then used to excite the feed structure beneath the dielectric resonator.

Subsequently, the dielectric resonator antennas are fabricated and measured. Comparison is first carried out between a cylindrical and rectangular DR antenna to investigate their potential advantages. Next, a DR antenna with high permittivity values of 38.5 is fabricated and compared with one using a permittivity value of 10.2. Finally, a circular-polarized DR antenna is designed, fabricated and compared with the linear-polarized case.

List of Figures

3.1 Division of fields associated with a dielectric resonator into an interior and an exterior region . . . 14
3.2 Geometry of a cylindrical DR antenna . . . 15
3.3 Side view of the cylindrical DR antenna . . . 15
3.4 Fields inside an isolated cylindrical DR for $TE_{01\delta}$ mode . . . 16
3.5 Fields inside an isolated cylindrical DR for $TM_{01\delta}$ mode . . . 17
3.6 Fields inside an isolated cylindrical DR for $TM_{11\delta}$ mode . . . 17
3.7 Fields inside an isolated cylindrical DR for $TM_{21\delta}$ mode . . . 17
3.8 Infinite and finite dielectric waveguide . . . 22
3.9 Radiation Q-factor of a dielectric disc with radius a, height h and dielectric constant $\epsilon_r = 10.2$. . . . 28
3.10 Resonant wavenumbers of different modes for an isolated cylindrical DR with radius a, height h and dielectric constant $\epsilon_r = 10.2$. . . . 28
3.11 Radiation Q-factor of a dielectric disc with radius a, height h and dielectric constant $\epsilon_r = 38.5$. . . . 29
3.12 Resonant wavenumbers of different modes for an isolated cylindrical DR with radius a, height h and dielectric constant $\epsilon_r = 38.5$. . . . 29

4.1 Dielectric resonator enclosed by a cavity . . . 31
4.2 Linear tetrahedral element . . . 36
4.3 Tetrahedral element . . . 39
4.4 Example of element.txt generated using mesh generator GID 7.2 . . . 43
4.5 Example of fedge.txt generated from FEDGE.M . . . 44
4.6 Example of gedge.txt generated from GEDGE.M . . . 44

5.1 Examples of some conventional DRAs . . . 47
5.2 Small antenna and connecting cable . . . 49
5.3 Schematics of the linear-polarized DRA . . . 52
5.4 Schematics of the circular-polarized DRA . . . 52
5.5 Coplanar Waveguide Feed . . . 53
5.6 Desired Impedance Locus . . . 54

5.7 Variation of input impedance as a function of the magnetic dipole length L_s. Frequency increases clockwise with step of 0.05GHz. Center of Loop : (1.35,0), Rs = 7.15mm, d = 7.35mm 55
5.8 Variation of input impedance as a function of parameter d. Frequency increases clockwise with step of 0.05GHz. Center of Loop = (1.35,0), Rs = 7.15mm, Ls = 4.094mm 56
5.9 Variation of input impedance as a function of the magnetic loop radius R_s. Frequency increases clockwise with step of 0.05GHz. Center of Loop = (1.35,0), Ls = 4.094mm 56
5.10 Variation of input impedance as a function of the magnetic loop center. Frequency increases clockwise with step of 0.05GHz. Ls = 4.094mm, Rs = 7.15mm, d = 7.35mm 57
5.11 Variation of input impedance as a function of the probe position. Frequency increases clockwise with step of 0.05GHz. Center of Loop = (1.35,0), Ls = 4.094mm, Rs = 7.15mm, d = 7.35mm 57
5.12 Variation of input impedance as a function of L_s. Frequency increases clockwise with step of 0.05GHz. Probe position = (5,0), L_1 = 5.735mm, d = 7.862mm 59
5.13 Variation of input impedance as a function of L_1. Frequency increases clockwise with step of 0.05GHz. Probe position = (5,0), L_s = 12.394mm, d = 7.862mm 59
5.14 Variation of input impedance as a function of d. Frequency increases clockwise with step of 0.05GHz. Probe position = (5,0), L_s = 12.394mm, L_1 = 5.735mm 60
5.15 Variation of input impedance as a function of probe position. Frequency increases clockwise with step of 0.05GHz. Ls = 12.394mm, L_1 = 5.735mm, d = 7.862mm 60
5.16 Axial ratio calculation 61

6.1 Mesh generated for empty cavity using *GiD 7.2* 63
6.2 Geometry of a Dielectric Resonator positioned in the center of a metallic box drawn using *Gmsh* 65
6.3 Surface Mesh generated for the metallic box enclosing a dielectric resonator 65
6.4 Closed-up view of surface mesh generated for the dielectric resonator 66
6.5 Closed-up view of volume mesh generated for the dielectric resonator 66
6.6 Steps in the mesh refinement process 67
6.7 Design schematics for linear-polarized cylindrical DRA 73
6.8 Design schematics for linear-polarized rectangular DRA 74
6.9 Cylindrical DRA simulated using Ansoft HFSS 75

6.10 Rectangular DRA simulated using Ansoft HFSS 75
6.11 E-fields within the cylindrical dielectric resonator simulated using Ansoft HFSS (4.20GHz) 76
6.12 E-fields within the rectangular dielectric resonator simulated using Ansoft HFSS (3.64GHz) 76
6.13 H-fields within the cylindrical dielectric resonator simulated using Ansoft HFSS (4.20GHz) 76
6.14 H-fields within the rectangular dielectric resonator simulated using Ansoft HFSS (3.64GHz) 76
6.15 Simulated current density for cylindrical DR antenna using Ansoft HFSS (4.20GHz) 77
6.16 Simulated current density for rectangular DR antenna using Ansoft HFSS (3.64GHz) 77
6.17 Electrical length (in λ_g) of the feed design for linear-polarized cylindrical DR antenna (4.20GHz) 78
6.18 Electrical length (in λ_g) of the feed design for linear-polarized rectangular DR antenna (3.64GHz) 78
6.19 Top view of feeding substrate for Cylindrical Dielectric Resonator Antenna (Linear-Polarized) fabricated 79
6.20 Three-dimensional view of Cylindrical Dielectric Resonator Antenna (Linear-Polarized) fabricated 79
6.21 Top view of feed substrate for Rectangular Dielectric Resonator Antenna (Linear-Polarized) fabricated 80
6.22 Three-dimensional view of Rectangular Dielectric Resonator Antenna (Linear-Polarized) fabricated 80
6.23 Photo showing the complementary pair of magnetic loop and magnetic dipole for linear-polarized antenna 81
6.24 Measured return loss for Cylindrical Dielectric Resonator Antenna, $\epsilon_r = 10.2$ (Linear-Polarized) 82
6.25 Measured return loss for Rectangular Dielectric Resonator Antenna, $\epsilon_r = 10.2$ (Linear-Polarized) 82
6.26 Measured far-field radiation pattern at 4.20 GHz for Cylindrical Dielectric Resonator Antenna (Linear-Polarized) 84
6.27 Measured far-field radiation pattern at 3.64 GHz for Rectangular Dielectric Resonator Antenna (Linear-Polarized) 84
6.28 Design schematics for linear-polarized cylindrical DRA using high permittivity resonator ($\epsilon_r = 38.5$) 86
6.29 Linear-polarized antenna ($\epsilon_r = 38.5$) simulated using Ansoft HFSS . . 87

6.30 Simulated E-fields within the antenna ($\epsilon_r = 38.5$) using Ansoft HFSS (3.60GHz) 87
6.31 Simulated H-fields within the antenna ($\epsilon_r = 38.5$) simulated using Ansoft HFSS (3.60GHz) 87
6.32 Simulated current density for antenna ($\epsilon_r = 38.5$) using Ansoft HFSS (3.60GHz) 88
6.33 Top view of feeding substrate for Cylindrical Dielectric Resonator Antenna ($\epsilon_r = 38.5$) fabricated 89
6.34 Three-dimensional view of Cylindrical Dielectric Resonator Antenna ($\epsilon_r = 38.5$) fabricated 89
6.35 Measured return loss for Cylindrical Dielectric Resonator Antenna ($\epsilon_r = 38.5$) 91
6.36 Measured far-field radiation pattern at 4.0 GHz for Cylindrical Dielectric Resonator Antenna ($\epsilon_r = 38.5$) 92
6.37 Design schematics for circular-polarized cylindrical DRA 94
6.38 Circular-polarized antenna simulated using Ansoft HFSS 95
6.39 E-fields within the circular-polarized antenna simulated using Ansoft HFSS (3.88GHz) 95
6.40 H-fields within the circular-polarized antenna simulated using Ansoft HFSS (3.88GHz) 95
6.41 Simulated current density for circular-polarized antenna using Ansoft HFSS (3.88GHz) 96
6.42 Electrical length (in λ_g) of the feed design for circular polarization . . 96
6.43 Top view of feeding substrate for Cylindrical Dielectric Resonator Antenna (Circular-Polarized) fabricated 97
6.44 Three-dimensional view of Cylindrical Dielectric Resonator Antenna (Circular-Polarized) fabricated 97
6.45 Photo showing the meandering magnetic dipole for circular-polarized antenna 98
6.46 Measured return loss for Cylindrical Dielectric Resonator Antenna (Circular-Polarized) 99
6.47 Measured axial ratio in the broadside direction against frequency . . 100
6.48 Measured radiation patterns for the circular-polarized antenna at 4.20 GHz 101
6.49 Measured antenna gain in the broadside direction against frequency . 101
6.50 Set-up for measuring antenna radiation efficiency using the Wheeler cap method 104

List of Tables

4.1 Edge definition for tetrahedral element 39

6.1 Eigenvalues (k_o, cm^{-1}) for an empty 5.339cm × 5.339cm × 5.339cm cavity 64
6.2 Parameters used to generate mesh of the dielectric resonator in cavity 66
6.3 Eigenvalues computed in the mesh refinement process 68
6.4 Effects of cavity's size on eigenvalues of the dielectric resonator ($\epsilon_r = 79.7, a = 5.145mm, h = 4.51mm$) 69
6.5 Comparison of resonant frequency among DWM, simulation, TVFE method and measurement (ϵ_r=90) 70
6.6 Comparison of eigenvalues obtained using Tangential Vector Finite Element (TVFE) Method and other conventional methods 71
6.7 Specifications of resonator and substrate used 72
6.8 Summary of near-field results for cylindrical and rectangular dielectric resonator antennas 82
6.9 Summary of measured radiation patterns 83
6.10 Specifications of resonator and substrate used 85
6.11 Summary of near-field results for high and low permittivity dielectric resonator antennas 90
6.12 Summary of measured radiation patterns 92
6.13 Specifications of resonator and substrate used 93
6.14 Summary of near-field results for linear and circular-polarized dielectric resonator antennas 98
6.15 Summary of measured radiation patterns for circular-polarized antenna at 4.20 GHz 102
6.16 Computed directivity and antenna efficiency using various methods . 105

Chapter 1

Introduction

A compact dielectric resonator (DR) antenna has been proposed and analyzed in this research work. The design process can be separated into two parts. The first part is to choose a suitable resonator dimensions for optimal performance. To do this, we need to have a good characterization of the DR's eigenmodes so that variation of the resonator's size with respect to its radiation Q-factor (Q_{rad}) and resonant frequency can be accurately predicted.

The radiation Q-factor is first studied using closed-form equations from [2] and [3]. Q_{rad} is then plotted against the resonator's size so as to identify a range of suitable dimensions with low Q_{rad}. Subsequently, we need to find out the resonant frequency of the chosen DRs and Tangential Vector Finite Element (TVFE) method is proposed for this analysis. Computed eigenvalues are compared with measured and predicted results using conventional models ([2],[4]). Comparison of results reveals that the proposed method is capable of predicting eigenvalues within 1% of error from measured values.

The second part involves the use of commercial software - Ansoft High Frequency Structure Simulator (*HFSS*) version 8.5 to design the feed structure. The eigenvalue computed in the first part provides a good guess of the antenna's operating frequency and the objective is to tune the feed design until the antenna operates close to this predicted frequency. In this way, high radiation efficiency of greater than 90% can be

achieved.

Even though *HFSS* has the capability to compute eigenvalues of an isolated DR, it suffers from convergence problem as the size of the terminating metallic box gets larger or when higher permittivity resonator is used. When solution does not converge, *HFSS* will refine its mesh and do the computation again. This iteration process is very time-consuming and the solution at times fails to converge at all. On the other hand, mesh generated using *Gmsh* for the written matlab codes is such that, only critical regions are meshed densely. For example, when a high dielectric constant resonator is analyzed, region inside the DR requires more refined mesh than the air-filled cavity. Hence, it allows the user more flexibility in choosing crucial areas where denser mesh is required. Computation resource will not be wasted on having to solve more unknowns due to meshing of non-critical regions. This leads to a faster and more accurate prediction of the DR's eigenvalues.

1.1 Background

The current trend in communications and wireless systems is towards miniaturization of every possible component, so as to integrate different modules into one system. At millimeter wave frequencies, integration of antennas and electronics is relatively more straightforward as the components are physically small and can be integrated on-chip or on the package. However, at lower frequencies such as in wireless applications, integrating antennas into a system on package is not easy. This is because the antenna is no longer physically small. The severe constraint on the physical size of integrated antennas therefore spurs designers to look into the implementation of electrically small ($ka < 1$) antennas. The requirements for high power efficiency and wide operational bandwidth makes the design and implementation of a wide band and efficient electrically small antennas of vital importance. However, as the antenna

gets electrically small, its fundamental limitations include a narrower bandwidth and lower radiation efficiency. This present as an additional constraint on the antenna design.

Traditional integrated antennas include microstrip patch, dipole and slot antennas. These antennas have the advantages of easy fabrication, high power capability and coplanar waveguide feed can be easily implemented. However, one of their primary limitations is their lower radiation efficiency due to existence of spurious surface waves in the substrate. As electrically small antenna is required, higher dielectric permittivity substrate is often needed. This results in even lower antenna radiation efficiency and narrower bandwidth. Another issue related to using patch antenna is the need for a ground plane. The impact of a finite size ground plane includes a great influence on the return loss and may cause new resonances. The finite size ground plane also acts as part of a radiator and may affect the radiation patterns and field distribution in the near-field region.

To overcome these limitations, a compact dielectric resonator (DR) antenna which make used of a pair of complementary magnetic dipole and magnetic loop [1] for wider bandwidth is proposed. Dielectric resonator antennas with printed feeds are not only compact in size, they also exhibit high radiation efficiency and good polarization selectivity within acceptable frequency bandwidth. In addition, DR antennas offer simple design for circular-polarized (CP) antennas. However, the resonator's dimensions and the substrate parameters together with the printed feed design must be carefully chosen for optimal performance of the antenna system.

1.2 Project Objectives

The objective of this thesis is to develop design and characterization methodologies for the proposed compact DR antennas. Hence, it involves much design and simulation of DR antennas with specified bandwidth, radiation pattern and polarization. Performance of a cylindrical and rectangular DR antennas are compared to show their strengths and limitations. To achieve small physical size, an electrically small DR antenna is also fabricated. Linear and circular-polarized antennas are implemented to verify broadband characteristic of the proposed feed structures and their radiation properties. Simulated and measured radiation patterns for these antennas are observed to be smooth and symmetrical, suitable for usage in various wireless applications.

To design an antenna with optimal performance, it is very important to characterize the eigenmodes of the dielectric resonator accurately. One of the objectives in this thesis is to do comparison studies of various conventional models used to model isolated DR and recommend a simple, yet robust method to predict the eigenvalues accurately. The Tangential Vector Finite Element (TVFE) method is found to be capable of predicting eigenvalues within 1% of error from measured results. Over the years, various models such as P. Guillon *et al*'s model [5] and Mongia *et al*'s close-form equations [2] have predicted resonant frequency of an isolated cylindrical DR to around 1% of error. The main strength of the TVFE method is that it can adapt to changes in the problem analyzed readily. No additional formulation is needed with the slightest change in the problem. Hence, a change in the dielectric resonator's geometry from cylindrical to rectangular, the inclusion of a finite size substrate or a metal plate placed near an isolated DR can be easily investigated by modifying the geometry, re-generating the mesh and re-defining the necessary boundary conditions. This can be easily done with an average performing personal computer.

1.3 Outline of Concept

In this research, eigenvalues of the dielectric resonator are computed using edge-based finite elements [6]. The resonator is placed in the center of a cavity whose dimensions are chosen to be sufficiently large so as not to perturb the fields of the dielectric resonator significantly. Formulation using tangential vector finite element is advantageous as it overcomes the occurrence of "spurious" modes faced by nodal based finite element approach. Even though this difficulty can be circumvented with the introduction of a penalty term, it is difficult to satisfy continuity requirements across material interfaces and treat geometries with sharp edges using classical finite element method. Even though the use of tangential vector finite elements results in more unknowns, the higher variable count is balanced by the greater sparsity of the finite element matrix. Hence, the computation time required to solve such a system iteratively with a given accuracy is still lesser than the traditional approach. Electric field $\{E\}$ within a three-dimensional cavity box with a center resonator occupying a volume V can be discretized into small tetrahedrals, each having an elemental volume V_e $(e = 1, 2, \ldots, M)$, where M is the total number of elements. To obtain numerical solution of E^e, it is expanded within the eth volume as

$$E^e = \sum_{j=1}^{m} N_j^e E_j^e = \{N^e\}^T \{E^e\}$$

where N_j^e are the edge-based vector basis functions, E_j^e denote the expansion coefficients of the basis function, m represents the number of edges comprising the element and the superscript e refers to the eth element. Substituting it into the usual vector wave equation and using variational formulation, some vector identities and divergence theorem, the weak form of Maxwell's equation is obtained and expressed in matrix form:

$$\{F\} = \frac{1}{2}(\{E\}^T[A]\{E\} - k_o^2\{E\}^T[B]\{E\})$$

where F represents the variational function. An eigenvalue system is then obtained by applying the Ritz procedure, which amounts to taking the partial derivative of F with respect to each unknown edge field and setting the result to zero. The result is

$$[A]\{E\} = k_o^2[B]\{E\}$$

where $[A]$ and $[B]$ are $N \times N$ symmetric, sparse matrices with N being the total number of edges resulting from the subdivision of the body excluding the edges on the boundary. The eigenvalues k_o can be subsequently computed from the above equation after imposing the necessary boundary conditions.

1.4 Thesis Layout

The layout of the thesis is as follows:

Chapter 2: Literature research is done to provide an overview of the DR antenna technology and packaging techniques for electrically small antennas. Some common analytical models used to characterize isolated DR are also reviewed and a paper on the computation of cavity resonances using edge-based finite element has been found to be useful in this research work.

Chapter 3: Conventional analytical models such as magnetic wall model, dielectric waveguide model and Mongia's closed-form equations for resonant frequency and Q-factors are examined.

Chapter 4: Evaluation of the eigenvalues using TVFE method is discussed in detail. A brief explanation of the variational formulation is presented, followed by listing the finite element numerical procedures. Finally, software implementations of Matlab codes are explained.

Chapter 5: Parametric study of the antenna is done to aid subsequent design process. The fundamental limitations of electrically small antennas are listed. Finally, precautions taken for the measurement of a small antenna are discussed.

Chapter 6: Eigenvalues computed using TVFE method are compared with measured results. In addition, the proposed method is compared with some popular models commonly used for analyzing DR antennas, to ascertain the range of validity of the models. Measurement results of the fabricated antennas are subsequently presented, discussed and compared.

Chapter 7: The limitations of the TVFE method are discussed. Suggestions for improvement and future works are made to conclude the thesis.

Appendix A: Derivations of the unknown coefficients a_j^e, b_j^e, c_j^e and d_j^e.

Appendix B: Details of implementation of the computer programs in the thesis.

1.5 Original Contributions

In this project, the following original contributions have been made:

(i) Using Tangential Vector Finite Element (TVFE) method, eigenvalues of various dielectric resonator geometries (cylindrical and rectangular) are compared with some conventional models. TVFE method is found to be robust and capable of predicting within 1% of error.

(ii) A compact DR antenna structure, modified from [1] to exclude the ground plane has been proposed. Simulation and measurement results for linear and circular-polarized antennas are in good agreement, verifying the usefulness of the printed feed designs for broadband antennas. These antennas also have smooth and symmetric radiation patterns, with high radiation efficiency.

(iii) Design methodology is proposed to aid subsequent design process for linear-polarized (LP) and circular-polarized (CP) antennas.

Chapter 2

Literature Review

2.1 Dielectric Resonator Antennas Supported by 'Infinite' and Finite Ground Planes

In 1997, Z. Wu *et al* [7] carried out an experimental study of the effects of ground plane size on a cylindrical dielectric resonator antenna fed by a probe. For the convenience of the feed, dielectric resonator antenna usually had the support of a ground plane of finite size. The parameters of concern include the antenna's resonance frequency, radiation pattern, gain and bandwidth. It has been observed that when the ground plane is smaller than half-wavelength, the antenna suffers the largest effect. Experimental study has shown that the size of the ground plane can affect radiation of the antenna particularly at angles close to the ground surface. Resonant frequency is mostly affected by the size of the ground plane when diameter of the ground plane is smaller than half-wavelength. The frequency increases with the size of the ground plane, with only little change when the diameter is greater than a wavelength. Backward radiation is more severe for antenna with finite ground plane. The backward radiation would lower the gain of the antenna. Experimentation shows that the antenna gain increases from 2.73dB to 2.98dB as the diameter of the ground plane increases from 2cm to 10cm. As the ground plane gets smaller, the impedance bandwidth increases from 3.2% to 4.2%.

2.2 Packaging Technique for Gain Enhancement of Electrically Small Antenna designed on Gallium Arsenide

In 2000, C.T.P. Song *et al* [8] presented a method to achieve complete RF front end product equipped with its radiator within a single chip package. This is by placing a parasitic radiator very close to the feed antenna, enabling the parasite to extract the highly reactive near-field associated with the poor performance of a reduced size feed antennas. This packaging technique offers alternative solution to difficulties associated with electrically small antennas using gallium arsenide substrate and increases the antenna gain by 15dB. As a result, manufacturing costs associated with connecting the antenna to the RF front-end chip can be reduced.

The increasing demand for compact and fully integrated RF front end products is due to their robustness, portability and ease of integration. One of the major challenge now is to include a compact and fully integrated antenna, transmitter and receiver on a single transceiver chip. However, such a configuration often suffers from poor efficiency and narrow bandwidth. This is due to the antenna's small radiating element and hence a small effective aperture for collecting incoming radio signals or providing radiation.

A quarter-wave H-shaped microstrip patch antenna operating at 5.8GHz, with MESFET switches use as time division duplex operation, is used as the feed patch. The chip antenna (4.1×2.1mm) is mounted on a brass block (20×20×6mm) which acts as the ground plane for the antenna. Due to the small feed antenna size, a gain of -10dBi is reported as compared to conventional patch antenna gain of +5dBi. The parasitic radiator with a size of 22×22mm, is placed above the feed antenna at distance of 0.5-10mm. Often, poor matching performance is due to difficulties in achieving an optimum bond onto the chip. The bandwidth achieved by this antenna configuration is 0.67%. Measured results show that the chip antenna without the

parasite has a gain of -15dBi. The low gain is again due to the poor bond wire properties. The inclusion of a parasitic radiator (placed 2mm above the feed) results in an overall antenna gain close to 1dBi. It is observed in the experiment that increasing the antenna ground plane can further improved the antenna gain to 6dBi.

The paper also offers suggestion to packaging design and assembly. It is well understood that packaging of a fragile semiconductor chip on a suitable carrier provides robustness, ease of handling and protects the device from environmental degeneration. Some of the more popular chip carriers are made of plastics and ceramics. As the silicon/GaAs chip will perform all the necessary signal processing, only a few connection pins are needed on the lead frame. These are effectively for the supply voltage, ground and baseband signals. The parasitic antenna then sits on top of the carrier material, sealing the MMIC antenna chip. The lid which seals the parasite within the package may also be used as a radome to further improve the gain.

2.3 A Low-Profile Rectangular Dielectric Resonator Antenna

In this paper, Esselle [9] reported a rectangular dielectric resonator antenna with a very low profile (length-to-height ratio≈6). This aperture-coupled antenna can be matched to the 50Ω input and radiates like a magnetic dipole at 11.6GHz.

The DRA has often been presented as a better alternative to microstrip patch antenna. In order to have a fair comparison, the DRA has to have a low-profile. Many low profile DRAs make use of very high permittivity material but in this paper, a better comparison is made since the resonator has medium permittivity of 10.8. The substrate has a permittivity of 10.2 and thickness of 0.64mm. The rectangular resonator has a dimension of 15.2(L)×7.0(W)×2.6(H) mm.

The antenna is perfectly matched to the 50Ω input at this frequency, giving a return loss of 38dB. Even though absorbers were placed around the edge of the ground

plane to minimize ground effects, the radiation patterns are still marred by ripples (-90$\leq \theta \leq$90). It also has a very low antenna gain value (close to 0dB). The cross-polarization is more than 15 dB below the co-polarization for the same directions. The author attributes the difference between the measured and theoretical radiation patterns to the finite size of the ground plane in the test antenna.

2.4 Overview of Analytical Models for Isolated Dielectric Resonator

One of the simplest models to determine the resonant frequency of an isolated dielectric resonator is by using Cohn's Model [10]. In Cohn's analysis, the electromagnetic field inside a dielectric resonator with high dielectric constant may be approximately described by assuming all surfaces are covered by perfect magnetic conductor. This crude characterization of the dielectric resonator resulted in predicting the resonant frequency with more than 10% of error.

A better analysis of the dielectric resonator is introduced by Itoh and Rudokas [11]. Instead of using idealized waveguide with perfect magnetic walls like in Cohn's Model, this model starts with a more realistic dielectric rod waveguide. Therefore, continuity of both the electric and magnetic fields tangential to the dielectric resonator's cylindrical interface is ensured. Hence, eigenvalue solved from the transcendental equations is a more accurate description of an isolated dielectric resonator than the Cohn's Model. As a result, this approximation method gives a considerably better prediction of the resonant frequency with 2% of error.

Subsequently, full-blown solution of the boundary value problem has been achieved by various authors predicting the resonant frequency with better than 1% accuracy. Using a combination of magnetic wall and dielectric waveguide models, Guillon and Garault [5] are able to propose a method with around 1% accuracy. However, in all the analytic models mentioned above, effects of the feed on the resonant frequency and

higher order modes are not taken into account. To do so, rigorous analysis methods such as Method of Moment (MoM), Finite Difference Time Domain (FDTD) and Finite Element Method (FEM) are required to include environmental effects on the antenna.

2.5 Computation of Cavity Resonances Using Edge-Based Finite Elements

In this paper by A. Chatterjee *et al* [6], eigenvalues of a cavity resonator are obtained accurately using edge-based finite elements. It has also been observed that this formulation method is suitable for modeling arbitrarily shaped inhomogeneous regions. A comparison between the edge-based tetrahedral and rectangular brick elements shows the use of tetrahedral elements leads to greater accuracy of the computed eigenvalues.

It is often necessary to solve Maxwell's equations for the resonances of a closed cavity. As exact eigenvalues can only be evaluated for simple geometries, numerical technique such as the finite element method is required for arbitrarily shaped cavities. However, the occurrence of spurious modes in nodal based finite element method often plague the computation of their eigenvalues. Even though this can be overcome by implementing a penalty term, continuity of fields across material interfaces and geometries with sharp edges are not easy to fulfil. It is suggested in this paper, the use tangential vector finite elements can overcome these shortcomings. Even though the use of edge elements would results in more unknowns, this can be balanced by the greater sparsity of the finite element matrix. Hence, computation time required to solve such a system iteratively with a given accuracy is still lesser than the conventional approach.

Using edge-based finite element method, a comparison of the computed eigenvalues for a 1.0×0.5×0.75cm rectangular cavity is presented, using rectangular bricks and

tetrahedral elements. The edge-based approach using tetrahedral elements predicts the first six distinct non-trivial eigenvalues with less than 4 percent error. This is much accurate than using rectangular brick elements which predicts the same eigenvalues with less than 6 percent error. This is despite the rectangular brick elements having a maximum edge length of 0.15 cm which is smaller than the tetrahedral elements of 0.2 cm. Another comparison of the computed eigenvalues for a rectangular cavity half-filled with a dielectric filling of $\epsilon_r = 2$, show good agreement (percentage error within 1%) with the analytical values. Hence, edge-based approach has been reliable in predicting the eigenvalues for both homogeneous and inhomogeneous cavities.

Chapter 3

Analytical Models for Dielectric Resonator

Various analytical models have been used over the years to analyze isolated dielectric resonator. It is usually developed by making basic assumptions to offer simple and analytical solutions to an understanding of the physical phenomena. In analytical methods, fields associated with the antenna are divided into interior and exterior regions as shown in Figure 3.1.

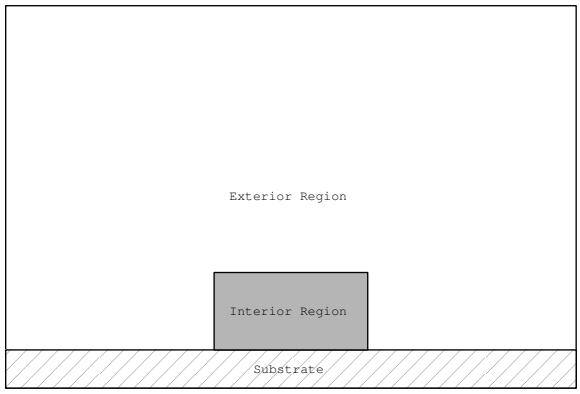

Figure 3.1: Division of fields associated with a dielectric resonator into interior and exterior region

The interior region refers to fields within the resonator and the exterior region includes the air and substrate. Often, it is of great practical interest to obtain solution of the electromagnetic fields within the dielectric resonator in some simplified way that is

still capable of giving results which are not too far from the exact values. In this chapter, four such simple mathematical models shall be reviewed.

3.1 Magnetic Wall Model

In 1983, a simple analysis for a cylindrical DR antenna was carried out by S.A. Long *et al* [4] using perfect magnetic wall model. Figure 3.2 shows the geometry of the DR antenna analyzed.

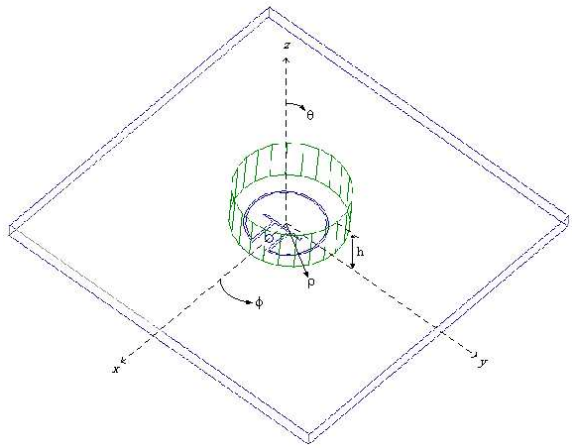

Figure 3.2: Geometry of a cylindrical DR antenna

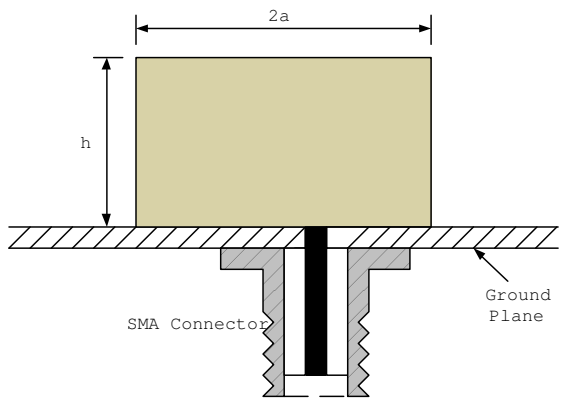

Figure 3.3: Side view of the cylindrical DR antenna

3.1.1 Different excitation modes

Various modes can be excited in the dielectric resonator. Figure 3.4-3.7 show the E-fields and H-fields of an isolated cylindrical DR. A study of the field configurations is very useful, as it gives designers some intuition of the antenna's far-field radiation characteristics. In this way, radiation patterns of a DR antenna can be predicted quite accurately without extensive computations. From Figure 3.4, it can be observed that $TE_{01\delta}$ mode radiates like a magnetic dipole oriented along the vertical (z-axis) direction. Similarly, $TM_{01\delta}$ mode radiates like an axial electric dipole. Such modes have endfire radiation patterns. In contrast, the fields for $TM_{11\delta}$ mode suggest it will radiate like a magnetic dipole oriented along the horizontal direction. Such a mode has a main beam in the broadside direction. As for $TM_{21\delta}$ mode, it radiates like a magnetic quadrupole oriented also along the horizontal direction. When magnetic walls are not no longer imposed on the cylindrical DR's surface, $TM_{11\delta}$ mode is replaced by hybrid $HE_{11\delta}$ mode. This is the lowest order mode, giving rise to the smallest antenna size and a desirable main beam along the broadside direction.

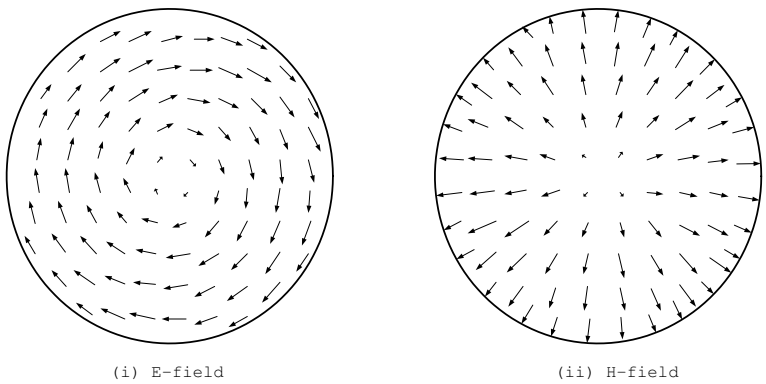

Figure 3.4: Fields inside an isolated cylindrical DR for $TE_{01\delta}$ mode

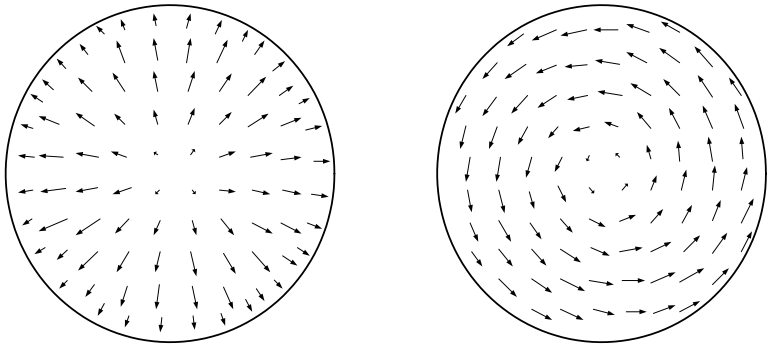

(ii) E-field (i) H-field

Figure 3.5: Fields inside an isolated cylindrical DR for $TM_{01\delta}$ mode

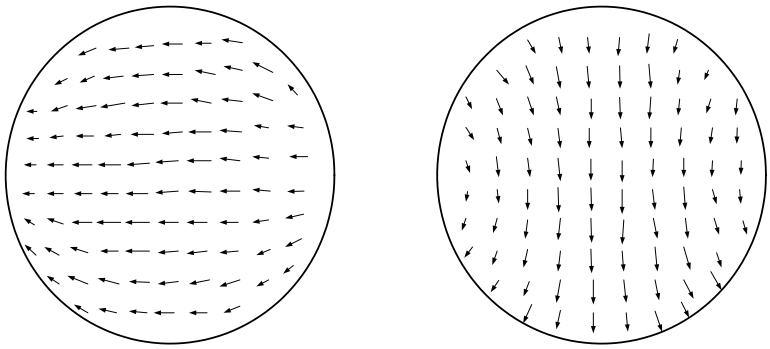

(ii) E-field (i) H-field

Figure 3.6: Fields inside an isolated cylindrical DR for $TM_{11\delta}$ mode

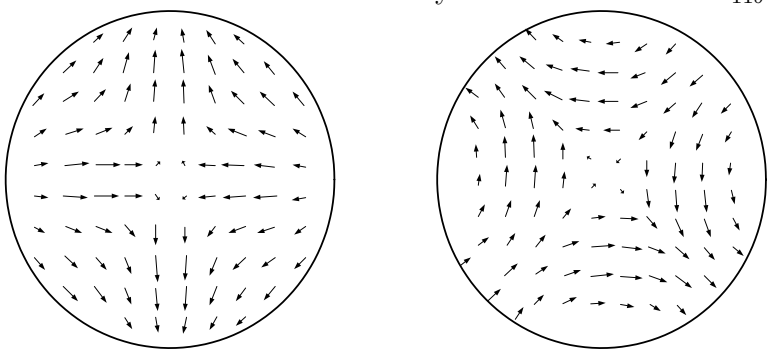

(i) E-field (ii) H-field

Figure 3.7: Fields inside an isolated cylindrical DR for $TM_{21\delta}$ mode

3.1.2 Resonant frequencies

When the DRA surfaces are assumed to be perfect magnetic conductors, wave functions for such a cavity can be represented as follows [4]:

$$\Psi_{TE_{npm}} = J_n\left(\frac{\chi_{np}^{TE}}{a}\rho\right)\begin{Bmatrix}\sin n\phi\\ \cos n\phi\end{Bmatrix}\sin\left[\frac{(2m+1)\pi z}{2d}\right] \tag{3.1.1}$$

$$\Psi_{TM_{npm}} = J_n\left(\frac{\chi_{np}^{TM}}{a}\rho\right)\begin{Bmatrix}\sin n\phi\\ \cos n\phi\end{Bmatrix}\cos\left[\frac{(2m+1)\pi z}{2d}\right] \tag{3.1.2}$$

where $\Psi_{TE_{npm}}$ and $\Psi_{TM_{npm}}$ refer to wave functions for the transverse electric (TE) to z and transverse magnetic (TM) to z respectively. J_n is the Bessel function of the first kind, with $J_n(\chi_{np}^{TE}) = 0$, $J_n'(\chi_{np}^{TM}) = 0$, n=1,2,3,..., p=1,2,3,... and m=0,1,2,3,... From the separation equation $k_\rho^2 + k_z^2 = k^2 = w^2\mu\epsilon$, the resonant frequency of the npm mode can be found as follows:

$$f_{npm} = \frac{1}{2\pi a\sqrt{\mu\epsilon}}\sqrt{\begin{Bmatrix}\chi_{np}^{TE^2}\\ \chi_{np}^{TM^2}\end{Bmatrix} + \left[\frac{\pi a}{2d}(2m+1)\right]^2} \tag{3.1.3}$$

and the wavenumbers are found as

$$k_\rho = \frac{1}{a}\begin{Bmatrix}\chi_{np}^{TE}\\ \chi_{np}^{TM}\end{Bmatrix} \tag{3.1.4}$$

$$k_z = \frac{(2m+1)\pi}{2d} \tag{3.1.5}$$

For most applications, it is of interest to excite the fundamental (dominant) mode, which has the lowest resonant frequency and the smallest antenna size. The mode of interest in this case is the TM_{110}. The resonant frequency is calculated by using

$$f_{TM_{110}} = \frac{c}{2\pi a\sqrt{\epsilon_r}}\sqrt{(\chi_{11}^{TM})^2 + \left(\frac{\pi a}{2d}\right)^2} \tag{3.1.6}$$

where $\chi_{11}^{TM} = 1.841$.

3.1.3 Equivalent magnetic surface currents

The TM_{110} mode fields within the cylindrical dielectric resonator are used for the derivation of the far-field expressions. Using equation 3.1.2, the wave function of this mode is expressed as:

$$\Psi_{TM_{110}} = J_1\left(\frac{\chi_{11}^{TM}}{a}\rho\right)\cos\phi\cos\left[\frac{z\pi}{2d}\right] \tag{3.1.7}$$

The $\cos\phi$ term is used because the feed position is along $\phi = 0$. From equation 3.1.7, the various E-fields can subsequently be obtained as follows:

$$E_\phi = \frac{1}{j\omega\epsilon\rho}\frac{\partial^2\Psi}{\partial\phi\partial z} \tag{3.1.8}$$

$$E_z = \frac{1}{j\omega\epsilon}\left(\frac{\partial^2}{\partial z^2} + k^2\right)\Psi \tag{3.1.9}$$

$$E_\rho = \frac{1}{j\omega\epsilon}\frac{\partial^2\Psi}{\partial\rho\partial z} \tag{3.1.10}$$

$\Psi_{TM_{110}}$ is expressed as Ψ for convenience. Using equivalence principle,

$$\overrightarrow{M_s} = \overrightarrow{E} \times \hat{n} \tag{3.1.11}$$

the equivalent magnetic currents on the DRA surfaces are found and treated as the radiating sources for far-field radiation fields. The equivalent currents obtained are:

The side wall:

$$M_{z'} = \frac{\pi}{2j\omega\epsilon ad}J_1(\chi_{11}^{TM})\sin\phi'\sin\left[\frac{\pi z'}{2d}\right] \tag{3.1.12}$$

$$M_{\phi'} = \frac{1}{j\omega\epsilon}\left(\frac{\chi_{11}^{TM}}{a}\right)^2 J_1(\chi_{11}^{TM})\cos\phi'\cos\left[\frac{\pi z'}{2d}\right] \tag{3.1.13}$$

The top and bottom walls:

$$M_{\phi'} = \frac{\pi\chi_{11}^{TM}}{2j\omega\epsilon ad}J_1'\left(\frac{\chi_{11}^{TM}\rho'}{a}\right)\cos\phi' \tag{3.1.14}$$

$$M_{\rho'} = \frac{\pi}{2j\omega\epsilon\rho' d}J_1\left(\frac{\chi_{11}^{TM}\rho'}{a}\right)\sin\phi' \tag{3.1.15}$$

3.1.4 Field Configuration

As the radiation fields are usually expressed in spherical coordinates (r, θ, ϕ), transformation of coordinates from cylindrical to spherical coordinates is required. Hence, the following equations are obtained:

$$M_\theta = M_{\rho'} \cos\theta \cos(\theta - \theta') + M_{\phi'} \cos\theta \sin(\theta - \theta') - M_{z'} \sin\theta \quad (3.1.16)$$

$$M_\phi = -M_{\rho'} \sin(\phi - \phi') + M_{\phi'} \cos(\phi - \phi') \quad (3.1.17)$$

After transformation, the currents are then used for the calculations of the electric vector potentials:

$$F_\theta = \frac{e^{-jk_o r}}{4\pi r} \int\int\int M_\theta e^{jk_o[\rho' \sin\theta \cos(\phi-\phi')+z' \cos\theta]} \rho' d\rho' d\phi' dz \quad (3.1.18)$$

$$F_\phi = \frac{e^{-jk_o r}}{4\pi r} \int\int\int M_\phi e^{jk_o[\rho' \sin\theta \cos(\phi-\phi')+z' \cos\theta]} \rho' d\rho' d\phi' dz \quad (3.1.19)$$

where $k_o = \omega\sqrt{\mu_o \epsilon_o}$ is the free space wave number. In far-field region, the electric field E_θ and E_ϕ are proportional to the vector potentials F_ϕ and F_θ respectively. In order to express the vector potentials into forms suitable for programming, they are further evaluated as:

$$F_\theta = C_1\{I_2 - I_1 - 0.5k_\rho(I_3 + I_4 - I_5 - I_6) + 1.16k_o \sin\theta J_1(k_o a \sin\theta) D_1 - 0.581k_\rho^2 a[J_o(k_o a \sin\theta) + J_2(k_0 a \sin\theta)] D_1\} \quad (3.1.20)$$

$$F_\phi = C_2\{-I_1 - I_2 - 0.5k_\rho(I_3 - I_4 - I_5 + I_6) - 0.581k_\rho^2 a[J_o(k_o a \sin\theta) - J_2(k_o a \sin\theta)] D_1\} \quad (3.1.21)$$

where

$$C_1 = \frac{\pi^2}{j\omega\epsilon d}\frac{1}{4\pi r}\sin\phi\cos(k_o d\cos\theta)\cos\theta \tag{3.1.22}$$

$$C_2 = \frac{\pi^2}{j\omega\epsilon d}\frac{1}{4\pi r}\cos\phi\cos(k_o d\cos\theta) \tag{3.1.23}$$

$$D_1 = \left[\frac{\pi^2}{4d^2} - k_o^2\cos^2\theta\right]^{-1} \tag{3.1.24}$$

$$k_\rho = \frac{\chi_{11}^{TM}}{a} = \frac{1.841}{a} \tag{3.1.25}$$

$$I_1 = \int_0^a J_1(k_\rho\rho')J_0(k_o\rho'\sin\theta)d\rho' \tag{3.1.26}$$

$$I_2 = \int_0^a J_1(k_\rho\rho')J_2(k_o\rho'\sin\theta)d\rho' \tag{3.1.27}$$

$$I_3 = \int_0^a J_0(k_\rho\rho')J_0(k_o\rho'\sin\theta)\rho' d\rho' \tag{3.1.28}$$

$$I_4 = \int_0^a J_0(k_\rho\rho')J_2(k_o\rho'\sin\theta)\rho' d\rho' \tag{3.1.29}$$

$$I_5 = \int_0^a J_2(k_\rho\rho')J_0(k_o\rho'\sin\theta)\rho' d\rho' \tag{3.1.30}$$

$$I_6 = \int_0^a J_2(k_\rho\rho')J_2(k_o\rho'\sin\theta)\rho' d\rho' \tag{3.1.31}$$

3.2 Dielectric Waveguide Model

An analytical model commonly used to model rectangular dielectric resonator antenna is the dielectric waveguide model (DWM) [12]. The model originated from DWM of rectangular dielectric guides. However, in this case the waveguide is truncated along the z-direction at $\pm d/2$ as shown in Figure 3.8. The six walls of the rectangular DR are assumed to be perfect magnetic walls.

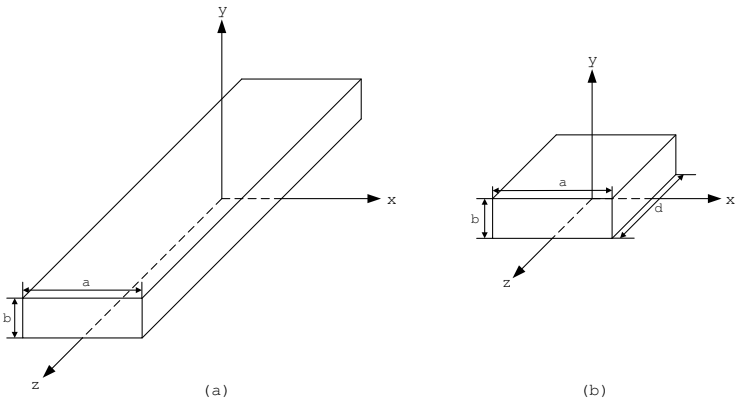

Figure 3.8: (a) Infinite Dielectric Waveguide (b) Truncated Dielectric waveguide

3.2.1 Field Configuration

For a rectangular DR antenna with dimension $a, b > d$, the lowest order mode will be TE^z_{111}. Using DWM, the following fields within the DR antenna are obtained:

$$H_x = \frac{k_x k_z}{jw\mu_o} \sin(k_x x)\cos(k_y y)\sin(k_z z) \tag{3.2.1}$$

$$H_y = \frac{k_y k_z}{jw\mu_o} \cos(k_x x)\sin(k_y y)\sin(k_z z) \tag{3.2.2}$$

$$H_z = \frac{k_x^2 + k_y^2}{jw\mu_o} \cos(k_x x)\cos(k_y y)\cos(k_z z) \tag{3.2.3}$$

$$E_x = k_y \cos(k_x x)\sin(k_y y)\cos(k_z z) \tag{3.2.4}$$

$$E_x = -k_x \sin(k_x x)\cos(k_y y)\cos(k_z z) \tag{3.2.5}$$

$$E_z = 0 \tag{3.2.6}$$

where

$$k_x^2 + k_y^2 + k_z^2 = \epsilon_r k_o^2 \tag{3.2.7}$$

$$k_z \tan(k_z d/2) = \sqrt{(\epsilon_r - 1)k_o^2 - k_z^2} \tag{3.2.8}$$

$$k_o = \frac{2\pi}{\lambda_o}\ ,\ k_x = \frac{m\pi}{a}\ ,\ k_y = \frac{n\pi}{b} \tag{3.2.9}$$

3.2.2 Resonant Frequency

To evaluate the resonant frequency of the DR, k_x and k_y are substituted into characteristic equation 3.2.7 and then used in the transcendental equation 3.2.8 to solve for k_z. The resonant frequency can be obtained from (3.2.7) by solving for k_o using the k_z evaluated using simple numerical root-finding method.

3.2.3 Q-Factor

The radiation Q-factor of the DR antenna is determined as follows:

$$Q_{rad} = \frac{2wW_e}{P_{rad}} \tag{3.2.10}$$

where W_e and P_{rad} are the stored energy and radiated power respectively. These parameters can be obtained using:

$$W_e = \frac{\epsilon_o \epsilon_r abd}{32}\left(1 + \frac{\sin(k_z d)}{k_z d}\right)(k_x^2 + k_y^2) \tag{3.2.11}$$

$$P_{rad} = 10k_o^4 |P_m|^2 \tag{3.2.12}$$

$$P_m = \frac{-jw8\epsilon_o(\epsilon_r - 1)}{k_x k_y k_z}\sin(k_z d/2)\hat{z} \tag{3.2.13}$$

The bandwidth (BW) can be obtained as

$$BW = \frac{S-1}{Q_e\sqrt{S}} \tag{3.2.14}$$

where S is the maximum acceptable voltage standing wave ratio (VSWR). The normalized Q-factor is defined as

$$Q_e = \frac{Q_{rad}}{\epsilon_r^{3/2}} \tag{3.2.15}$$

3.3 Empirical Equations derived from Rigorous Methods

In the previous sections, some analytical models commonly used for isolated dielectric resonator are reviewed. A more accurate way to determining the resonator's frequency and bandwidth, is by using the equations proposed by Mongia *et al* [2] and Kishk *et al* [3]. It was found from rigorous methods that

$$k_o a \ \propto \ \frac{1}{\sqrt{\epsilon_r + X}} \tag{3.3.1}$$

gives a good approximation to describe the dependence of normalized wavenumber as a function of ϵ_r. The value of X is found empirically by comparing the numerical results of numerical methods. Its value is quite small and is assumed to depend on the mode.

3.3.1 Resonant Frequency of Isolated Cylindrical DRs

$\mathbf{HE}_{11\delta}$ Mode:

$$k_o a_{(\epsilon_r=38)} = \frac{6.324}{\sqrt{\epsilon_r + 2}} \left[0.27 + 0.36 \left(\frac{a}{2H} \right) + 0.02 \left(\frac{a}{2H} \right)^2 \right] \tag{3.3.2}$$

where c is the velocity of light in free-space. Range of validity for the above equation is $0.4 \leq \ a/H \ \leq 6$.

$\mathbf{TE}_{01\delta}$ Mode:

$$k_o a_{(\epsilon_r \geq 25)} = \frac{2.327}{\sqrt{\epsilon_r + 1}} \left[1.0 + 0.2123 \left(\frac{a}{H} \right) - 0.00898 \left(\frac{a}{H} \right)^2 \right] \tag{3.3.3}$$

where the the above formula is valid in the range $0.33 \leq \ a/H \ \leq 5$.

$\mathbf{TE}_{011+\delta}$ Mode:

$$k_o a_{(\epsilon_r \geq 25)} = \frac{2.208}{\sqrt{\epsilon_r + 1}} \left[1.0 + 0.7013 \left(\frac{a}{H} \right) - 0.002713 \left(\frac{a}{H} \right)^2 \right] \tag{3.3.4}$$

where the the above formula is valid in the range $0.33 \leq \ a/H \ \leq 5$.

$\mathbf{TM}_{01\delta}$ Mode:

$$k_o a = \frac{\sqrt{3.83^2 + \left(\frac{\pi a}{2H}\right)^2}}{\sqrt{\epsilon_r + 2}} \tag{3.3.5}$$

where the the above formula is valid in the range $0.33 \leq \ a/H \ \leq 5$.

3.3.2 Bandwidth of Isolated Cylindrical DRs

The impedance bandwidth of an antenna refers to the frequency bandwidth in which the antenna's $VSWR$ is less than a specified value S. Impedance bandwidth of a DR antenna, when completely matched to the coplanar waveguide feed at its resonant frequency, is related to the total unloaded Q-factor (Q_u) of the resonator by the following equation:

$$BW = \frac{S - 1}{Q_u \sqrt{S}} \tag{3.3.6}$$

For a DR antenna, its dielectric and conductor loss are negligible as compared to its radiated power. Hence, the total unloaded Q-factor (Q_u) is related to the radiation Q-factor (Q_{rad}) by

$$Q_u \ \simeq \ Q_{rad} \tag{3.3.7}$$

It has been found from rigorous numerical methods that Q_{rad} depends on the DR's radius to height aspect ratio and the dielectric constant of the resonator.

$HE_{11\delta}$ Mode:

$$Q_{rad(\epsilon_r=38)} = 0.01007(\epsilon_r)^{1.30}\frac{a}{H}\left\{1+100e^{-2.05[0.5(a/H)-0.0125(a/H)^2]}\right\} \tag{3.3.8}$$

Range of validity for the above equation is $0.4 \leq \ a/H \ \leq 6$.

$TE_{01\delta}$ Mode:

$$\begin{aligned} Q_{rad(\epsilon_r\geq 25)} = 0.078192(\epsilon_r)^{1.27}[1.0 \quad & +17.31\left(\tfrac{H}{a}\right) - 21.57\left(\tfrac{H}{a}\right)^2 \\ & +10.86\left(\tfrac{H}{a}\right)^3 - 1.98\left(\tfrac{H}{a}\right)^4] \end{aligned} \tag{3.3.9}$$

Range of validity for the above equation is $0.5 \leq \ a/H \ \leq 5$.

$TE_{011+\delta}$ Mode:

$$\begin{aligned} Q_{rad(\epsilon_r\geq 25)} = 0.03628(\epsilon_r)^{2.38}[-1.0 + 7.81\left(\frac{H}{a}\right) \quad & - \quad 5.858\left(\frac{H}{a}\right)^2 \\ & + \quad 1.277\left(\frac{H}{a}\right)^3] \end{aligned} \tag{3.3.10}$$

Range of validity for the above equation is $0.5 \leq \ a/H \ \leq 5$.

$TM_{01\delta}$ Mode:

$$\begin{aligned} Q_{rad} \quad & = 0.009(\epsilon_r)^{0.888}e^{0.04\epsilon_r}\left\{1-\left[0.3-0.2\left(\tfrac{a}{H}\right)\right]\left[\tfrac{38-\epsilon_r}{28}\right]\right\} \\ & .\left\{9.498\left(\tfrac{a}{H}\right)+2058.33\left(\tfrac{a}{H}\right)^{4.322}e^{-3.501(a/H)}\right\} \end{aligned} \tag{3.3.11}$$

3.3.3 Radiation Q-Factor and Eigenvalues of Various Modes

Using empirical equations [2],[3] from previous section, variation of the DR's radiation Q-factor and wavenumbers are plotted against the a/h aspect ratio in Figures 3.9-3.12. $TM_{01\delta}$, $TE_{01\delta}$ and $HE_{11\delta}$ modes are considered in this investigation.

It is interesting to find out the amount of bandwidth attainable by an isolated DR without resorting to bandwidth enhancement techniques. Comparing Figures 3.9 and 3.11, it is observed that DR with lower dielectric constant value has a lower radiation Q-factor and therefore, a wider impedance bandwidth. However, it may not be practical to choose a resonator with too low permittivity value. Since, the resonator must have a dielectric constant high enough to contain the fields within the DR antenna in order to resonate.

Figures 3.9 and 3.11 also provide typical radiation Q-factor values for DR with $\epsilon_r = 10.2$ and 38.5. These values are useful to give designers some intuition of typical bandwidth achievable by DR antennas. It is interesting to note that a low profile antenna give the widest bandwidth, but the bandwidth does not increase monotonically with the DR antenna's volume. As the DR antenna's volume increases, the bandwidth decreases initially until it reaches a minimum value and then increases with volume. However, it should be kept in mind that the estimated achievable bandwidth was determined for an isolated DR and do not take into account the coupling mechanisms which may reduce the achievable bandwidth significantly.

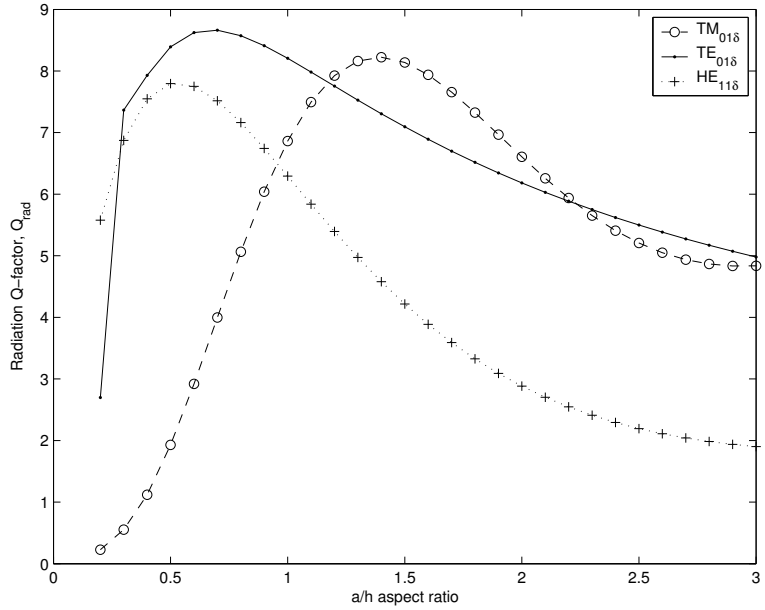

Figure 3.9: Radiation Q-factor of a dielectric disc with radius a, height h and dielectric constant $\epsilon_r = 10.2$.

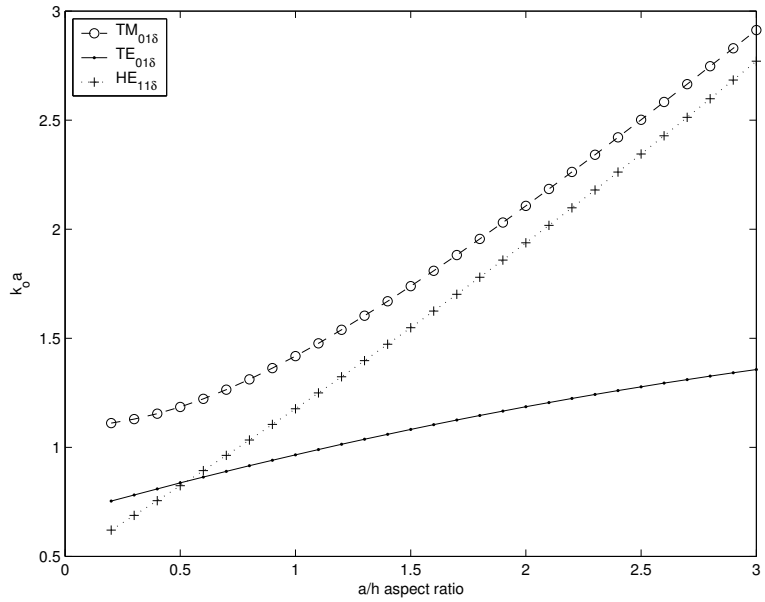

Figure 3.10: Resonant wavenumbers of different modes for an isolated cylindrical DR with radius a, height h and dielectric constant $\epsilon_r = 10.2$.

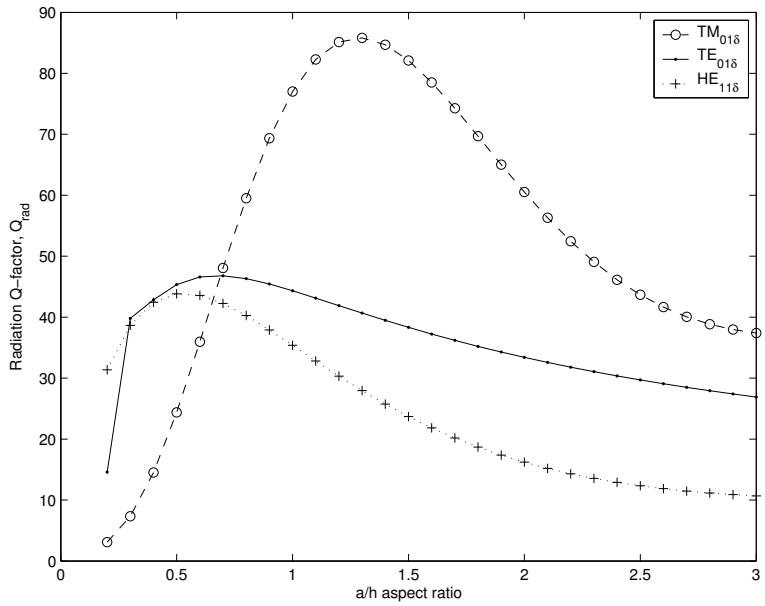

Figure 3.11: Radiation Q-factor of a dielectric disc with radius a, height h and dielectric constant $\epsilon_r = 38.5$.

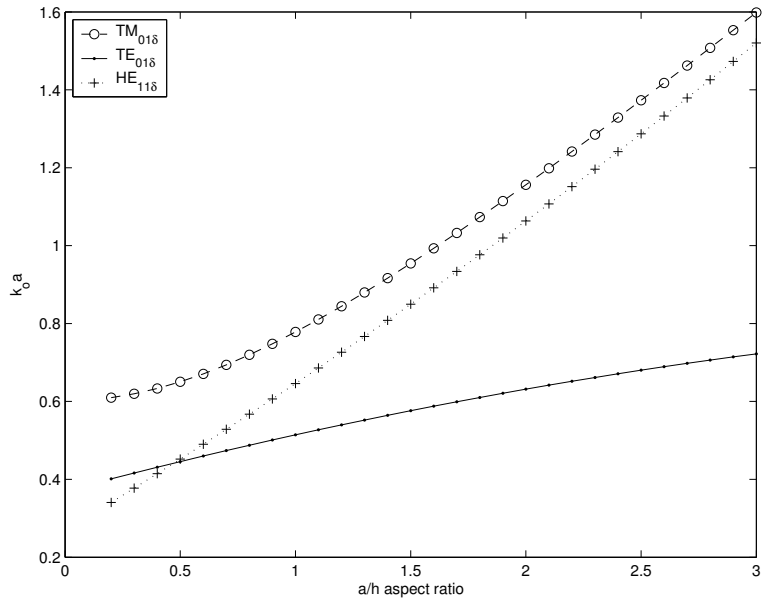

Figure 3.12: Resonant wavenumbers of different modes for an isolated cylindrical DR with radius a, height h and dielectric constant $\epsilon_r = 38.5$.

Chapter 4

Full-Wave Analysis of Dielectric Resonator using Finite Element Method

In the previous chapter, a number of analytical models have been used to characterize dielectric resonator antenna. However, these simple models are not able to characterize environmental effects such as the existence of a substrate, a finite size ground plane, a feed substrate or a metallic box enclosing the dielectric resonator. Also, higher order modes or hybrid modes co-exist with the desired mode within the resonator. Their effects can be taken into account by using full-wave analysis. Over the years, various more complex methods have been employed to analysis the dielectric resonator. These range from various radial and axial mode matching methods [13]-[14], the asymptotic expansion method for resonators with very high permittivity [15], the moment method based on the surface integral techniques [16]-[17] and the conventional mode matching approaches using dyadic Green functions or transverse modes in expanding the interior and exterior fields [18]. Normally, these methods are used to compute rigorously the resonant frequencies, the electromagnetic field distribution of axis symmetric structures and their unloaded quality factors.

In this thesis, three-dimensional finite element method is used to investigate *TE*, *TM* and hybrid DR modes. Finite element method has shown to be the most applicable and versatile way to analyze a dielectric resonator resting on a finite size

ground plane. With this method, it is possible to fit any polygonal shape by choosing triangular element shapes and sizes. To increase the accuracy of the solution, denser mesh or high-order polynomial approximation functions can be used. Formulation in this chapter can be found in [19] and interested reader can refer to this book for more details.

4.1 Problem Description

Consider the case of a dielectric resonator placed in the center of a metallic cavity shown in Figure 4.1:

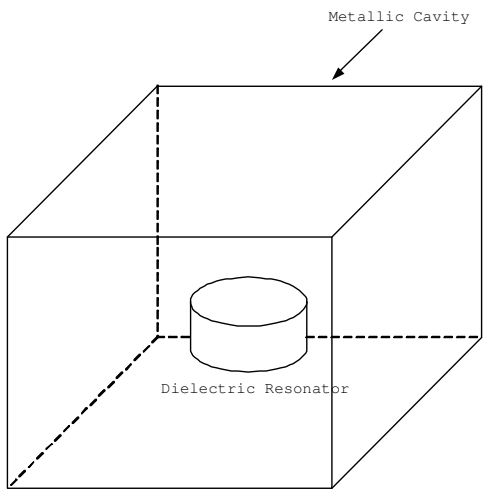

Figure 4.1: Dielectric resonator enclosed by a cavity

In the full-wave analysis of a dielectric resonator enclosed in a metallic cavity, it is necessary to solve the following boundary value problem:

$$\nabla \times \left(\frac{1}{\mu_r} \nabla \times \mathbf{E} \right) - k_o^2 \epsilon_r \mathbf{E} = -j k_o Z_o \mathbf{J} \tag{4.1.1}$$

$$\nabla \times \left(\frac{1}{\epsilon_r} \nabla \times \mathbf{H} \right) - k_o^2 \mu_r \mathbf{H} = \nabla \times \left(\frac{1}{\epsilon_r} \mathbf{J} \right) \tag{4.1.2}$$

Boundary conditions often encountered for electrically conducting surfaces are

$$\hat{n} \times \mathbf{E} = 0 \tag{4.1.3}$$

$$\hat{n} \times \nabla \times \mathbf{H} = 0 \tag{4.1.4}$$

and magnetically conducting surfaces are

$$\hat{n} \times \mathbf{H} = 0 \tag{4.1.5}$$

$$\hat{n} \times \nabla \times \mathbf{E} = 0 \tag{4.1.6}$$

4.2 Variational Formulation

Given the boundary-value problem as shown in Figure 4.1, consider the vector wave equation from Equation 4.1.1,

$$\nabla \times \left(\frac{1}{\mu_r} \nabla \times \mathbf{E} \right) - k_o^2 \epsilon_r \mathbf{E} = -jk_o Z_o \mathbf{J}$$

Let the operator L be

$$L = \nabla \times \left(\frac{1}{\mu_r} \nabla \times \right) - k_o^2 \epsilon_r \tag{4.2.1}$$

and according the definition of the inner product,

$$\langle L\mathbf{E}, \mathbf{F} \rangle = \int\int\int_V \mathbf{F}^* \cdot \left[\nabla \times \left(\frac{1}{\mu_r} \nabla \times \mathbf{E} \right) - k_o^2 \epsilon_r \mathbf{E} \right] dV \tag{4.2.2}$$

Using the second vector Green's theorem,

$$\begin{aligned} &\int\int\int_V [b \cdot (\nabla \times u \nabla \times a) - a.(\nabla \times u \nabla \times b)] dV \\ &\qquad = \oint_S u(a \times \nabla \times b - b \times \nabla \times a) \cdot \hat{n} dS \end{aligned} \tag{4.2.3}$$

the following equation is obtained:

$$\begin{aligned} \langle L\mathbf{E}, \mathbf{F} \rangle &= \int\int\int_V \mathbf{E} \cdot \left[\nabla \times \left(\frac{1}{\mu_r} \nabla \times \mathbf{F}^* \right) - k_o^2 \epsilon_r \mathbf{F}^* \right] dV \\ &+ \int\int_S \frac{1}{\mu_r} [\mathbf{E} \times (\nabla \times \mathbf{F}^*) - \mathbf{F}^* \times (\nabla \times \mathbf{E})] \cdot \hat{n} dS \end{aligned} \tag{4.2.4}$$

Using the identity,

$$[\mathbf{E} \times (\nabla \times \mathbf{F}^*)] \cdot \hat{n} = (\hat{n} \times \mathbf{E}) \cdot (\nabla \times \mathbf{F}^*) = -\mathbf{E} \cdot [\hat{n} \times (\nabla \times \mathbf{F}^*)] \tag{4.2.5}$$

and if both $\mathbf{E}$ and $\mathbf{F}$ satisfy the homogeneous Dirichlet boundary condition,

$$\hat{n} \times \mathbf{E} = 0 \quad \textit{on the cavity walls } S_1 \tag{4.2.6}$$

and the homogeneous Neumann boundary condition of the third kind

$$\frac{1}{\mu_r}\hat{n} \times (\nabla \times \mathbf{E}) + \gamma_e \hat{n} \times (\hat{n} \times \mathbf{E}) = 0 \quad \textit{on } S_2 \tag{4.2.7}$$

with $S_1 + S_2 = S$, the surface integral in equation 4.2.4 vanishes on the condition that both γ_e and μ_r are real. In addition, if both ϵ_r and μ_r are real, equation 4.2.4 can be expressed as

$$\langle L\mathbf{E}, \mathbf{F} \rangle = \langle \mathbf{E}, L\mathbf{F} \rangle \tag{4.2.8}$$

and therefore, L is self-adjoint. When this condition is satisfied, the variational function can be constructed by substituting equation 4.2.1 into

$$F(\phi) = \frac{1}{2}\langle L\phi, \phi \rangle - \frac{1}{2}\langle \phi, f \rangle - \frac{1}{2}\langle f, \phi \rangle \tag{4.2.9}$$

where the angular brackets denote the inner product defined by

$$\langle \phi, \psi \rangle = \int_\Omega \phi \psi^* d\Omega \tag{4.2.10}$$

and Ω denotes the domain of the problem with the asterisk implying complex conjugate operation, the following equation is subsequently obtained:

$$\begin{aligned} F(\mathbf{E}) &= \frac{1}{2}\int\int\int_V \mathbf{E}^* \cdot \left[\nabla \times \left(\frac{1}{\mu_r}\nabla \times \mathbf{E}\right) - k_o^2 \epsilon_r \mathbf{E}\right] dV \\ &- \frac{jk_o Z_o}{2}\int\int\int_V (\mathbf{E} \cdot \mathbf{J}^* - \mathbf{E}^* \cdot \mathbf{J}) dV \end{aligned} \tag{4.2.11}$$

Making use of the first vector Green's theorem,

$$\begin{aligned} &\int\int\int_V [u(\nabla \times a) \cdot (\nabla \times b) - a \cdot (\nabla \times u\nabla \times b)] dV \\ &\qquad = \int\int_S u(a \times \nabla \times b) \cdot \hat{n} dS \end{aligned} \tag{4.2.12}$$

and boundary conditions (4.2.6) and (4.2.7), the following equation is obtained:

$$\begin{aligned} F(\mathbf{E}) &= \frac{1}{2}\int\int\int_V \left[\frac{1}{\mu_r}(\nabla\times\mathbf{E})\cdot(\nabla\times\mathbf{E})^* - k_o^2\epsilon_r\mathbf{E}.\mathbf{E}^*\right]dV \\ &+ \frac{jk_oZ_o}{2}\int\int\int_V(\mathbf{E}^*\cdot\mathbf{J}-\mathbf{E}\cdot\mathbf{J}^*)dV \\ &+ \frac{1}{2}\int\int_{S_2}\gamma_e(\hat{n}\times\mathbf{E})\cdot(\hat{n}\times\mathbf{E}^*)dS \end{aligned} \tag{4.2.13}$$

Since there is no excitation, $J = 0$ and applying the Dirichlet boundary condition, the following equation is hence obtained:

$$F(\mathbf{E}) = \frac{1}{2}\int\int\int_V \left[\frac{1}{\mu_r}(\nabla\times\mathbf{E})\cdot(\nabla\times\mathbf{E})^* - k_o^2\epsilon_r\mathbf{E}\cdot\mathbf{E}^*\right]dV \tag{4.2.14}$$

where $k_o = w^2\mu_o\epsilon_o$. From the above equation, it can be observed that both $\nabla\times\mathbf{E}$ and $\mathbf{E}$ need to be square integrable.

4.3 Finite Element Numerical Procedures

4.3.1 Domain Discretization

The variational formulation in the previous section seeks to find the solution in the infinite-dimensional functional space. In order to solve the three-dimensional cavity problem, there is a need to convert the original continuum problem into a discretized version using finite element method. It this way, the solution space has been restricted to a smaller, finite dimensional function space which can be described by a finite number of parameters (the degrees of freedom). When this constraint is imposed properly, stationary will occur at a point which is in the neighbourhood of the true solution and leads to a finite number of equations with respect to the degrees of freedom. Hence, from the original variational equation 4.2.14:

$$F(\mathbf{E}) = \frac{1}{2}\int\int\int_V \left[\frac{1}{\mu_r}(\nabla\times\mathbf{E})\cdot(\nabla\times\mathbf{E})^* - k_o^2\epsilon\mathbf{E}\cdot\mathbf{E}^*\right]dV$$

where V being the volume of the cavity. F can be numerically discretized by subdividing the volume V into small tetrahedral with volume V^e (e=1,2,3,...,M), where M is

the total number of elements. Within each element, the electric field is approximated as

$$E^e = \sum_{i=1}^{n} N_i^e E_i^e = \{E^e\}^T\{N^e\} = \{N^e\}^T\{E^e\} \tag{4.3.1}$$

where N_i^e are the vector basis functions, E_i^e denote the expansion coefficients of the basis functions and n represents the number of edges comprising the element. Substituting (4.3.1) into (4.2.14), the following matrix form can be attained:

$$F = \frac{1}{2}\sum_{e=1}^{M}(\{E^e\}^T[A^e]\{E^e\} - k_o^2\{E^e\}^T[B^e]\{E^e\}) \tag{4.3.2}$$

where

$$[A^e] = \int\int\int_{V^e} \frac{1}{\mu_r^e}\{\nabla \times N^e\} \cdot \{\nabla \times N^e\}^T dV \tag{4.3.3}$$

$$[B^e] = \int\int\int_{V^e} \epsilon_r^e\{N^e\} \cdot \{N^e\}^T dV \tag{4.3.4}$$

Once the summation is carried out and using global notation, equation 4.3.2 can be expressed as

$$F = \frac{1}{2}(\{E\}^T[A]\{E\} - k_o^2\{E\}^T[B]\{E\}) \tag{4.3.5}$$

An eigenvalue system is subsequently obtained by applying the Ritz procedure, which involved taking partial derivative of F with respect to each unknown edge field and setting the result to zero. Hence, the following result is obtained:

$$[A]\{E\} = k_o^2[B]\{E\} \tag{4.3.6}$$

4.3.2 Elemental Interpolation

Once the domain has been discretized, the next step is to approximate the unknown function within each element (Figure 4.2). Within each element, the unknown func-

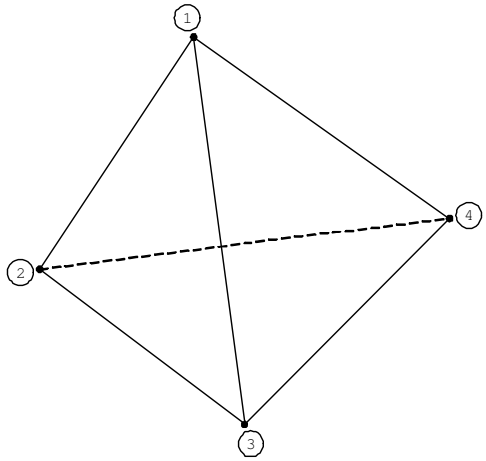

Figure 4.2: Linear tetrahedral element

tion ϕ can be approximated as

$$\phi^e(x, y, z) = a^e + b^e x + c^e y + d^e z \tag{4.3.7}$$

where the four unknown coefficients a^e, b^e, c^e and d^e can be determined by enforcing equation (4.3.7) at the four nodes of the element. Hence, the following four equations are obtained:

$$\phi_1^e = a^e + b^e x_1^e + c^e y_1^e + d^e z_1^e \tag{4.3.8}$$

$$\phi_2^e = a^e + b^e x_2^e + c^e y_2^e + d^e z_2^e \tag{4.3.9}$$

$$\phi_3^e = a^e + b^e x_3^e + c^e y_3^e + d^e z_3^e \tag{4.3.10}$$

$$\phi_4^e = a^e + b^e x_4^e + c^e y_4^e + d^e z_4^e \tag{4.3.11}$$

where ϕ_j^e refers to the value of ϕ at the jth node. Solving the above four simultaneous equations, the following unknown coefficients are thus found to be:

$$a^e = \frac{1}{6V^e}\begin{vmatrix} \phi_1^e & \phi_2^e & \phi_3^e & \phi_4^e \\ x_1^e & x_2^e & x_3^e & x_4^e \\ y_1^e & y_2^e & y_3^e & y_4^e \\ z_1^e & z_2^e & z_3^e & z_4^e \end{vmatrix} = \frac{1}{6V^e}(a_1^e\phi_1^e + a_2^e\phi_2^e + a_3^e\phi_3^e + a_4^e\phi_4^e) \quad (4.3.12)$$

$$b^e = \frac{1}{6V^e}\begin{vmatrix} 1 & 1 & 1 & 1 \\ \phi_1^e & \phi_2^e & \phi_3^e & \phi_4^e \\ y_1^e & y_2^e & y_3^e & y_4^e \\ z_1^e & z_2^e & z_3^e & z_4^e \end{vmatrix} = \frac{1}{6V^e}(b_1^e\phi_1^e + b_2^e\phi_2^e + b_3^e\phi_3^e + b_4^e\phi_4^e) \quad (4.3.13)$$

$$c^e = \frac{1}{6V^e}\begin{vmatrix} 1 & 1 & 1 & 1 \\ x_1^e & x_2^e & x_3^e & x_4^e \\ \phi_1^e & \phi_2^e & \phi_3^e & \phi_4^e \\ z_1^e & z_2^e & z_3^e & z_4^e \end{vmatrix} = \frac{1}{6V^e}(c_1^e\phi_1^e + c_2^e\phi_2^e + c_3^e\phi_3^e + c_4^e\phi_4^e) \quad (4.3.14)$$

$$d^e = \frac{1}{6V^e}\begin{vmatrix} 1 & 1 & 1 & 1 \\ x_1^e & x_2^e & x_3^e & x_4^e \\ y_1^e & y_2^e & y_3^e & y_4^e \\ \phi_1^e & \phi_2^e & \phi_3^e & \phi_4^e \end{vmatrix} = \frac{1}{6V^e}(d_1^e\phi_1^e + d_2^e\phi_2^e + d_3^e\phi_3^e + d_4^e\phi_4^e) \quad (4.3.15)$$

with volume of the eth element, V^e given as

$$V^e = \frac{1}{6}\begin{vmatrix} 1 & 1 & 1 & 1 \\ x_1^e & x_2^e & x_3^e & x_4^e \\ y_1^e & y_2^e & y_3^e & y_4^e \\ z_1^e & z_2^e & z_3^e & z_4^e \end{vmatrix} \quad (4.3.16)$$

The coefficients a_j^e, b_j^e, c_j^e and d_j^e can be determined from expansion of the determinants (refer to Appendix A), where $j = 1, 2, 3, 4$. Substituting the expressions for a^e, b^e, c^e *and* d^e back into (4.3.7), the following equation is obtained:

$$\phi^e(x, y, z) = \sum_{j=1}^{4} N_j^e(x, y, z)\phi_j^e \quad (4.3.17)$$

where the interpolation functions

$$N_j^e(x, y, z) = \frac{1}{6V^e}(a_j^e + b_j^e x + c_j^e y + d_j^e z) \quad (4.3.18)$$

and the interpolation functions have the property of

$$N_j^e(x_i, y_i, z_i) = \delta_{ij} = \begin{cases} 1 & (i = j) \\ 0 & (i \neq j) \end{cases} \tag{4.3.19}$$

and in addition, $N_j^e(x, y, z)$ varnishes when the observation point is on the tetrahedron surface opposite the jth node. This is to ensured inter-element continuity of the interpolated function.

4.3.3 Tangential Vector Finite Elements

In the previous section, linear interpolation functions for the tetrahedral elements has been derived. Consider the vector function

$$W_{12} = L_1^e \nabla L_2^e - L_2^e \nabla L_1^e \tag{4.3.20}$$

As before, L_1^e is a linear function that varies from one at node 1 to zero at node 2 and in a similar way, L_2^e is a linear function which varies from one at node 2 to zero at node 1. Also, the vector function W_{12} satisfies the following properties

$$\begin{aligned} \nabla \cdot W_{12} &= 0 \\ \nabla \times W_{12} &= 2\nabla L_1^e \times \nabla L_2^e \\ e_1 \cdot W_{12} &= \frac{L_1^e + L_2^e}{l_1^e} = \frac{1}{l_1^e} \end{aligned} \tag{4.3.21}$$

where e_1 refers to a unit vector pointing from node 1 to node 2, such that $e_1 \cdot \nabla L_1^e = -1/l_1^e$ and $e_1 \cdot \nabla L_2^e = 1/l_1^e$. Parameter l_1^e denotes the length of the edge connecting nodes 1 and 2. This implies that W_{12} has a constant tangential component along edge $(1 \rightarrow 2)$ and no tangential component along any other five edges. In addition, W_{12} has no tangential component along element facet (2,3,4) and (1,3,4). Tangential component only exist on element facets that contain edge (1,2). Thus, W_{12} possesses the necessary requirements to be a vector basis function for the edge field associated with edge (1,2). Hence, the vector basis functions for the six edges are expressed as:

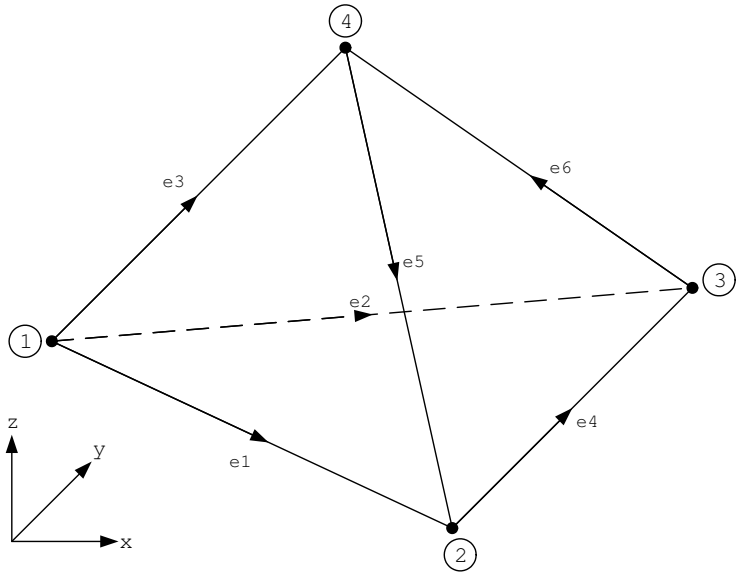

Figure 4.3: Tetrahedral element

Edge i	Node i_1	Node i_2
1	1	2
2	1	3
3	1	4
4	2	3
5	4	2
6	3	4

Table 4.1: Edge definition for tetrahedral element

$$N_1^e = W_{12} l_1^e = (L_1^e \nabla L_2^e - L_2^e \nabla L_1^e) l_1^e$$

$$N_2^e = W_{13} l_2^e = (L_1^e \nabla L_3^e - L_3^e \nabla L_1^e) l_2^e$$

$$N_3^e = W_{14} l_3^e = (L_1^e \nabla L_4^e - L_4^e \nabla L_1^e) l_3^e$$

$$N_4^e = W_{23} l_4^e = (L_2^e \nabla L_3^e - L_3^e \nabla L_2^e) l_4^e$$

$$N_5^e = W_{42} l_5^e = (L_4^e \nabla L_2^e - L_2^e \nabla L_4^e) l_5^e$$

$$N_6^e = W_{34} l_6^e = (L_3^e \nabla L_4^e - L_4^e \nabla L_3^e) l_6^e$$

where the vector basis function for edge i can be simplified as

$$N_i^e = W_{i_1 i_2} l_i^e = (L_{i_1}^e \nabla L_{i_2}^e - L_{i_2}^e \nabla L_{i_1}^e) l_i^e \tag{4.3.22}$$

where the local edge numbers i $(= 1, 2, 3, \ldots, 6)$ and their respective nodes i_1 and i_2 are defined in Table 4.3.3. V^e refers to the volume of the tetrahedral element and $l_i^e = |r_{i_2}^e - r_{i_1}^e|$ is the length of the ith edge with $r_{i_1}^e$ and $r_{i_2}^e$ denote the locations of the nodes i_1 and i_2 of the eth element respectively.

In general, the implementation of the above discretization will involve two numbering systems and thus some unique global edge direction must be defined to ensure continuity of $\hat{n} \times E$ across all edges. Finally, since $\nabla \cdot W_i^e = 0$, the electric field obtained from the solution of (4.3.2) satisfies the divergence equation within each element. Hence, the solution will be free from contamination due to spurious solutions.

4.3.4 Evaluation of Elemental Matrices

When the vector basis functions in the previous section are used for the three-dimensional finite element discretization of a vector wave equation, the resulting elemental matrices are obtained:

$$E_{ij}^e = \int_{V^e} (\nabla \times N_i^e) \cdot (\nabla \times N_j^e) dV \tag{4.3.23}$$

$$F_{ij}^e = \int_{V^e} N_i^e \cdot N_j^e dV \tag{4.3.24}$$

These two integrals are subsequently evaluated analytically for tetrahedral elements. Since

$$\begin{aligned} \nabla \times N_i^e &= 2 l_i^e \nabla L_{i_1}^e \times \nabla L_{i_2}^e \\ &= \frac{l_i^e}{(6V^e)^2} [(c_{i_1}^e d_{i_2}^e - d_{i_1}^e c_{i_2}^e)\hat{x} + (d_{i_1}^e b_{i_2}^e - b_{i_1}^e d_{i_2}^e)\hat{y} + (b_{i_1}^e c_{i_2}^e - c_{i_1}^e b_{i_2}^e)\hat{z} \end{aligned} \tag{4.3.25}$$

and

$$N_i^e \cdot N_j^e = \frac{l_i^e l_j^e}{(6V^e)^2} [L_{i_1}^e L_{j_1}^e f_{i_2 j_2} - L_{i_1}^e L_{j_2}^e f_{i_2 j_1} - L_{i_2}^e L_{j_1}^e f_{i_1 j_2} + L_{i_2}^e L_{j_2}^e f_{i_1 j_1}] \tag{4.3.26}$$

where $f_{ij} = b_i^e b_j^e + c_i^e c_j^e + d_i^e d_j^e$. Hence, the elemental matrices become

$$E_{ij}^e = \frac{4 l_i^e l_j^e V^e}{(6V^e)^4} \quad [(c_{i_1}^e d_{i_2}^e - d_{i_1}^e c_{i_2}^e)(c_{j_1}^e d_{j_2}^e - d_{j_1}^e c_{j_2}^e)$$
$$+(d_{i_1}^e b_{i_2}^e - b_{i_1}^e d_{i_2}^e)(d_{j_1}^e b_{j_2}^e - b_{j_1}^e d_{j_2}^e)$$
$$+(b_{i_1}^e c_{i_2}^e - c_{i_1}^e b_{i_2}^e)(b_{j_1}^e c_{j_2}^e - c_{j_1}^e b_{j_2}^e)] \tag{4.3.27}$$

and

$$\begin{aligned}
F_{11}^e &= \frac{(l_1^e)^2}{360V^e}(f_{22} - 2f_{12} + f_{11}) \\
F_{12}^e &= \frac{l_1^e l_2^e}{720V^e}(2f_{23} - f_{21} - f_{13} + f_{11}) \\
F_{13}^e &= \frac{l_1^e l_3^e}{720V^e}(2f_{24} - f_{21} - f_{14} + f_{11}) \\
F_{14}^e &= \frac{l_1^e l_4^e}{720V^e}(f_{23} - f_{22} - 2f_{13} + f_{12}) \\
F_{15}^e &= \frac{l_1^e l_5^e}{720V^e}(f_{22} - f_{24} - f_{12} + 2f_{14}) \\
F_{16}^e &= \frac{l_1^e l_6^e}{720V^e}(f_{24} - f_{23} - f_{14} + f_{13}) \\
F_{22}^e &= \frac{(l_2^e)^2}{360V^e}(f_{33} - 2f_{13} + f_{11}) \\
F_{23}^e &= \frac{l_2^e l_3^e}{720V^e}(2f_{34} - 2f_{13} - 2f_{14} + f_{11}) \\
F_{24}^e &= \frac{l_2^e l_4^e}{720V^e}(f_{33} - f_{23} - f_{13} + 2f_{12}) \\
F_{25}^e &= \frac{l_2^e l_5^e}{720V^e}(f_{23} - f_{34} - f_{12} + f_{14}) \\
F_{26}^e &= \frac{l_2^e l_6^e}{720V^e}(f_{13} - f_{33} - 2f_{14} + f_{34}) \\
F_{33}^e &= \frac{(l_3^e)^2}{360V^e}(2f_{44} - 2f_{14} + f_{11}) \\
F_{34}^e &= \frac{l_3^e l_4^e}{720V^e}(f_{34} - f_{24} - f_{13} + f_{12}) \\
F_{35}^e &= \frac{l_3^e l_5^e}{720V^e}(f_{24} - f_{44} - 2f_{12} + f_{14}) \\
F_{36}^e &= \frac{l_3^e l_6^e}{720V^e}(f_{44} - f_{34} - f_{14} + 2f_{13}) \\
F_{44}^e &= \frac{(l_4^e)^2}{360V^e}(f_{33} - 2f_{23} + f_{22}) \\
F_{45}^e &= \frac{l_4^e l_5^e}{720V^e}(f_{23} - 2f_{34} - f_{22} + f_{24}) \\
F_{46}^e &= \frac{l_4^e l_6^e}{720V^e}(f_{34} - f_{33} - 2f_{24} + f_{23})
\end{aligned}$$

$$
\begin{aligned}
F^e_{55} &= \frac{(l^e_5)^2}{360V^e}(f_{22} - 2f_{24} + f_{44}) \\
F^e_{56} &= \frac{l^e_5 l^e_6}{720V^e}(f_{24} - 2f_{23} - f_{44} + f_{34}) \\
F^e_{66} &= \frac{(l^e_6)^2}{360V^e}(f_{44} - 2f_{34} + f_{33})
\end{aligned} \tag{4.3.28}
$$

4.4 Software Implementation

Based on the finite element formulation mentioned in the previous sections, several subroutines are written in Matlab to facilitate the solving of eigenvalues for the case of a dielectric resonator within a metallic cavity. In this section, an overview of the Matlab codes will be presented for easy usage of the FEM codes (Appendix B).

4.4.1 Software Overview

The written codes are capable of generating the necessary matrices, formulating the eigenvalue equation and solving the resultant matrices. The codes require the user to input the following:

1. Generate the meshes using commercial softwares (For example: Gmsh and GID 7.2).

2. Permittivity of the dielectric resonator and supporting substrate.

3. Size of the metallic cavity box.

The Matlab codes will subsequently output the computed results as text files. The output files consist of a list of assigned edges, assigned global edge for each elements and most important of all, the eigenvalues of the dielectric resonator and metallic cavity.

4.4.2 Code Descriptions

FEDGE.M: This program is used for assigning numbers to each unique edges after generating the mesh using commercial software (GID 7.2). The mesh generator will mesh the object drawn and provide two files: "Element.txt" and "Global.txt". "Element.txt" comprises of all the tetrahedral elements with their corresponding global nodes. On the other hand, "Global.txt" will contain x, y and z coordinates of each global coordinates. "Element.txt" consists of a (n×4) matrix as shown in Figure 4.4.

Element	Local Nodes			
	1	2	3	4
1	6	8	20	11
2	6	8	11	5
3	6	8	5	4
.	.	.	.	.
.	.	.	.	.
.	.	.	.	.
.	.	.	.	.
222	54	38	60	47

Figure 4.4: Example of element.txt generated using mesh generator GID 7.2

where n refers to the number of tetrahedral elements and is also the number of rows for the matrix. The first column contains all the first nodes of the n tetrahedral elements. Similarly, each columns comprised of their respective local nodes. The data stored within each row and column are the global edges. Hence, from Figure 4.4, we can see that there are a total of 222 tetrahedral elements. Matrix of element.txt with (row,column)=(222,2) contains global node 38. The row refers to the 222nd tetrahedral element and this corresponds to the 2nd local node. The output files "fedge.txt" and "edge.txt" are required by "GEDGE.M".

File "fedge.txt" consists of a m×2 matrix as shown in Figure 4.5:

Edge	Local Nodes	
	1	2
1	6	8
2	6	20
3	6	11
⋮	⋮	⋮
100	17	38
101	38	22
⋮	⋮	⋮
340	70	65
341	62	70

Figure 4.5: Example of fedge.txt generated from FEDGE.M

In this file, the number of rows m are the number of unique edges. For example, the 100th edge is defined by the first local node 17 and the second local node 38. The assumed positive direction of the vector along the edge is from global node 17 →38.

GEDGE.M This program is used to identify the six global edges of each tetrahedral elements and arrange them according to the order shown in Figure 4.6.

Element	Local Edges					
	1	2	3	4	5	6
1	1	2	3	4	5	6
2	1	3	7	-5	8	9
3	1	7	10	-8	11	12
⋮	⋮	⋮	⋮	⋮	⋮	⋮
222	212	-222	-226	-300	314	-329

Figure 4.6: Example of gedge.txt generated from GEDGE.M

The inputs for this code are “Element.txt”, “fedge.txt” and “edge.txt”. The output file comprised of a n×6 matrix, where each row represents the number of elements and each column corresponds to each of the six local edges. Some of the global edges are negative and this indicates opposite direction to the assumed direction to ensure continuity at all the edges. The assumed direction for edges can be found in “fedge.txt”.

BEDGE.M The purpose of this code is to identify edges on the boundary of the metallic cavity. This program requires the user to input the dimensions of the metallic cavity. The output file “bedge.txt” contains all the edges on the metallic boundary.

CAVITY.M This is the main program which requires output files generated by the earlier codes. These include: Global.txt, Element.txt, gedge.txt and fedge.txt. The code first computes the element matrices and subsequently, the elemental matrices add up to give the global matrices. Finally, the matrices are solved for their eigenvalues using eigenvalue solver package available in matlab.

Chapter 5

Design Methodology of the Dielectric Resonator Antenna

5.1 Introduction

In the previous section, an accurate characterization of the DR has been proposed so that the resonator's size can be carefully chosen for optimal performance. Now, design methodology for the feeding mechanism is presented. Dielectric resonator antennas (DRAs) are gaining popularity because of their various merits. These include its higher radiation efficiency ($> 90\%$), due to the lack of conductor loss and surface wave loss. Various resonator shapes (cylindrical, rectangular and hemispherical) can be chosen. There is also no need for special feeding technique. In fact, simple feeding mechanism such as probe-feeding, coplanar waveguide, microstrip line and aperture-coupling are existing technologies that can be employed. Various modes can be excited depending on the desired radiation patterns. In addition, there is a wide range of permittivity values to choose from and this gives designers a lot of flexibility in choosing the antenna size and bandwidth. The aim of this design is to achieve an integrated dielectric resonator antenna with wide impedance bandwidth ($> 10\%$). Efforts are also made to obtain a smooth and symmetrical radiation pattern.

5.2 Conventional DRAs

Examples of some conventional DRAs are shown in Figure 5.1. As observed, the actual size of the antenna includes the finite size ground plane which has an influence on the antenna's return loss and radiation patterns.

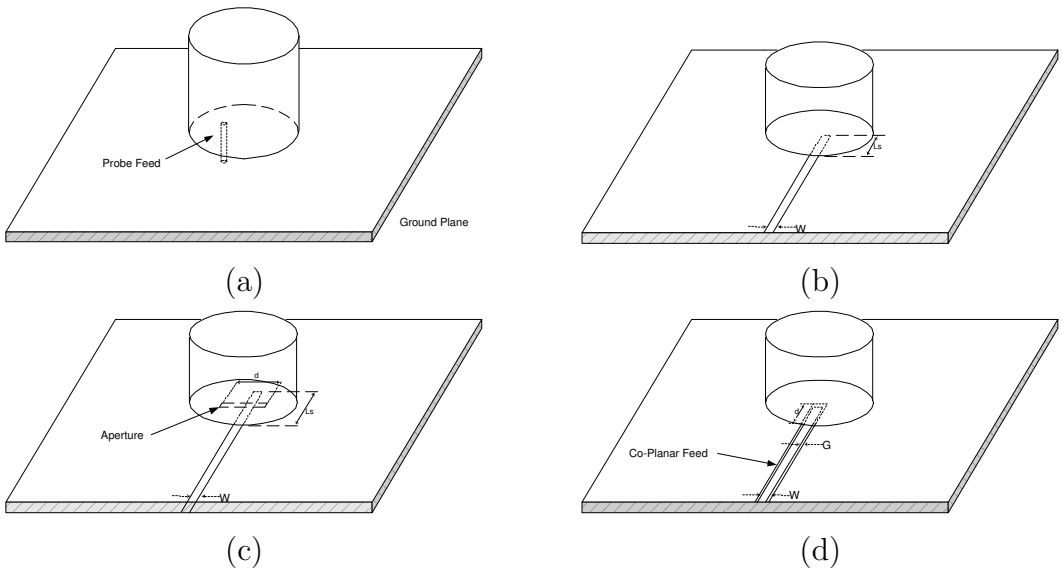

Figure 5.1: Examples of some conventional DRAs: (a)Probe Feed (b)Microstripline Feed (c)Aperture Feed (d)Coplanar waveguide Feed

In addition, tuning the resonator placed on substrate has been a major problem for traditional DRAs. However, the proposed antenna is able to advert this problem because feeding substrate is placed inside the DRA. The problem of tuning is resolved as position of the substrate (RF Micro-module) is fixed. Therefore, the DRA can be fixed to external substrate easily, with no requirement for very accurate placing of the device. Beside problems associate with traditional DRAs, there are also inherent limitations of a small antenna which will be discussed in the next section.

5.3 Fundamental Limitations of a small antenna

Design of compact and fully integrated antennas is a major challenge in development of modern RF front end products for wireless communications. The conventional integrated patch antennas suffer from low efficiency, high sensitive fabrication tolerances, and narrow bandwidth. Due to the size constraint, integrated antennas are often small or electrically small. Small antennas inherently have low radiation resistance, low radiation efficiency and narrow bandwidth. The antenna's Q-factor (quality factor) increases at a high rate when the antenna size gets smaller. Small antenna usually have very sensitive tolerances. Hence, the near field distribution may affect the antenna input impedance greatly causing mismatch between the radiating elements and the rest of the circuits. To achieve a smaller size, high dielectric constant substrates are often used. However, this would reduce the radiation efficiency drastically. For a conventional microstrip antenna using high dielectric constant substrate (silicon), the radiation efficiency can be as low as about 20%. Another problem is that the antenna must operate with a finite "ground plane", which has a great impact on the return loss and causes new resonances. The finite ground plane acts as part of a radiator and often cause scalloping in the radiation pattern. It also results in the antenna having a low forward-backward ratio. Hence, the design process becomes more complex. Electrically small antennas are neither balanced nor unbalanced. As a result, return currents flow along the coaxial cable and radiate. During measurement of the antenna's radiation patterns, the higher gain measured could be the result of long and radiating RF feeding cable. To overcome these problems, special precautions must be taken during antenna measurement.

5.4 Antenna measurement for small antenna

Because of the limitations of small antenna mentioned in the earlier section, there are a few concerns during the measurement of a small antenna. The reduction of antenna size results in introducing more challenging problems in antenna measurement. One of the difficulties involved is how to determine the small impedance and low efficiency with precision. Measurements of a small antenna often involve proximity effects and it is important for designers to be wary of such effects.

Environment effects include coupling of the antenna with nearby materials. When the size of the antenna under test is comparable to or smaller than that of the instrument connected to the test antenna, electromagnetic coupling is likely to exist between the antenna element and nearby objects, such as the RF cables and instruments. For example, if a coaxial cable connected to an antenna element has a comparatively larger size than the antenna under test, and it runs very closely to the antenna element, the cable couples electromagnetically with the antenna element and the impedance of the antenna may be measured with an error. The length and thick-

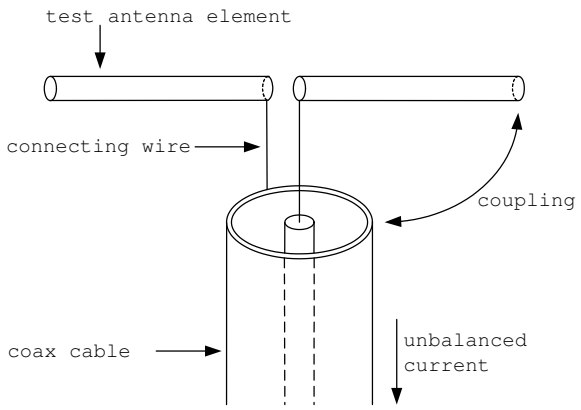

Figure 5.2: Small antenna and connecting cable

ness of the connecting wire from the cable to the antenna feed point should be short enough to avoid the inclusion of an extra impedance of the connecting wire because

the antenna impedance might be comparable to or smaller than the wire impedance when the size of the antenna becomes extremely small. If any object exists near an antenna element, especially near the feed point, it may have some influence on the antenna characteristics. The antenna feed point is such an important aspect during fabrication that anything which interacts with the antenna current must be removed. It is observed that how good the impedance bandwidth depends on how good is the connection between the probe and the coplanar waveguide feed. Hence, a via connection is suggested. Comparison of return loss using normal probe connection and one using a via connection shows the latter more superior and gives more consistent measurement results. In addition to a better contact, it can also minimized the air gap between the substrate and the resonator.

Another important problem is to suppress the unbalanced currents that may flow on the outside of the coaxial cable and generate undesired radiation. Simulation of the antenna has shown that radiation pattern can be affected by the length of the connecting coaxial cable. The higher gain measured could be due to the long and radiating coaxial cable. Hence, it is very important to ensure RF cables are well-covered with absorbers during measurement in the anechoic chamber.

Finally, it is not an easy task to measure the phase of a small antenna accurately. Correct measurement of a small antenna's phase has been found to be very crucial for the measurement of an electrically small antenna with circular polarization. Special attention has to be given to the connectors and cables used during the measurement. Even though a L-shape connectors may not affect the magnitude of the radiation pattern significantly, it has been found to affect the phase of circular-polarized antenna substantially if it is not taken into account during the initial calibration process. Hence, all the connectors must be taken into account during calibration.

5.5 Proposed Antenna Structures

5.5.1 Linear and Circular-Polarized Antennas

The schematics of the proposed antennas, with linear-polarized (LP) and circular-polarized (CP) feed designs are shown in Figure 5.3 and 5.4 respectively. The potential advantages of using a DRA as compared to a conventional microstrip antenna include its significantly higher radiation efficiency and broader impedance bandwidth. Moreover, small physical dimensions of the antenna can be achieved by using higher permittivity ceramic material for the dielectric resonator whose physical dimension is proportional to $\lambda_o/\sqrt{\epsilon_r}$.

To overcome the finite "ground plane" problem, a feed structure comprising of a complementary pair of magnetic dipole and magnetic loop, modified to exclude the ground plane and optimized for a wider bandwidth has been proposed in Figure 5.3. The design parameters of the feed are chosen to allow a unidirectional radiation pattern away from the ground plane. So, the ground plane impact on the antenna parameters is significantly reduced allowing a compact design of the antenna system. The feed structure has metallization on all sides to prevent possible electromagnetic interference from the antenna on the RF circuitry. A probe is then used to excite the feed structure beneath the dielectric resonator. A similar design for circular-polarized antenna is shown in Figure 5.4 which has a meandering magnetic dipole as its feed design.

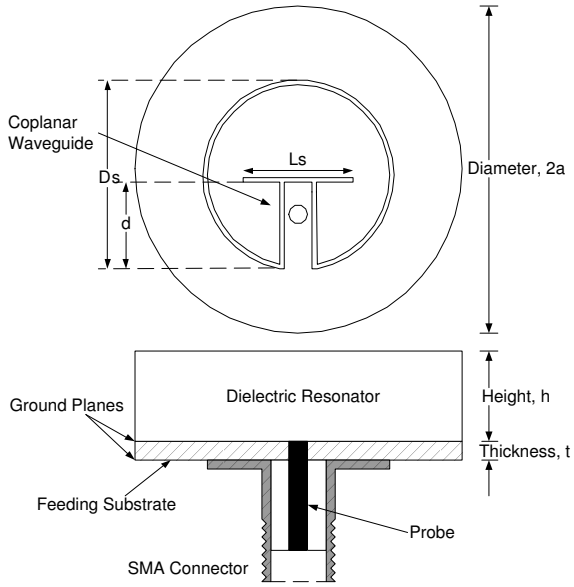

Figure 5.3: Schematics of the proposed linear-polarized DRA

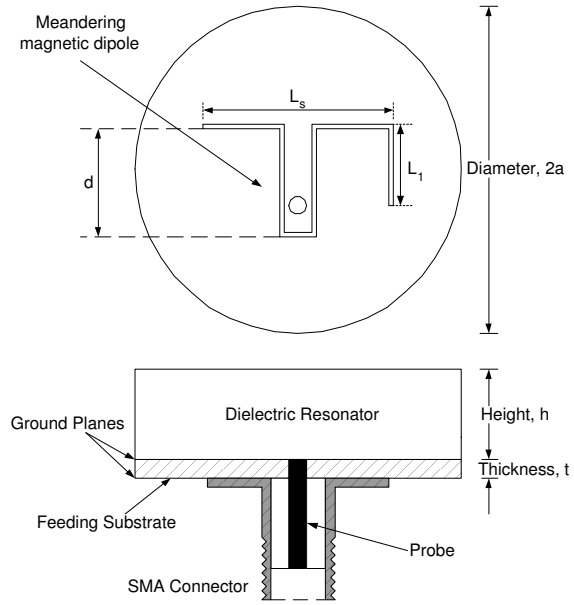

Figure 5.4: Schematics of the proposed circular-polarized DRA

5.5.2 Design Procedures

In this section, the design methodology for LP and CP dielectric resonator antennas are presented. The purpose of this investigation is to provide designers an easy and reliable way of designing the antenna.

Coplanar Waveguide Feed Design

The feeding mechanism of the antenna comprised of a coplanar waveguide (CPW) feed and the first step is to design the CPW feed for a 50Ω environment.

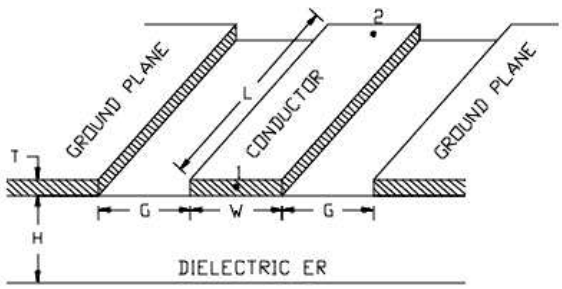

Figure 5.5: Coplanar Waveguide Feed

This can be easily done using Advanced Design System (ADS) to obtain the desired center conductor width (W) and gap (G) between the center conductor and the ground plane. The slot width of the magnetic loop and magnetic dipole is set at this value of G throughout the optimization process.

Parametric Study of a LP Antenna

Next, various parameters of the antenna are varied to ascertain their effects on the antenna's impedance loci. Simulated impedance loci of the antenna are plotted as a function of frequency in the smith chart , shown in Figure 5.7 - 5.11. The aim is to tune the impedance locus such that the "loop" is positioned at $Z_o = 50\Omega$ as shown in Figure 5.6. The simulated impedance loci comprised of 20 points, ranging from

3.5GHz to 4.5GHz with a step-size of 0.05GHz. These figures contain simulated loci for several values of the antenna parameters.

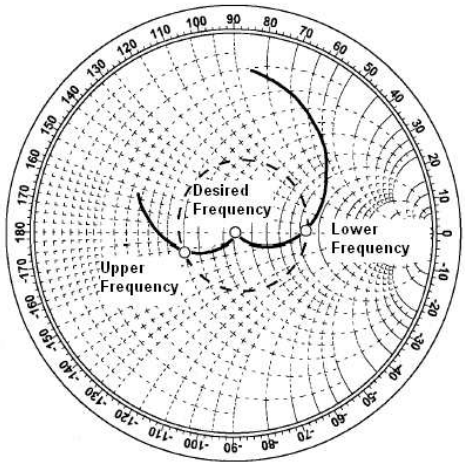

Figure 5.6: Desired Impedance Locus

The effect of varying length of the magnetic dipole, L_s is shown in Figure 5.7. If the input impedance at a single frequency (eg. 4.5GHz) is plotted for various L_s, the locus approximately follows a constant resistance contour. The impedance loci at the desired frequency band are not very sensitive to a slight change in L_s. As L_s increases, radius of the impedance locus widens with minimal shift in the position of the impedance loci "loop". Hence, this parameter is suitable for fine-tuning of the antenna's matching. Next, parameter d is varied at a step-size of 0.35mm to give the impedance loci presented in Figure 5.8. The shape of the impedance loci remains approximately the same, except for a clockwise rotation as d increases from 6.65mm to 7.70mm. At higher frequency, d has a bigger influence on the capacitive reactance component of the antenna's input impedance than L_s. Varying d while keeping all other parameters constant, is effectively changing the position of the magnetic dipole. Having observed the impedance loci's behaviour due to changes in L_s and d, the magnetic dipole behaves like a capacitive load.

The magnetic loop is next investigated. Size of the magnetic loop depends on the

magnetic loop's radius R_s. As R_s increased from 6.60mm to 7.85mm, the impedance locus widen noticeably. It is noted that increasing R_s also increase the value of d without affecting the position of the magnetic dipole. Hence, there is a slight clockwise shift in the impedance loci. Another useful parameter to play with is displacing the magnetic loop's center with respect to the resonator's center (positioned at (0,0)). It is observed that as the center of the magnetic loop is displaced further away from the reference position, the impedance locus shifted downwards with a slight rotation in the clockwise direction.

The position of the probe can also be adjusted to fine-tune the impedance locus because it affects the amplitude of the electric and magnetic fields excited within the dielectric resonator. As the location of the probe shifts from (3,0) to (6,0), the impedance locus shifted upward accordingly.

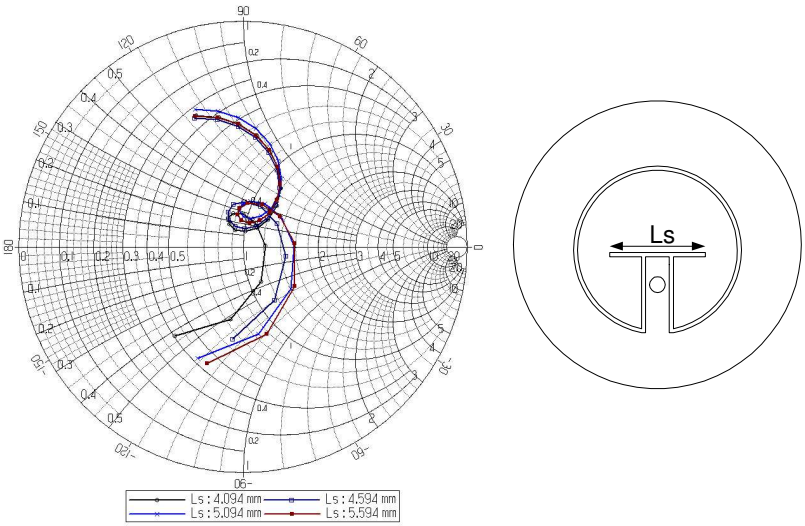

Figure 5.7: Variation of input impedance as a function of the magnetic dipole length L_s. Frequency increases clockwise with step of 0.05GHz. Center of Loop : (1.35,0), Rs = 7.15mm, d = 7.35mm

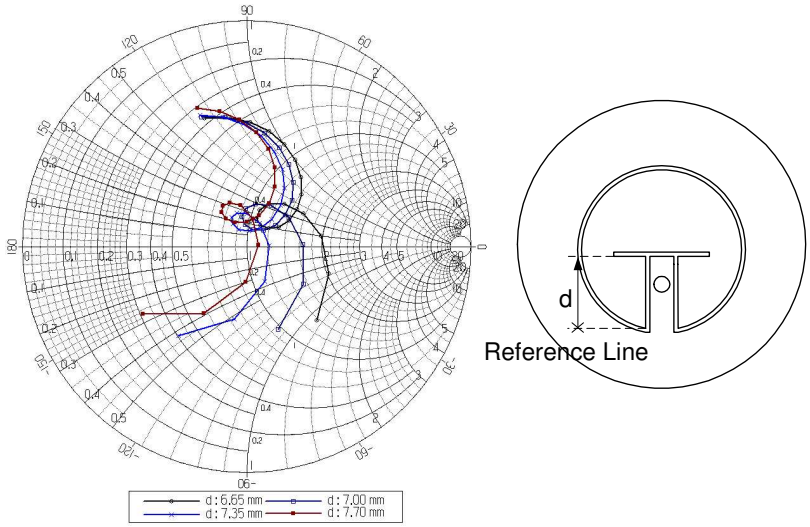

Figure 5.8: Variation of input impedance as a function of parameter d. Frequency increases clockwise with step of 0.05GHz. Center of Loop = (1.35,0), Rs = 7.15mm, Ls = 4.094mm

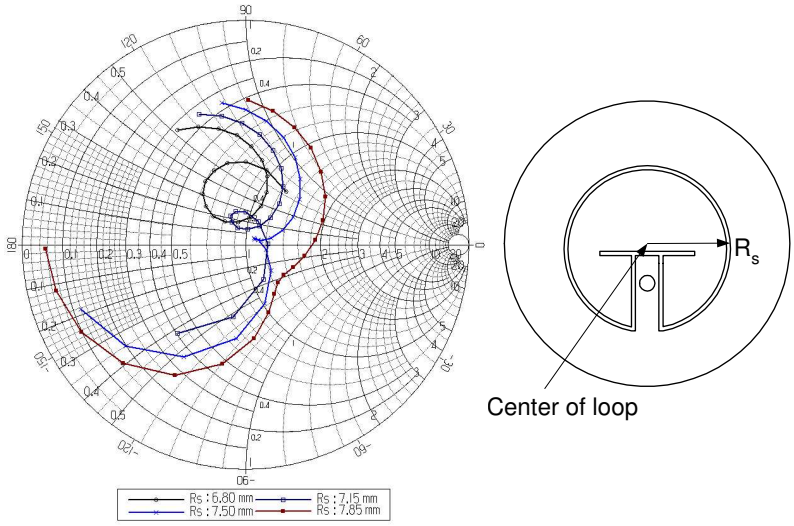

Figure 5.9: Variation of input impedance as a function of the magnetic loop radius R_s. Frequency increases clockwise with step of 0.05GHz. Center of Loop = (1.35,0), Ls = 4.094mm

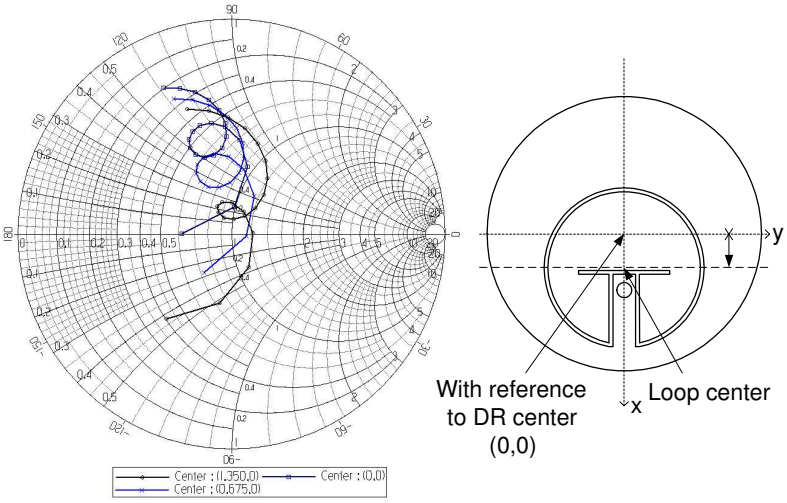

Figure 5.10: Variation of input impedance as a function of the magnetic loop center. Frequency increases clockwise with step of 0.05GHz. Ls = 4.094mm, Rs = 7.15mm, d = 7.35mm

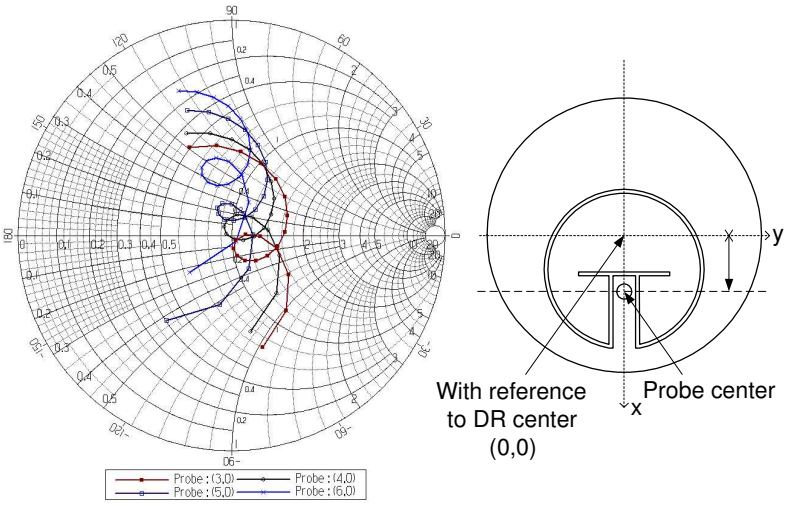

Figure 5.11: Variation of input impedance as a function of the probe position. Frequency increases clockwise with step of 0.05GHz. Center of Loop = (1.35,0), Ls = 4.094mm, Rs = 7.15mm, d = 7.35mm

Parametric Study of a CP Antenna

In this section, parameters such as L_s, L_1, d and the probe position are varied to determine their effects on the impedance locus. The meandering magnetic dipole comprised of vertical and horizontal slots. These vertical and horizontal slots are responsible for exciting two near-degenerate orthogonal modes of nearly equal amplitudes and 90° phase difference within the resonator. The parametric study will focus more on getting a broad impedance bandwidth first, before attempts to achieve circular-polarization.

The length of L_s is increased progressively in steps of 0.7mm to investigate the effects of horizontal slots on the impedance locus. As L_s increased, the radius of the impedance locus is observed to become slightly narrower with no obvious rotation. Next, length of the vertical slots can be varied by changing parameters such as L_1 and d. As L_1 is increased in steps of 0.5mm, the impedance locus widens with a slight clockwise rotation. L_1's influence on the impedance locus is more than the previous case when L_s is varied. Hence, L_s is suitable for fine tuning the impedance locus when a slight change is required for optimal bandwidth. When d is increased in steps of 0.35mm, radius of the impedance locus becomes narrower with no obvious rotation. Finally, changing location of the probe from (3,0) to (6,0), widens radius of the impedance locus with no rotation.

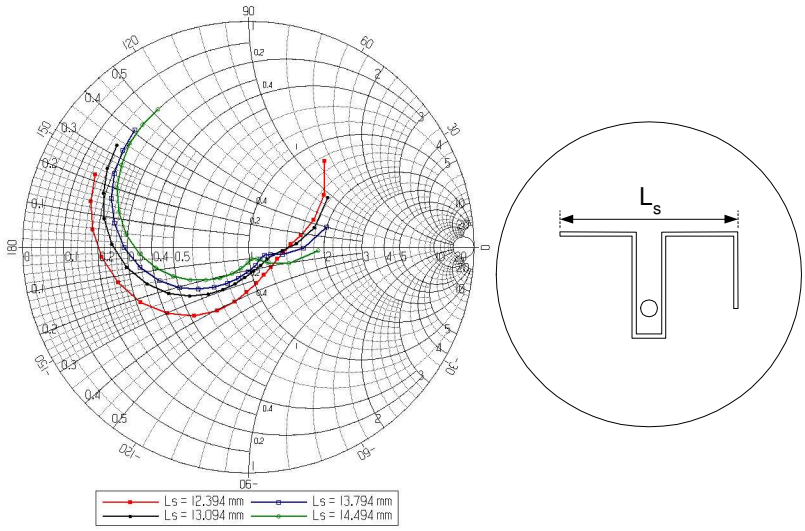

Figure 5.12: Variation of input impedance as a function of L_s. Frequency increases clockwise with step of 0.05GHz. Probe position = (5,0), L_1 = 5.735mm, d = 7.862mm

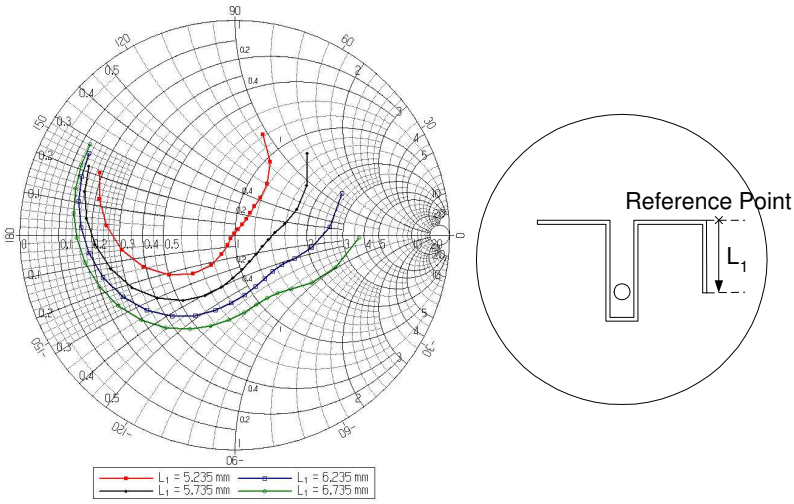

Figure 5.13: Variation of input impedance as a function of L_1. Frequency increases clockwise with step of 0.05GHz. Probe position = (5,0), L_s = 12.394mm, d = 7.862mm

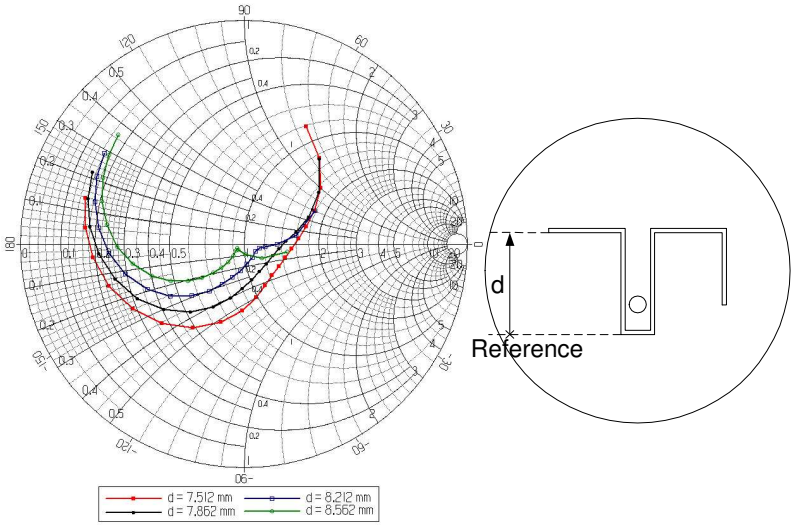

Figure 5.14: Variation of input impedance as a function of d. Frequency increases clockwise with step of 0.05GHz. Probe position = (5,0), L_s = 12.394mm, L_1 = 5.735mm

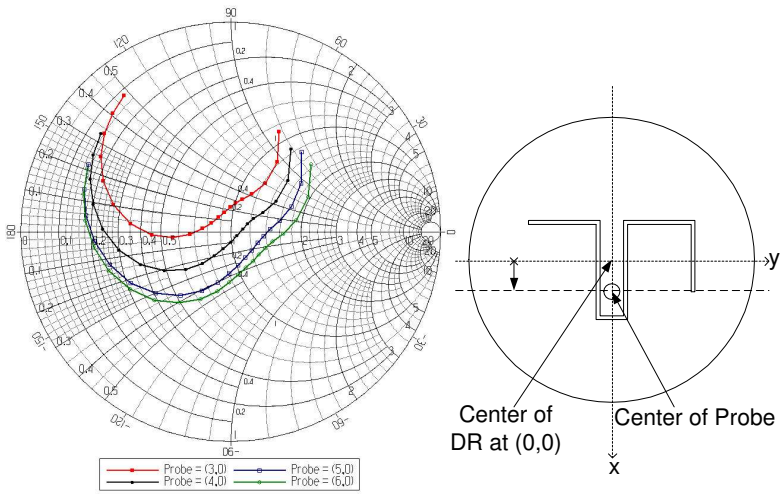

Figure 5.15: Variation of input impedance as a function of probe position. Frequency increases clockwise with step of 0.05GHz. L_s = 12.394mm, L_1 = 5.735mm, d = 7.862mm

However, using the above observations to design a CP antenna is not enough. After achieving a wide impedance bandwidth, the next task is to tune the design parameters until axial ratio of the antenna at boresight is around 1. The axial ratio can be obtained from:

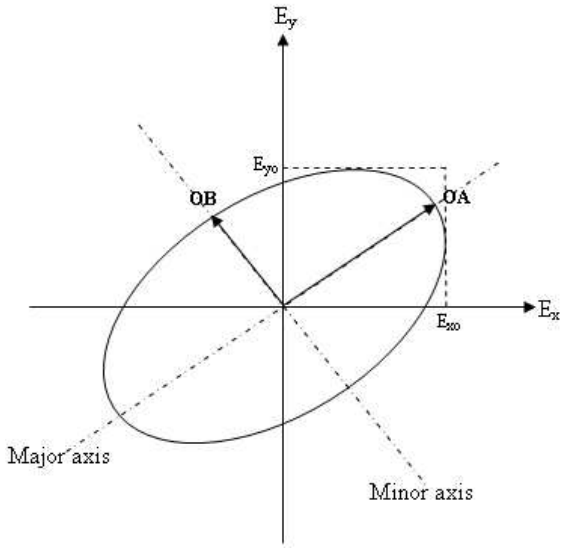

Figure 5.16: Axial ratio calculation

$$AR = \frac{major\ axis}{minor\ axis} = \frac{OA}{OB} \tag{5.5.1}$$

It is a very tedious task to tune the antenna until AR becomes unity. An easier and faster way to design subsequent LP and CP antennas is by scaling the design parameters from Figure 6.17 and 6.42, followed by fine-tuning the antenna using the above parametric studies.

Chapter 6

Results and Discussions

In this chapter, eigenvalues of cylindrical dielectric resonator with various permittivity values and sizes, are analyzed using Tangential Vector Finite Element (TVFE) method. The predicted eigenvalues are then compared with measured results, to ascertain the range of validity of the proposed method and some other popular models. Once the eigenvalues have been computed accurately, the antennas are designed and fabricated. Measured results of the dielectric resonator (DR) antennas are subsequently presented. Performance of antenna using different resonator geometries and permittivity values are compared to understand their characteristics and potential advantages. Lastly, the measured results of a circularly polarized cylindrical DR antenna is presented and used to compare with a linearly polarized DR antenna.

6.1 Comparison of Eigenvalues

6.1.1 Test Case: Empty Box

Before comparing the eigenvalues using various methods, it is necessary to ascertain the accuracy of finite element method. As a simple example, consider the problem of finding the eigenvalues of an empty cavity as shown in Figure 6.1, which shows an air-filled cavity and the mesh generated using *GiD 7.2* - a three-dimensional finite element mesh generator. The walls of the cavity are perfectly conducting, so the

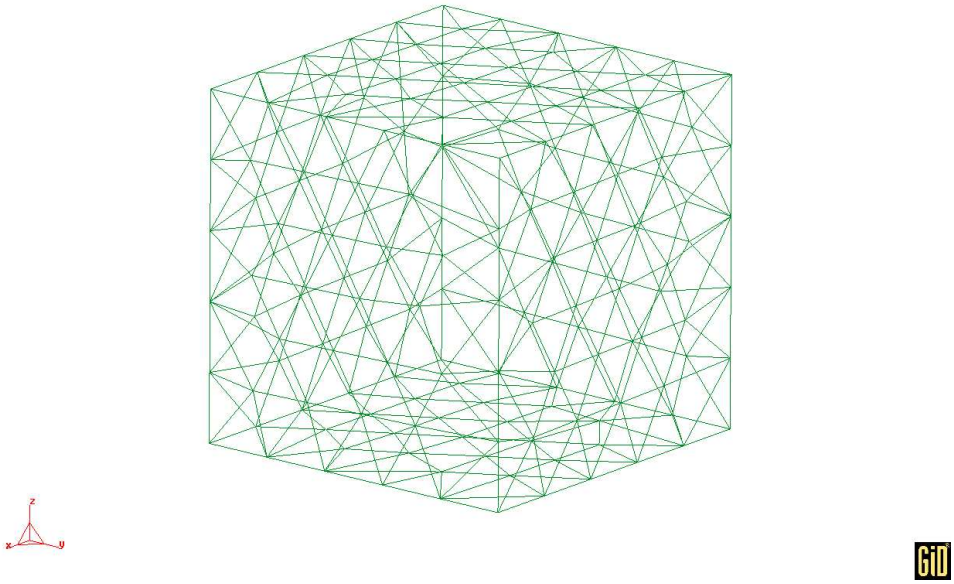

Figure 6.1: Mesh generated for empty cavity using *GiD 7.2*

governing equations for the electric field are as follows:

$$\nabla \times (\nabla \times E) - k_o^2 E = 0 \tag{6.1.1}$$

$$\hat{n} \times E = 0 \tag{6.1.2}$$

The analytical solution to this problem is very well established and it consists of two sets of modes: TE_{mnp} and TM_{mnp}. The eigenvalues can be calculated analytically as

$$k^2 = \pi^2 \left(\frac{m^2}{a^2} + \frac{n^2}{b^2} + \frac{p^2}{c^2} \right) \tag{6.1.3}$$

Hence, the case of an empty cavity is solved using the finite element method described earlier and compared with eigenvalues obtained analytically using Equation (6.1.3). The mesh generated for the cavity is refined until the eigenvalues computed are below 1% of error as compared with the analytical model. The computed results are summarized in Table 6.1. From the tabulated results, four cases A, B, C and D are used to compare with the analytical results.

Comparison of Eigenvalues									
		Case A		**Case B**		**Case C**		**Case D**	
Mode	**Analytical**	Computed (tetrahedral) 93 Unknowns	Error(%)	Computed (tetrahedral) 191 Unknowns	Error(%)	Computed (tetrahedral) 419 Unknowns	Error(%)	Computed (tetrahedral) 1422 Unknowns	Error(%)
TE_{101}	0.8322	0.8329	0.08	0.8262	0.72	0.8255	0.81	0.8299	0.28
TE_{011}	0.8322	0.8472	1.80	0.8306	0.19	0.8307	0.18	0.8309	0.16
TM_{110}	0.8322	0.8653	3.98	0.8472	1.80	0.8358	0.43	0.8320	0.02
TE_{111}	1.0192	1.0815	6.11	1.0060	1.30	1.0179	0.13	1.0204	0.12
TM_{111}	1.0192	1.1037	8.29	1.0249	0.56	1.0267	0.74	1.0209	0.17
TE_{102}	1.3158	1.2716	3.36	1.2435	5.49	1.2839	2.42	1.3028	0.99
TE_{201}	1.3158	1.3320	1.23	1.2721	3.32	1.3017	1.07	1.3042	0.88
TE_{021}	1.3158	1.3556	3.02	1.2994	1.25	1.3084	0.56	1.3065	0.71
TE_{012}	1.3158	1.3869	5.40	1.3124	0.26	1.3109	0.37	1.3071	0.66
TM_{210}	1.3158	1.4391	9.37	1.3256	0.74	1.3236	0.59	1.3112	0.35
TM_{120}	1.3158	1.4480	10.05	1.3652	3.75	1.3286	0.97	1.3157	0.01
TE_{112}	1.4413	1.4701	2.00	1.3871	3.76	1.4049	2.53	1.4273	0.97
TM_{112}	1.4413	1.5186	5.36	1.4045	2.55	1.4265	1.03	1.4321	0.64

Table 6.1: Eigenvalues (k_o, cm^{-1}) for an empty cavity with dimensions of 5.339 cm $\times$ 5.339 cm $\times$ 5.339 cm)

The difference between all the four cases lies in the mesh generated. As the mesh becomes denser, the number of unknowns increases. In Case A, there are 93 unknowns and this leads to an error percentage ranging from 0.08% to 10%. As the mesh is further refined in Case B (191 unknowns), the error percentage improved to within the range of 0.19% - 5.49%. Similar trend is observed in Case C (419 unknowns) as the error percentage improves to 0.13% - 2.53%. The solution finally converges to below 1% of error in Case D which has 1422 unknowns. Hence, consistency in obtaining accurate results within 1% of error can be achieved as the meshing becomes more refined.

6.1.2 Dielectric Resonator in Cavity

Using the concept mentioned in the earlier section, similar procedure is applied to the case of a dielectric resonator placed in the center of a cavity as shown in Figure 6.2. In the computation of the dielectric resonator's eigenvalues, volume mesh is generated. But for easy viewing, surface mesh is generated in Figure 6.3. A closed-up view of the mesh generated using 3-dimensional tetrahedral elements is shown in Figure 6.5. The meshing of the cavity is omitted in this case for simplicity.

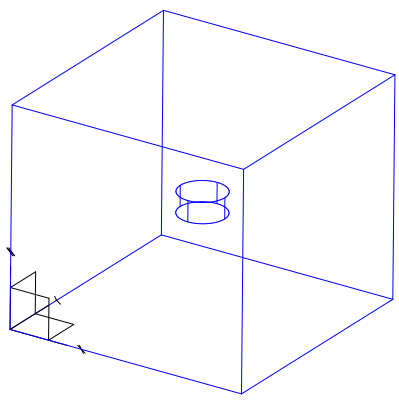

Figure 6.2: Geometry of a Dielectric Resonator positioned in the center of a metallic box drawn using *Gmsh*

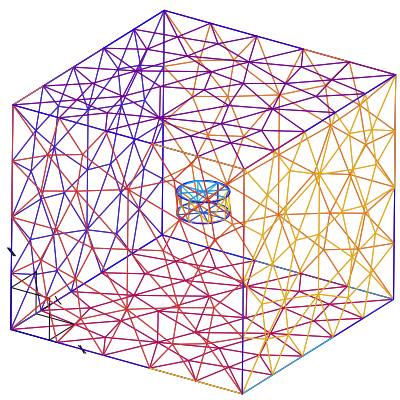

Figure 6.3: Surface Mesh generated for the metallic box enclosing a dielectric resonator

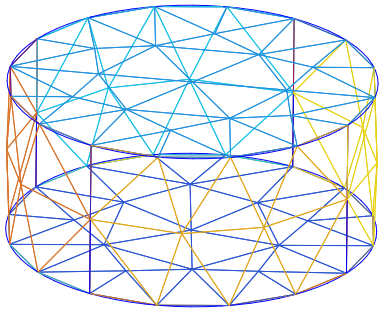

Figure 6.4: Closed-up view of surface mesh generated for the dielectric resonator

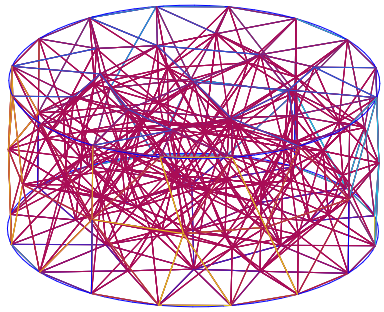

Figure 6.5: Closed-up view of volume mesh generated for the dielectric resonator

Using the mesh generated, eigenvalues of the cavity and dielectric resonator can be obtained. To obtain an accurate evaluation of the eigenvalues, there are a few considerations.

Effect of mesh refinement

The first consideration is to ensure computed solution has converged, by meshing the cavity with resonator progressively until subsequent eigenvalues give an absolute error less than 0.01 difference. A dielectric resonator of ϵ_r=79.7, radius = 5.145mm and height = 4.51mm, placed inside a 8×8×8cm cavity shall be used as an example. Six steps in meshing are generated in Table 6.2 to investigate the convergence of the resonator's eigenvalues.

Case	Nodes	Unknowns	Maximum edge length (tetrahedral)	
			Cavity,Δm(cm)	DR,Δd(cm)
(a)	193	1091	2.0	0.50
(b)	239	1422	1.8	0.50
(c)	312	1829	1.6	0.50
(d)	362	2178	1.6	0.30
(e)	450	2816	1.6	0.20
(f)	474	2970	1.6	0.18

Table 6.2: Parameters used to generate mesh of the dielectric resonator in cavity

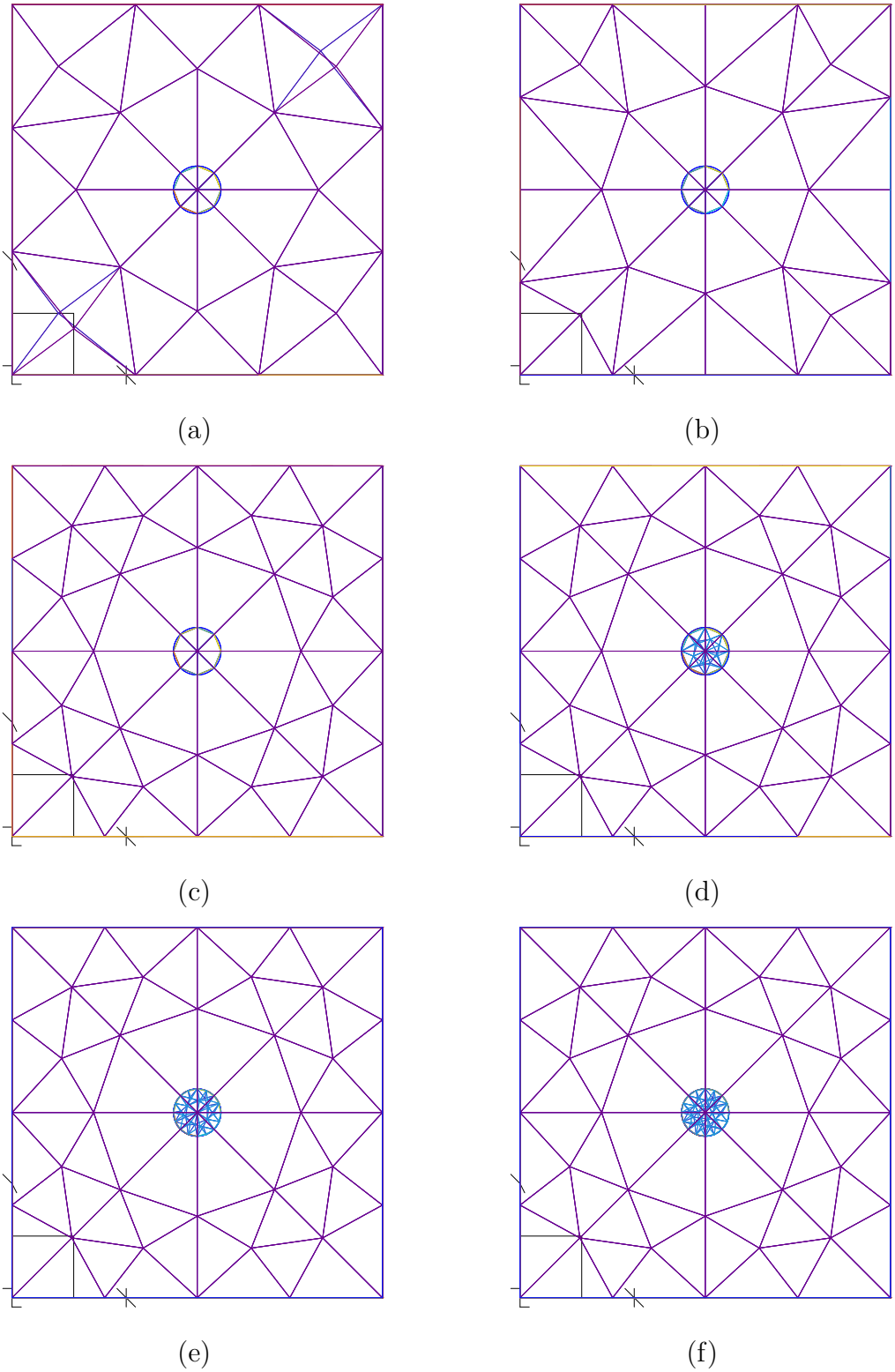

Figure 6.6: Steps in the mesh refinement process for dielectric resonator with permittivity of 79.7, radius a=0.5145cm and height h=0.451cm: (a)193 Nodes, $\Delta m = 2.0cm$ and $\Delta d = 0.5cm$ (b)239 Nodes, $\Delta m = 1.8cm$ and $\Delta d = 0.5cm$ (c)312 Nodes, $\Delta m = 1.6cm$ and $\Delta d = 0.5cm$ (d)362 Nodes, $\Delta m = 1.6cm$ and $\Delta d = 0.30cm$ (e)450 Nodes, $\Delta m = 1.6cm$ and $\Delta d = 0.20cm$(f)474 Nodes, $\Delta m = 1.6cm$ and $\Delta d = 0.18cm$

It can be observed from case (a)-(c) that maximum edge length for the tetrahedral elements within the dielectric resonator (Δd) has been kept constant. Region outside the resonator has been meshed according to steps of Δm=2.0cm,1.8cm,1.6cm. Next, in the case (c)-(f), the maximum edge length inside the resonator is refined accordingly to steps of Δ d=0.50cm, 0.30cm, 0.20cm and 0.18cm while Δm is set at 1.6cm. The results of the computed eigenvalues are tabulated in Table 6.3. As observed from

Modes	Case						Absolute Error $\|\delta t\|$				
	(a)	(b)	(c)	(d)	(e)	(f)	$(b)-(a)$	$(c)-(b)$	$(d)-(c)$	$(e)-(d)$	$(f)-(e)$
$TE_{01\delta}$	0.830	0.676	0.678	0.826	0.782	0.779	0.154	0.002	0.148	0.044	0.003
$HE_{11\delta}$	0.956	0.944	0.954	0.954	0.960	0.953	0.012	0.010	0.000	0.006	0.007
$TM_{01\delta}$	1.127	1.104	1.131	1.135	1.142	1.138	0.023	0.027	0.004	0.007	0.004

Table 6.3: Eigenvalues computed in the mesh refinement process

Table 6.3, the absolute errors $|\delta t|$ generally decrease for all the three modes. In case (f), $|\delta t|$ falls below 0.01 and hence the iteration is stopped.

Effect of the cavity's size

The second consideration is the effect of the cavity size on the resonator's resonant frequency. Consider the same example as before, a 8cm×8cm×8cm cavity and a dielectric resonator with $\epsilon_r = 79.7$, radius = 5.145mm and height = 4.51mm. Such a case generates the same results shown in Table 6.3. Even though the results seem to have converged, computed eigenvalues in case (f) have absolute error percentage of 0.44 - 6.86% from measured results (Table 6.6). A glance of Table 6.6 reveals that $TE_{01\delta}$ mode has the lowest frequency and hence, the largest free-space wavelength. The cavity box must be sufficiently large so as not to perturb the resonator's eigenmodes. Therefore, cavity of different sizes are employed to examine their effects on eigenvalues of 3 main modes ($TE_{01\delta}$, $HE_{11\delta}$ and $TM_{01\delta}$).

Size of Cavity		$TE_{01\delta}$ **(0.729)**		$HE_{11\delta}$ **(0.954)**		$TM_{01\delta}$ **(1.133)**	
(cm)	(λ_o) wrt $TE_{01\delta}$	k_o	|Error(%)|	k_o	|Error(%)|	k_o	|Error(%)|
7×7×7	0.81	0.769	5.54	0.947	0.78	1.091	3.74
8×8×8	0.93	0.779	6.86	0.953	0.10	1.138	0.44
9×9×9	1.04	0.743	1.88	0.956	0.19	1.119	1.20
10×10×10	1.16	0.745	2.22	0.951	0.37	1.111	1.92
11×11×11	1.28	0.738	1.29	0.955	0.07	1.120	1.16
12×12×12	1.39	0.730	0.14	0.955	0.10	1.126	0.62

Table 6.4: Effects of cavity's size on eigenvalues of the dielectric resonator ($\epsilon_r = 79.7, a = 5.145mm, h = 4.51mm$)

As observed from Table 6.4, cavity's size has an impact on the computed eigenvalues. This influence is greater for modes with lower resonant frequency, such as $TE_{01\delta}$ mode which has the lowest eigenvalue value ($f_r = 3.48$GHz and $\lambda_o = 8.62mm$). The absolute error percentage in predicting the resonator's eigenvalues range from 0.10 - 6.86% when using a cavity of 7×7×7cm and 8×8×8cm. As the cavity's dimensions increase to 9×9×9cm, a much improved absolute error percentage of 0.19 - 1.88% has been achieved. The absolute error percentage eventually improved to below 1% for all the three modes when the cavity increased to 12×12×12cm.

However, it is observed that accurate prediction of the desired $HE_{11\delta}$ mode does not require a cavity size of such magnitude. In fact, a 7×7×7cm is sufficiently large enough to predict the eigenvalues within 1% error percentage. Taking these two factors into consideration, eigenvalues are computed and discussed in the next section.

6.2 Validity of models

Results of the computed eigenvalues are tabulated in Table 6.6 for isolated cylindrical DRs. A wide range of permittivity values ranging from 35 - 79.7 and of different sizes are chosen to carry out this investigation. Eigenvalues generated using Tangential

Vector Finite Element (TVFE) method are compared with measured ([20],[21],[22]) and computed eigenvalues using conventional models ([2],[4]). From Table 6.6, it is observed that by imposing PMC walls, percentage error greater than 20% is obtained. Eigenvalues computed uisng PMC wall model are usually lower than the measured values. On the other hand, Mongia's closed-form equations is capable of predicting the eigenvalues with errors below 2%. Finally, TVFE method has been able to predict eigenvalues with less than 1% error for all the cases.

Next, eigenvalues of rectangular DR antennas are investigated. The mode excited is TE^z_{111} by means of aperture coupling. The resonant frequencies are then compared among values obtained from DWM, simulation (HFSS), TVFE method and measurement. It is noted that simulation and measurement results have taken into account, effects of the feeding mechanism while DWM and TVFE method are basically computing eigenvalues of an isolated rectangular DR. It is interesting to see how much the antenna has de-tuned due to the feeding mechanism. Eigenvalues computed using DWM are generally lower than measured results. Simulated values are usually closer to the measured values. In case (a), the simulated frequency is way off the measured value. As the antenna's size gets smaller, it is very sensitive to its environment such as its feed. Hence, the antenna's resonant frequency is de-tuned the most as compared to other cases. The TVFE method achieves quite a good accuracy for predicting the eigenvalues of the antenna.

				Resonant Frequency (GHz) for Rectangular DRA						
Case	a (mm)	b (mm)	d (mm)	DWM	|Error %|	TVFE	|Error %|	HFSS	|Error %|	Measured [23]
(a)	10	5	10	2.50	8.4	2.57	5.9	2.354	13.8	2.73
(b)	15	5	15	2.06	3.3	2.17	1.9	1.918	10.0	2.13
(c)	20	5	20	1.87	20.3	1.70	9.3	1.690	8.7	1.56

Table 6.5: Comparison of resonant frequency among DWM, simulation, TVFE method and measurement (ϵ_r=90)

Computed Eigenvalues of an Isolated Cylindrical Dielectric Resonator											
	Resonator								**This Study**		
	Parameters			**(Reference)**	**(PMC Wall [4])**		**(Mongia [2])**		**(TVFE)**		
Mode	ϵ_r	a (cm)	H (cm)	k_o	k_o	Error(%)	k_o	Error(%)	k_o	Error(%)	Reference
$TE_{01\delta}$	79.7	0.5145	0.451	0.729	0.653	10.38	0.725	0.53	0.730	-0.14	[20]
$HE_{11\delta}$	79.7	0.5145	0.451	0.954	0.560	41.36	0.962	-0.82	0.955	-0.10	[20]
$TM_{01\delta}$	79.7	0.5145	0.451	1.133	0.921	18.71	1.129	0.34	1.126	0.62	[20]
$TE_{01\delta}$	35	0.5000	1.000	0.934	0.855	8.43	0.934	0	0.931	0.28	[21]
$HE_{11\delta}$	35	0.5000	1.000	0.934	0.677	27.54	0.946	-1.29	0.935	-0.13	[21]
$TM_{01\delta}$	35	0.5000	1.000	1.338	1.322	1.17	1.360	-1.64	1.337	0.10	[21]
$TE_{01\delta}$	38	0.6415	0.562	0.831	0.759	8.69	0.836	-0.56	0.832	0.17	[22]
$HE_{11\delta}$	38	0.6415	0.562	1.085	0.650	40.09	1.105	-1.58	1.082	-0.31	[22]
$TM_{01\delta}$	38	0.6415	0.562	1.289	1.070	17.01	1.292	-0.24	1.288	-0.05	[22]

Table 6.6: Comparison of eigenvalues obtained using Tangential Vector Finite Element (TVFE) Method and other conventional methods

6.3 Dielectric Resonator Antennas Fabricated

In this section, dielectric resonator antennas are fabricated after optimization process using Ansoft High Frequency Structure Simulator (HFSS) and eigenvalue analysis (TVFE method). Return loss of the antenna is measured using HP Vector Network Analyzer (VNA), while radiation pattern measurement is carried out using Indoor Anechoic Chamber. Firstly, comparison of two antenna geometries (cylindrical and rectangular DR) are investigated to ascertain their potential advantages. Next, comparison is done between antennas of low ($\epsilon_r = 10.2$) and high ($\epsilon_r = 38.5$) permittivity values. Finally, a circular-polarized antenna is designed and fabricated. The measurement results are included for comparison with the linear-polarized case.

6.3.1 Comparison of Cylindrical and Rectangular Dielectric Resonator Antennas

Schematics

The schematics for the cylindrical and rectangular DRAs designed are shown in Figure 6.7 and 6.8 respectively. Parameters shown in the schematics are optimized parameters based on commercial software *Ansoft HFSS 8.5*. A summary of the physical dimensions of the resonator and feeding substrate chosen are presented in Table 6.7.

Specifications		
Antenna Geometry	Rectangular	Cylindrical
Predicted Frequency (GHz)	3.79	4.10
Resonator Permittivity, ϵ_r	10.2	10.2
Dimensions(mm)	23.6(W) $\times$ 23.6(L)	24(D)
Height(mm)	7.62	7.62
Substrate Permittivity, ϵ_s	2.2	2.2
Substrate thickness, t (mils)	62	62

Table 6.7: Specifications of resonator and substrate used

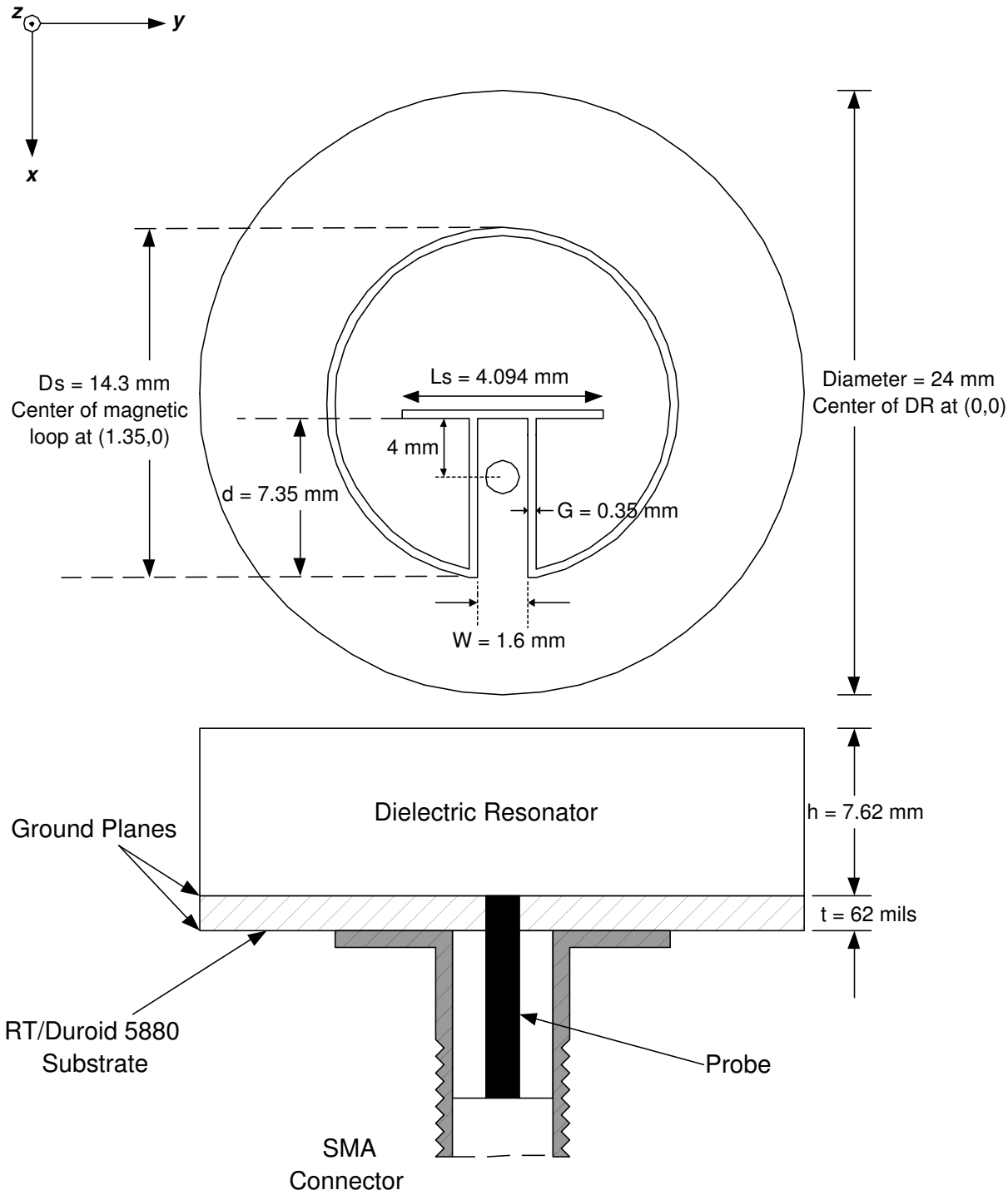

Figure 6.7: Design schematics for linear-polarized cylindrical DRA

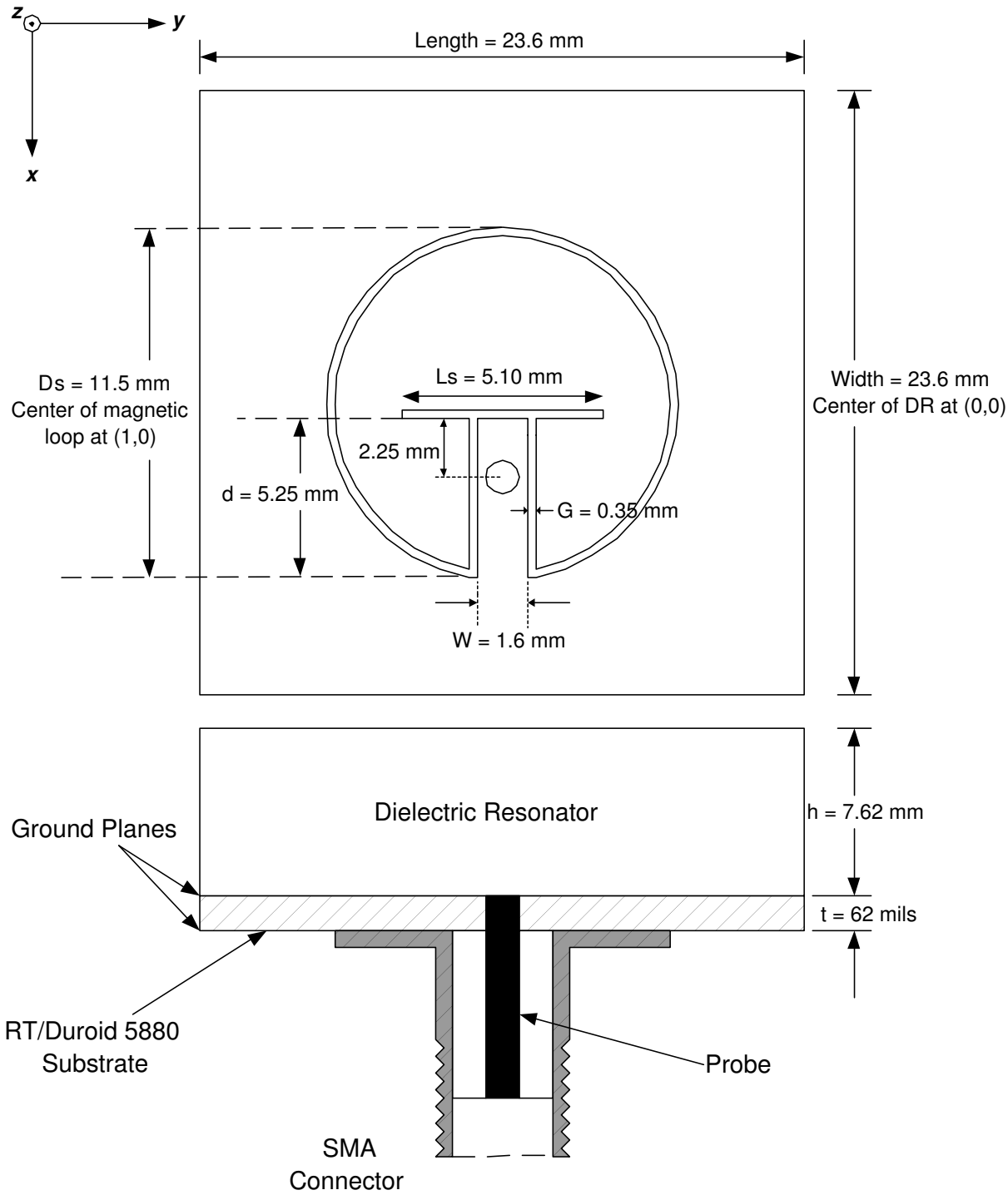

Figure 6.8: Design schematics for linear-polarized rectangular DRA

Near-Field analysis

Before comparing performance of the cylindrical and rectangular DR antennas, it is crucial to have some understanding of the physics behind the designed antennas. Hence, near-field analysis of the DR antennas is investigated using simulation software. Comparison of the antennas' E-fields, H-fields and current density are carried out. The geometry of the antenna simulated are as shown in Figure 6.9 and 6.10. E-fields and H-fields of both antennas resembles that of $HEM_{11\delta}$ mode in a dielectric waveguide or the $TM_{11\delta}$ mode (if PMC walls are assumed) shown in Figure 3.6. This is an indication that the desired $HEM_{11\delta}$ has been excited.

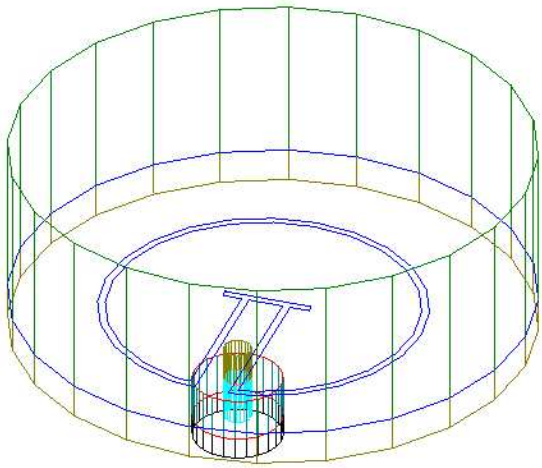

Figure 6.9: Cylindrical DRA simulated in HFSS

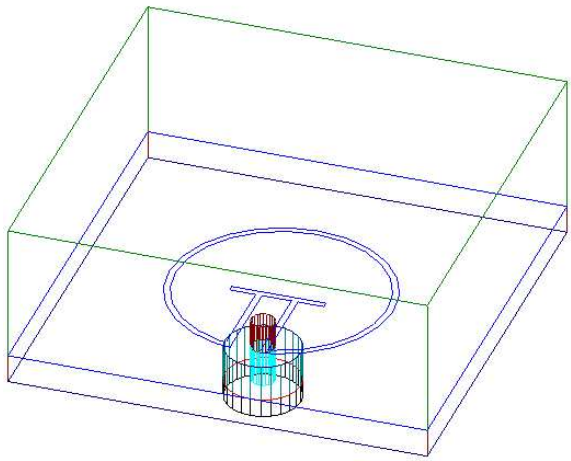

Figure 6.10: Rectangular DRA simulated in HFSS

From Figures 6.11 and 6.12, it is observed that E-fields can be excited from the magnetic loop, magnetic dipole and the coplanar waveguide feed. For cylindrical DR antenna, the magnetic loop contributes most of the E-fields, with the maximum component directed in the vertical direction (x-axis). The magnetic dipole can also contribute to E-fields in the vertical direction, but observed to be in lesser extent. Coplanar waveguide has been observed to excite E-fields in the horizontal direction (y-axis). These E-fields comprise of two components with equal magnitude but pointing in the opposite directions. Hence, far-field radiation at boresight is mainly due

to E-fields excited by the magnetic loop and dipole. The E-fields at the coplanar waveguide feed could result in a higher cross-polarization levels during the far-field measurement of the antenna.

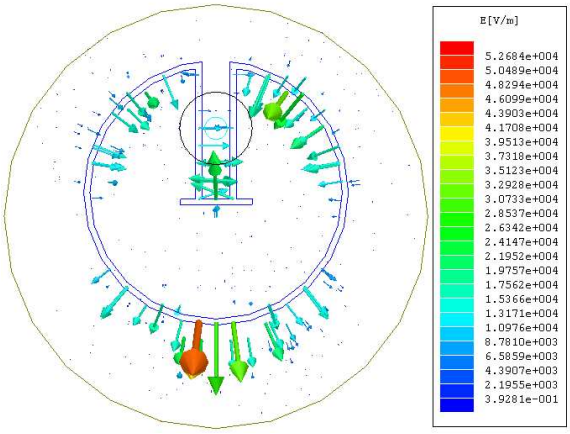

Figure 6.11: E-fields within the cylindrical dielectric resonator simulated using Ansoft HFSS (4.20GHz)

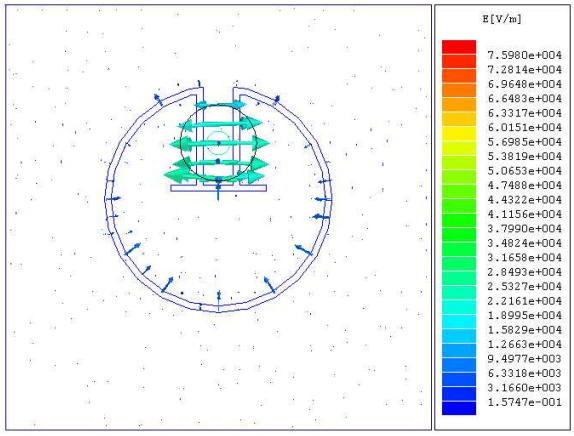

Figure 6.12: E-fields within the rectangular dielectric resonator simulated using Ansoft HFSS (3.64GHz)

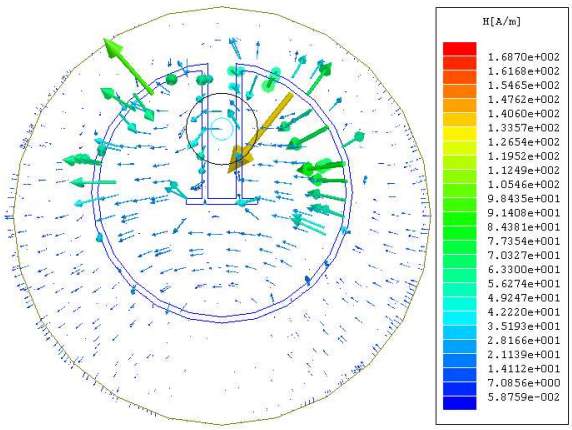

Figure 6.13: H-fields within the cylindrical dielectric resonator simulated using Ansoft HFSS (4.20GHz)

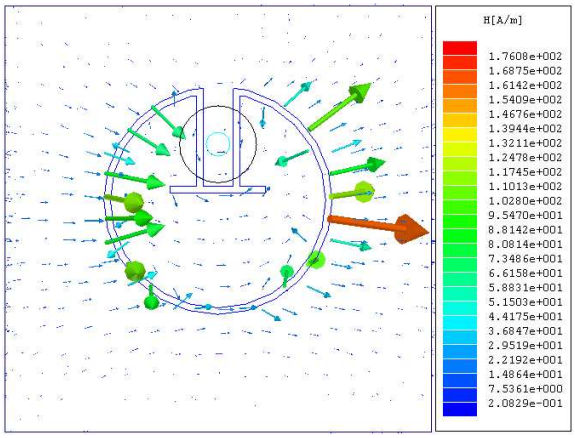

Figure 6.14: H-fields within the rectangular dielectric resonator simulated using Ansoft HFSS (3.64GHz)

Next, the current densities for both DRAs are investigated. The current density for rectangular DR antennas in Figure 6.16 is of particular interest, as maximum current density is noticed at both sides of the magnetic loop, with line of symmetry along the x-axis. This suggests the length of the magnetic loop is about $1\lambda_g$ and can help to approximated the effective dielectric constant ϵ_{eff}. The first step is to

calculate the circumference of the magnetic loop. From schematics of the rectangular DR antenna (Figure 6.8), the outer diameter of the magnetic loop, D_s is 11.5mm and the inner diameter is 10.8mm. The actual diameter of the magnetic loop is taken from the center of slot of the magnetic loop, that is (11.5-0.35)=11.15mm. Hence the circumference of the magnetic loop L_{loop} is 35.04mm. At 3.64GHz, the free-space wavelength λ_o is 82.42mm and by equating $\lambda_g = \frac{\lambda_o}{\sqrt{\epsilon_{eff}}}$, the effective dielectric constant ϵ_{eff} is found to be 5.53.

Using this ϵ_{eff} value, the designs can be expressed in term of its electrical length in Figure 6.17 and 6.18. A convenient starting point of the design process is to tune the circumference of the magnetic loop to $1\lambda_g$ by similar observation of the current density. Subsequently, ϵ_{eff} can be approximated and used for calculation of λ_g. A good guess of the initial design parameters for subsequent designs, can be be obtained from scaling of Figure 6.17 and 6.18. Judging from the current density of the magnetic loop for cylindrical DRAs, the magnetic loop is larger than $1\lambda_g$. A quick calculation shows that the magnetic loop's circumference is 43.83mm, equivalent to $1.44\lambda_g$. Hence, after analyzing the antenna's near-field characteristics, the measurement of the antenna is presented in the next section.

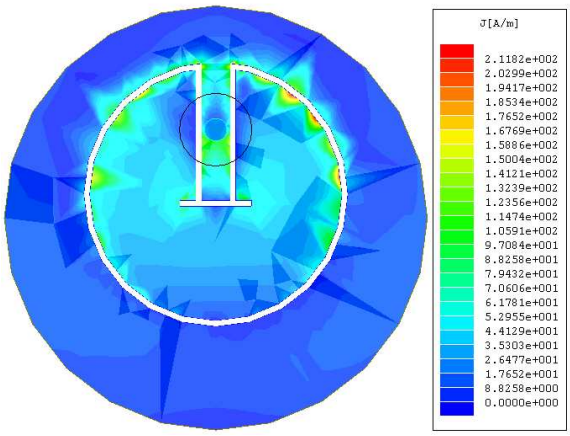

Figure 6.15: Simulated current density for cylindrical DR antenna using Ansoft HFSS (4.20GHz)

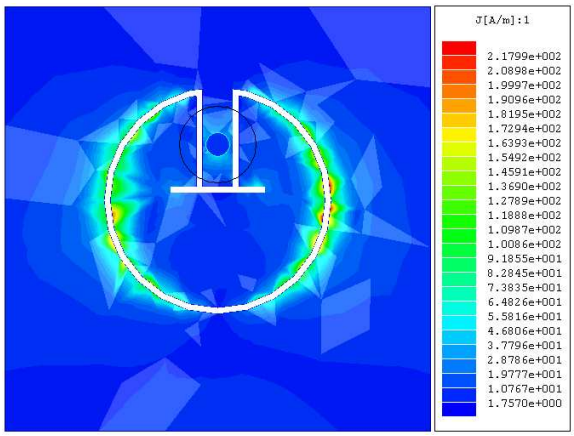

Figure 6.16: Simulated current density for rectangular DR antenna using Ansoft HFSS (3.64GHz)

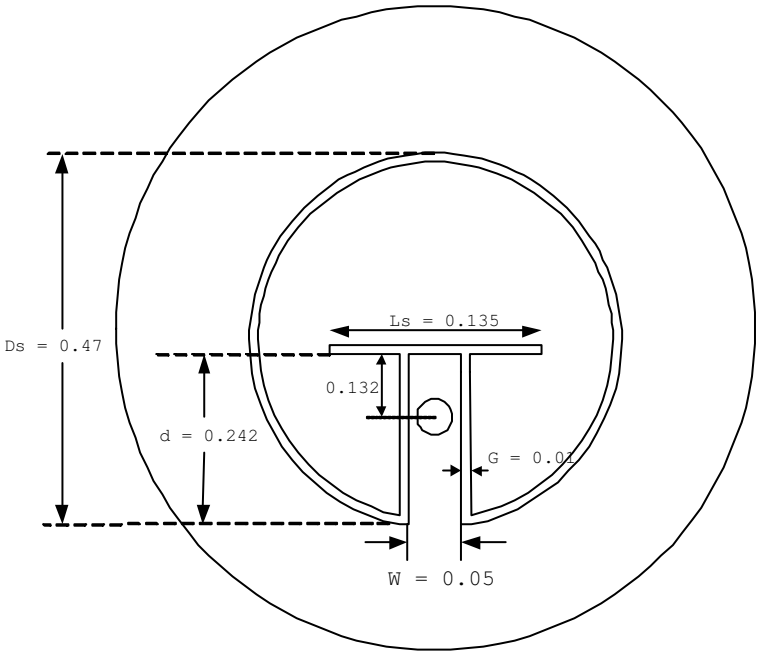

Figure 6.17: Electrical length (in λ_g) of the feed design for linear-polarized cylindrical DR antenna (4.20GHz)

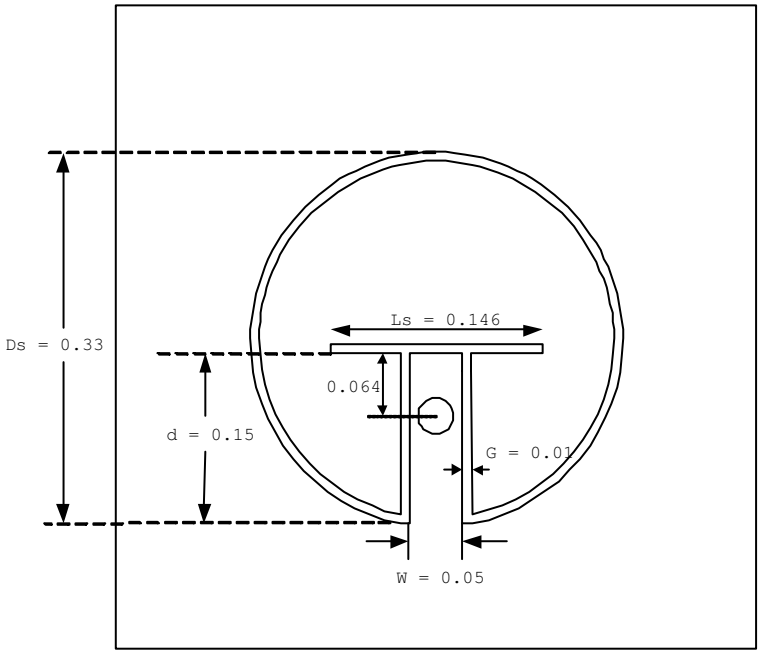

Figure 6.18: Electrical length (in λ_g) of the feed design for linear-polarized rectangular DR antenna (3.64GHz)

Measurement Results

Based on the design parameters mentioned in the previous section, the antennas are fabricated, measured and presented in this section. Photos of the fabricated antennas are displayed in Figure 6.19 to 6.23.

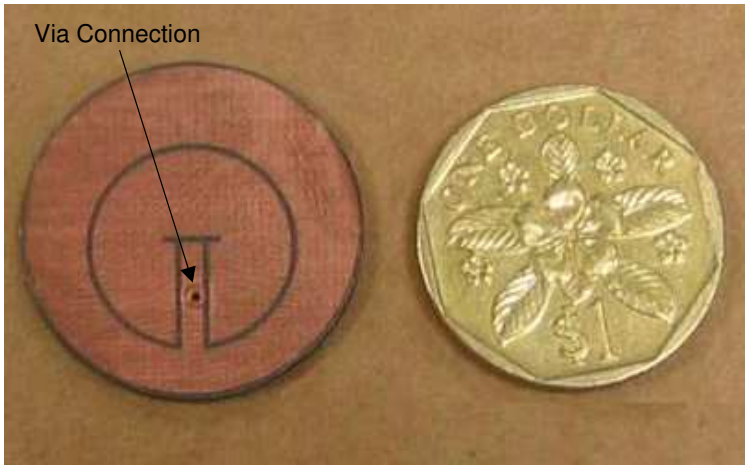

Figure 6.19: Top view of feeding substrate for Cylindrical Dielectric Resonator Antenna (Linear-Polarized) fabricated

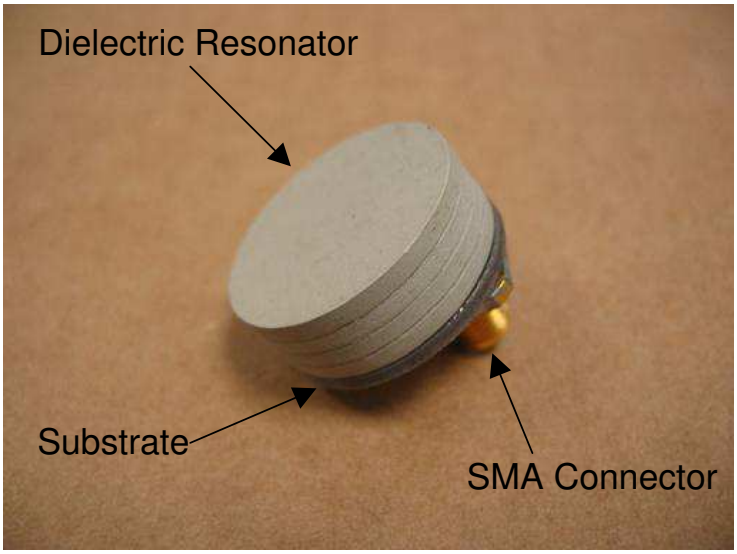

Figure 6.20: Three-dimensional view of Cylindrical Dielectric Resonator Antenna (Linear-Polarized) fabricated

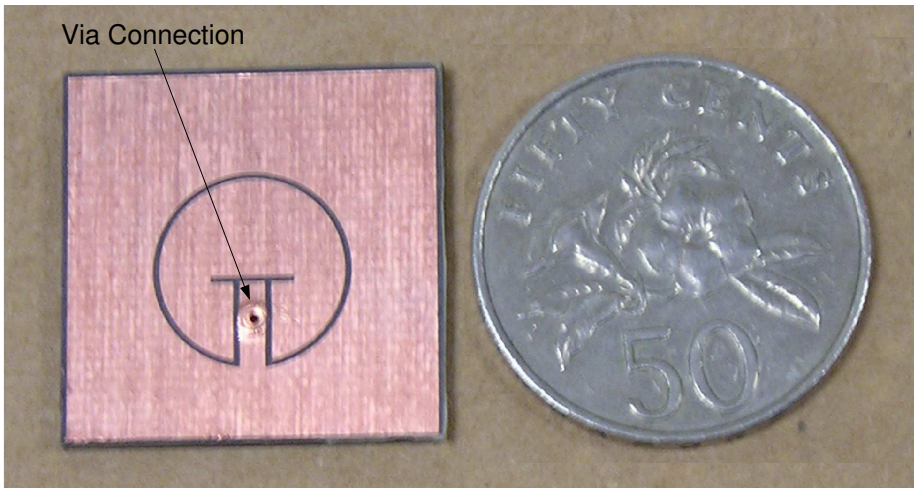

Figure 6.21: Top view of feed substrate for Rectangular Dielectric Resonator Antenna (Linear-Polarized) fabricated

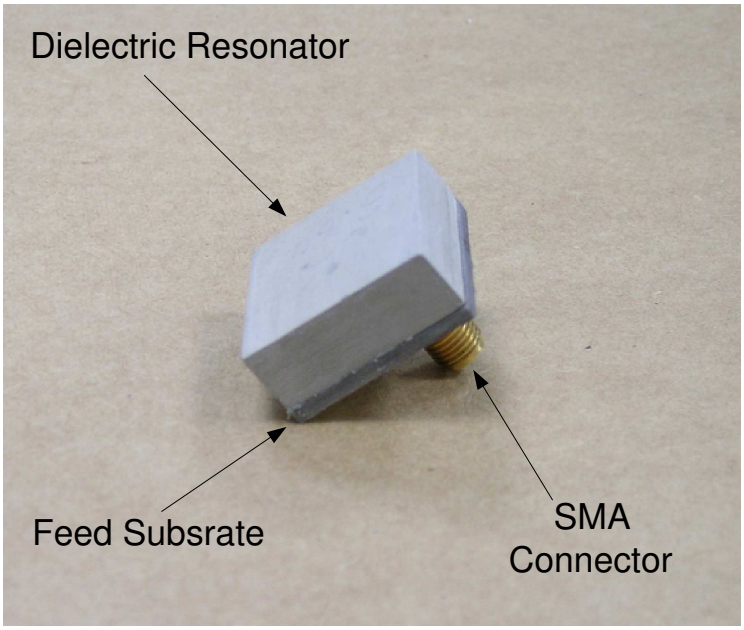

Figure 6.22: Three-dimensional view of Rectangular Dielectric Resonator Antenna (Linear-Polarized) fabricated

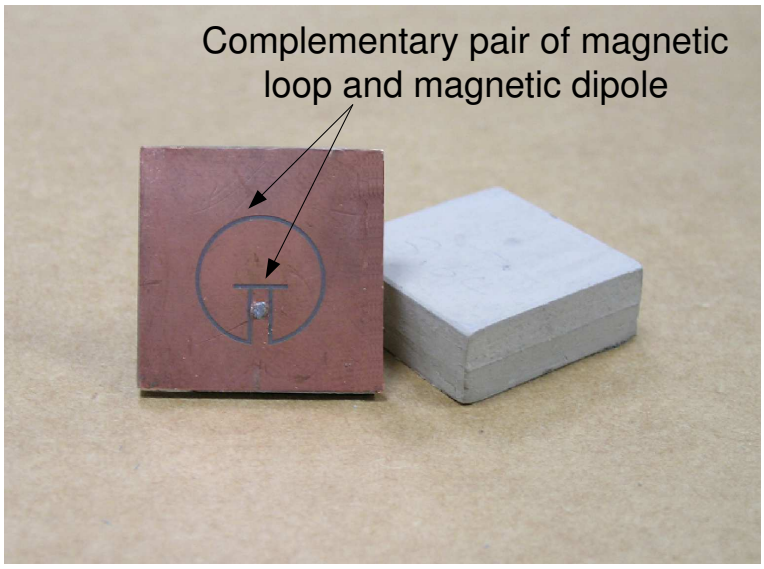

Figure 6.23: Photo showing the complementary pair of magnetic loop and magnetic dipole for linear-polarized antenna

For cylindrical DR antenna, the simulated bandwidth range from 3.80 GHz to 4.45 GHz. This corresponds to an impedance bandwidth of 16%. In contrast, the fabricated antenna has an impedance bandwidth of 13% and falls within the range of 3.90 to 4.45 GHz. The slightly smaller bandwidth is most likely due to the imperfect contact between the probe and the coplanar waveguide. The use of a via connection has been found to be the best way to avert a mismatch due to poor soldering. It can also ensure the air-gap between the feeding substrate and dielectric resonator is minimized. On the other hand, the rectangular dielectric resonator antenna exhibits a much wider simulated bandwidth of 27%, operating in the range of 3.30 GHz to 4.33 GHz (return loss $\geq$ 10dB). The fabricated antenna is in good agreement with the simulation results and exhibits a wide impedance bandwidth of 23%, ranging from 3.36 GHz to 4.25 GHz. A comparison of the return loss for cylindrical and rectangular DR antennas can be done by referring to Figure 6.24 and 6.25.

Near-Field Measurement		
Antenna Geometry	Rectangular	Cylindrical
Operating Frequency($\|S_{11}\| \geq 10dB$)	3.36 - 4.25 GHz	3.90 - 4.45 GHz
Impedance Bandwidth	0.89 GHz (23%)	0.55 GHz (13%)
Q-Factor	3.1	5.4

Table 6.8: Summary of near-field results for cylindrical and rectangular dielectric resonator antennas

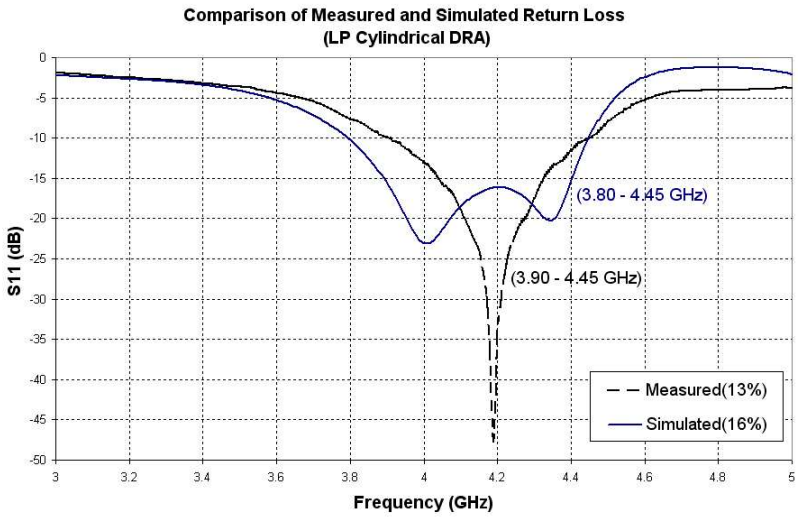

Figure 6.24: Measured Return Loss for Cylindrical Dielectric Resonator Antenna, $\epsilon_r = 10.2$ (Linear-Polarized)

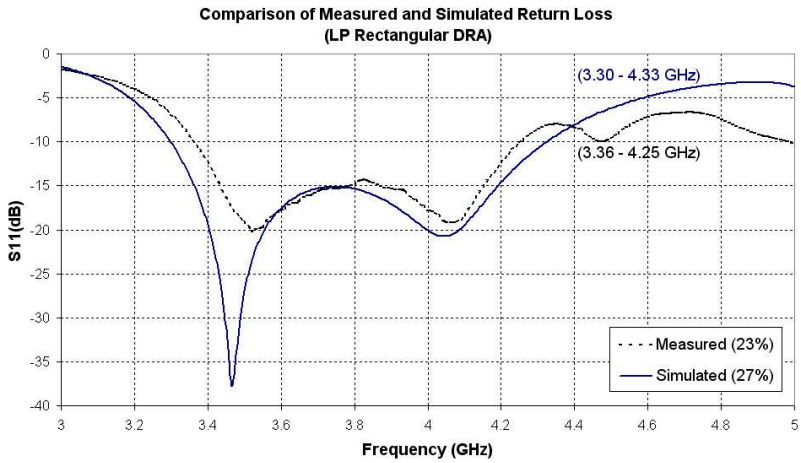

Figure 6.25: Measured Return Loss for Rectangular Dielectric Resonator Antenna, $\epsilon_r = 10.2$ (Linear-Polarized)

Subsequently, the far-field measurement of both antennas is carried out using NUS indoor anechoic chamber. The accuracy of such a measurement setup is believed to be about ±1dB. Both antennas exhibit symmetrical radiation patterns with minimal scalloping that is dominant for small antenna measurement. This is due to careful placement of the absorbers during measurements. The cylindrical DR antenna has a measured gain of about 4.20dB and this is in good agreement with the simulated gain of 4.40dB. In contrast, the rectangular dielectric resonator antenna has a measured gain of 3.97dB, as compared to a higher simulated gain of 4.47dB. The cross-polarization level for the rectangular DRA is observed to be much higher than that of the cylindrical DRA. The H-Plane 3dB-beamwidth Θ_H is also observed to be narrower than that of the cylindrical one. Hence, the rectangular DRA has a higher directivity and a lower radiation efficiency of 87%. This is lower than the cylindrical DRA, which has a radiation efficiency of 94%. The lower radiation efficiency for rectangular DRA could be due to the presence of higher order modes in the rectangular dielectric resonator, losses incur due to the feed and substrate loss. Even though the rectangular DRA can achieve a much wider impedance bandwidth than a cylindrical design, it must tolerate a lower radiation efficiency and a higher cross-polarization level.

Far-Field Measurement		
Antenna Geometry	Rectangular	Cylindrical
E-Plane Co-Polarization(dBi),E_{cPol}	3.35	4.20
E-Plane Cross-Polarization(dB) wrt E_{cPol}	-8.52	-21.2
E-Plane 3dB-Beamwidth(deg),Θ_E	119	115
H-Plane Co-Polarization(dBi),H_{cPol}	3.97	4.24
H-Plane Cross-Polarization(dB) wrt H_{cPol}	-16.04	-17.24
H-Plane 3dB-Beamwidth(deg),Θ_H	90	105
Forward-to-Backward(F/B) Ratio(dB)	8	13
Directivity(dB)	4.46	4.23
Radiation Efficiency(%)	87	94

Table 6.9: Summary of measured radiation patterns

The directivity is obtained by integrating the antennas' radiation patterns. Radiation efficiency of the antennas is computed using Wheeler cap method.

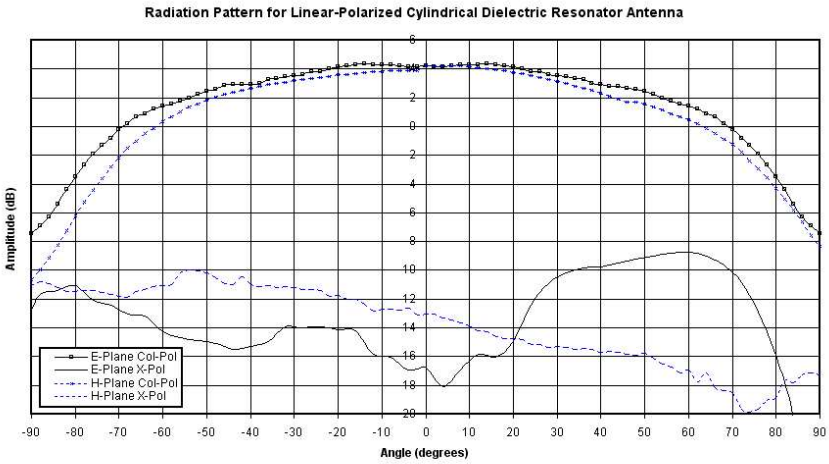

Figure 6.26: Measured far-field radiation pattern at 4.20 GHz for Cylindrical Dielectric Resonator Antenna (Linear-Polarized)

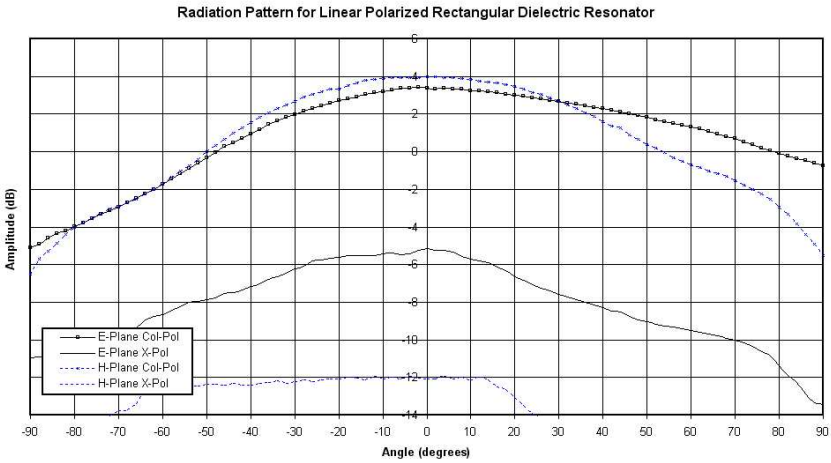

Figure 6.27: Measured far-field radiation pattern at 3.64 GHz for Rectangular Dielectric Resonator Antenna (Linear-Polarized)

6.3.2 Comparison of Antennas using High and Low Permittivity Dielectric Resonator

Next, DR antennas using dielectric resonators of high ($\epsilon_r = 38.5$) and low ($\epsilon_r = 10.2$) permittivity value are investigated. The advantage of using resonator with higher dielectric constant is a smaller physical size, since the resonator's dimension is a function of $\lambda_o/\sqrt{\epsilon_r}$. However, problems associated with a smaller antenna is its narrower bandwidth and lower radiation efficiency. In addition, it has greater sensitivity to fabrication errors and its environment. Design schematics for DR antenna using high permittivity value is shown in Figure 6.28. The earlier cylindrical DR antenna designed (with $\epsilon_r = 10.2$) is compared with the current case. A summary of the resonator and feeding substrate's specifications are presented in Table 6.10.

Specifications		
Resonator Permittivity, ϵ_r	38.5	10.2
Predicted Frequency (GHz)	4.04	4.10
Diameter(mm)	13	24
Height(mm)	5.00	7.62
Substrate Permittivity, ϵ_s	4.4	2.2
Substrate thickness, t (mils)	62	62

Table 6.10: Specifications of resonator and substrate used

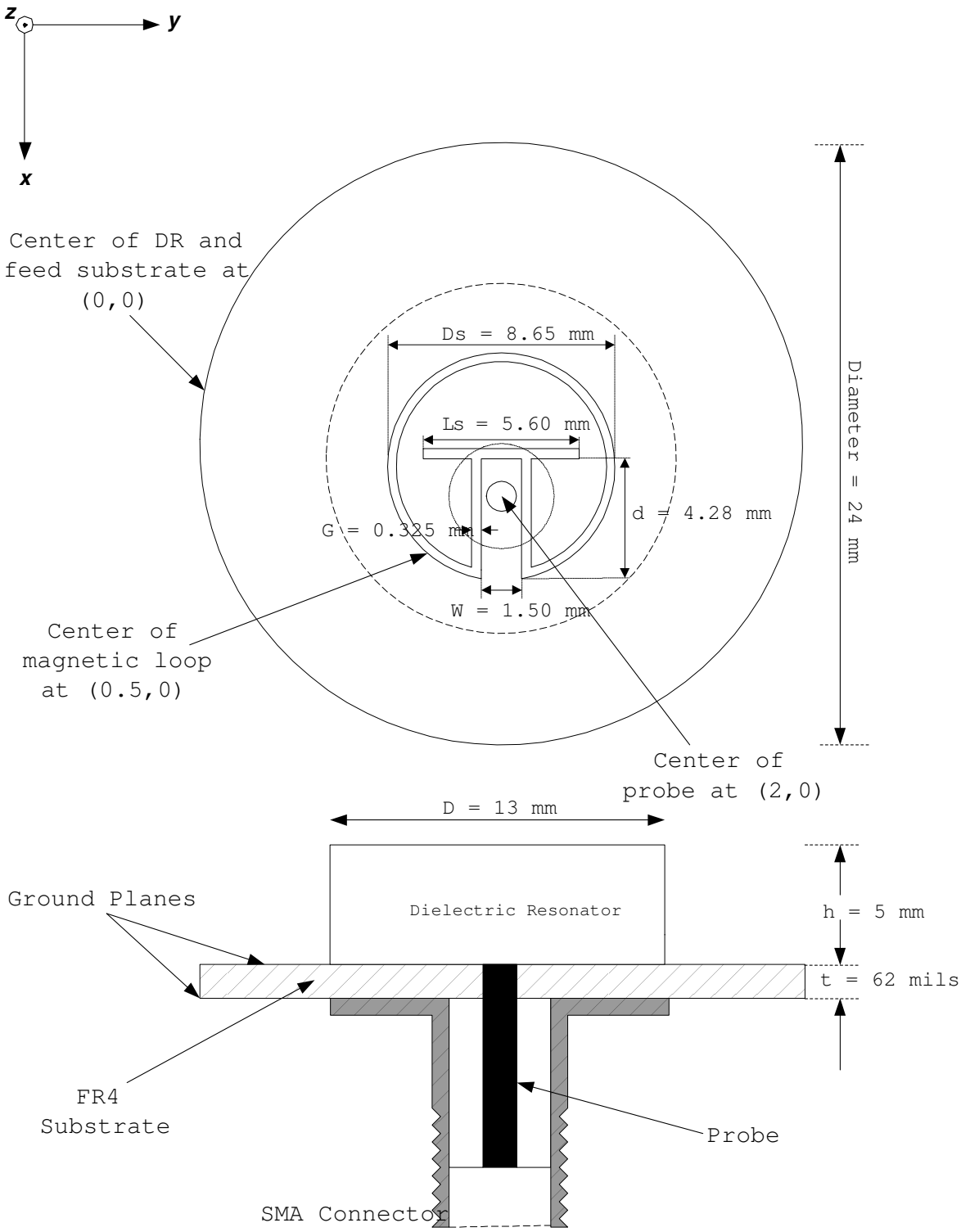

Figure 6.28: Design schematics for linear-polarized cylindrical DRA using high permittivity resonator ($\epsilon_r = 38.5$)

Near-Field Analysis

Near-field analysis of the antenna is next investigated. Analysis of the antenna's E-fields, H-fields and current density are conducted. The antenna structure simulated is presented in Figure 6.29. E-fields and H-fields of the antenna resemble that of $HEM_{11\delta}$ and hence, the desired mode has been excited.

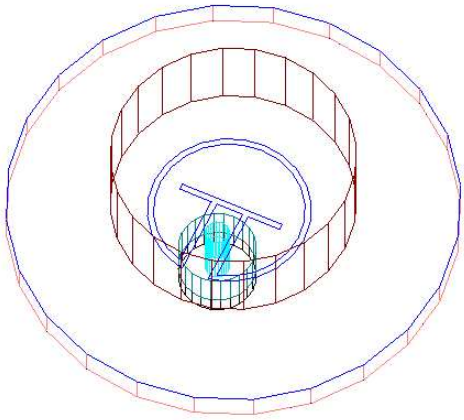

Figure 6.29: Linear-polarized antenna ($\epsilon_r = 38.5$) simulated using Ansoft HFSS

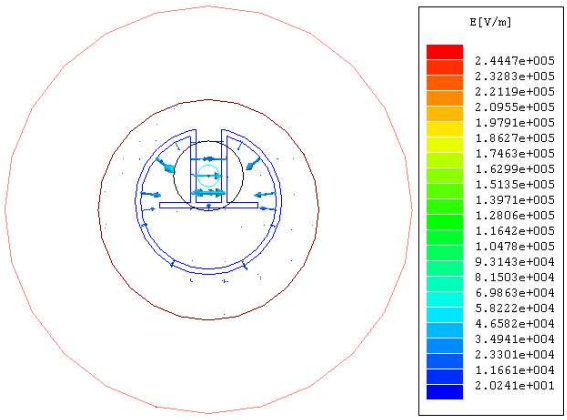

Figure 6.30: Simulated E-fields within the antenna ($\epsilon_r = 38.5$) using Ansoft HFSS (3.60GHz)

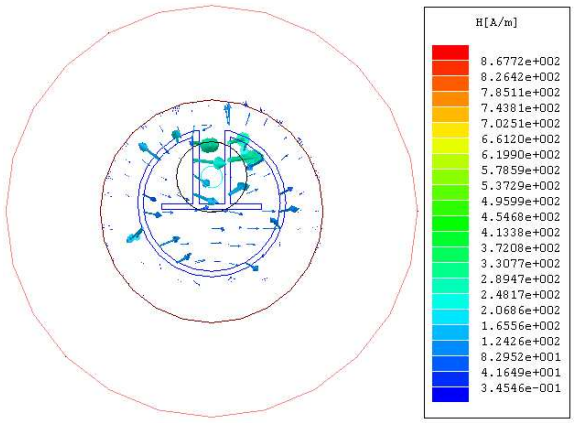

Figure 6.31: Simulated H-fields within the antenna ($\epsilon_r = 38.5$) simulated using Ansoft HFSS (3.60GHz)

From Figure 6.30, E-fields are observed to come from the magnetic loop, magnetic dipole and the coplanar waveguide feed. Like in the previous case, the magnetic

loop contributes to most of the E-fields. The magnetic dipole has also excited E-fields along the vertical direction, but observed to be in lesser extent. As before, coplanar waveguide are observed to excite E-fields comprising of two components of equal magnitude but opposite directions. Next, the current density for DR antenna is investigated. Judging from the current density of the magnetic loop for DR antenna, the magnetic loop is larger than $1\lambda_g$.

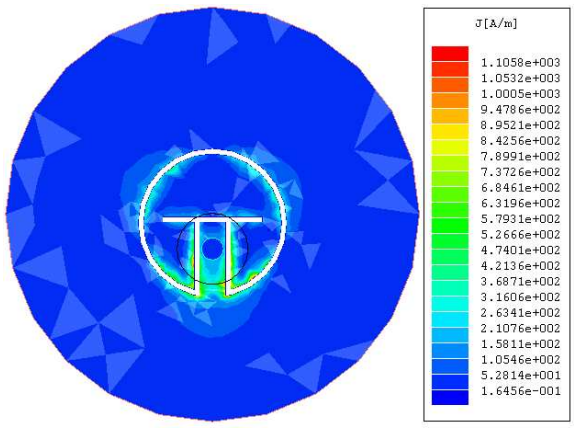

Figure 6.32: Simulated current density for antenna ($\epsilon_r = 38.5$) using Ansoft HFSS (3.60 GHz)

Measurement Results

Based on the design parameters mentioned in the previous section, the antennas are fabricated, measured and presented in this section. Photos of the fabricated antennas are displayed in Figure 6.33 and 6.34.

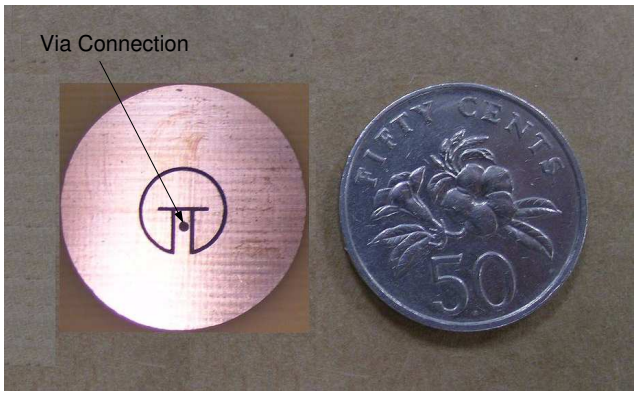

Figure 6.33: Top view of feeding substrate for Cylindrical Dielectric Resonator Antenna ($\epsilon_r = 38.5$)

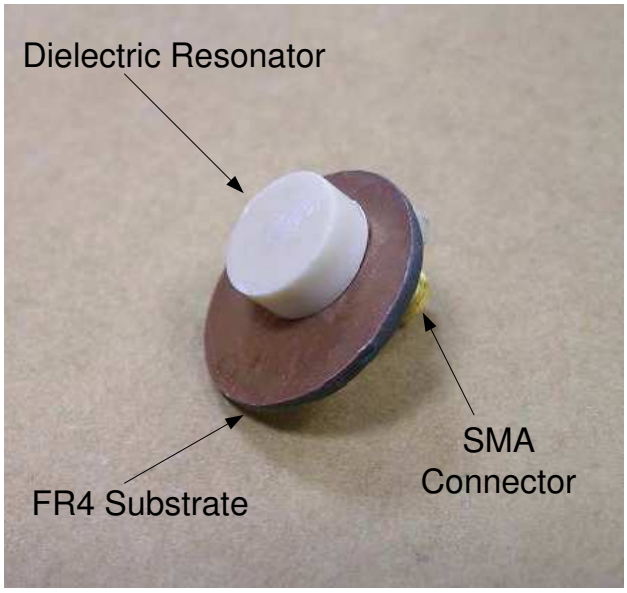

Figure 6.34: Three-dimensional view of Cylindrical Dielectric Resonator Antenna ($\epsilon_r = 38.5$) fabricated

For DR antenna using higher permittivity value, simulated bandwidth ranges from 3.50 to 3.67 GHz. This corresponds to an impedance bandwidth of 4.7%. However, the fabricated antenna can be optimized experimentally to achieve a wide impedance bandwidth of 10% operating in the range from 3.79 to 4.20 GHz. Hence, the complementary pair of magnetic loop and magnetic dipole has shown potential in the design of broadband antenna even for smaller DR antenna using higher permittivity value. As the antenna size becomes smaller, it has been observed to become more sensitive to the environment and can be de-tuned easily. A comparison between simulated and measured return loss for cylindrical DRA using high permittivity are presented in Figure 6.35. The return loss for lower permittivity case is also included in Figure 6.35 for reference purpose. The near-field results for both antennas are summarized in Table 6.11.

Near-Field Measurement		
Permittivity of the Resonator	High ($\epsilon_r = 38.5$)	Low ($\epsilon_r = 10.2$)
Operating Frequency($\|S_{11}\| \geq 10dB$)	3.79 - 4.20 GHz	3.90 - 4.45 GHz
Impedance Bandwidth	0.41GHz (10%)	0.55GHz (13%)
Q-Factor	7.1	5.4

Table 6.11: Summary of near-field results for high and low permittivity dielectric resonator antennas

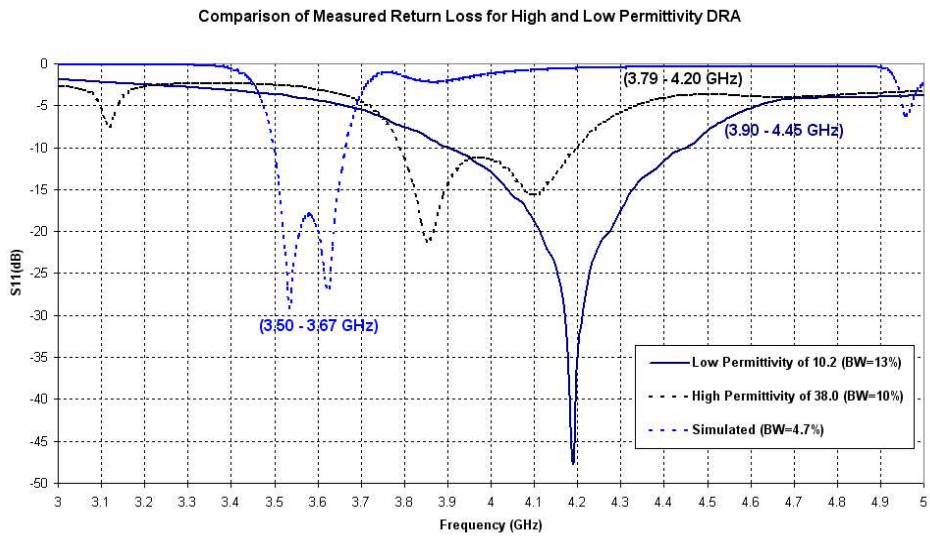

Figure 6.35: Measured Return Loss for Cylindrical Dielectric Resonator Antenna ($\epsilon_r = 38.5$)

Subsequently, far-field measurement of DR antenna ($\epsilon_r = 38.5$) is carried out. The antenna using higher permittivity resonator has a smooth and symmetric radiation patterns. Careful placement of the absorbers is found to be critical for good antenna measurements. DR antenna with $\epsilon_r = 38.5$ has a measured gain of about 3.90dB and is slightly higher than the simulated gain of 3.50dB. The gain of antenna using lower permittivity value of $\epsilon_r = 10.2$ is a slightly higher value of 4.20 dB.

Cross-polarization level for DR antenna using higher permittivity value is noted to be 14dB below its corresponding co-polarization level. The H-Plane 3dB-beamwidth Θ_H is narrower than the lower permittivity case. Hence, the higher permittivity DRA has a higher directivity and a lower radiation efficiency of 80%. This is much lower than the cylindrical DRA, which has a radiation efficiency of 94%. Even though the use of higher permittivity value can achieve miniaturization, it must tolerate a narrower impedance bandwidth, a lower radiation efficiency and higher fabrication sensitivity. A summary of the far-field measurements for different permittivity value

used are tabulated in Table 6.12 for comparison purposes.

Far-Field Measurement		
Permittivity of the Resonator	High ($\epsilon_r = 38.5$)	Low ($\epsilon_r = 10.2$)
E-Plane Co-Polarization(dBi),E_{cPol}	3.78	4.20
E-Plane Cross-Polarization(dB) wrt E_{cPol}	-15.2	-21.2
E-Plane 3dB-Beamwidth(deg),Θ_E	116	115
H-Plane Co-Polarization(dBi),H_{cPol}	3.90	4.24
H-Plane Cross-Polarization(dB) wrt H_{cPol}	-14.2	-17.2
H-Plane 3dB-Beamwidth(deg),Θ_H	82	105
Forward-to-Backward(F/B) Ratio(dB)	6	13
Directivity(dB)	4.65	4.23
Radiation Efficiency(%)	80	94

Table 6.12: Summary of measured radiation patterns

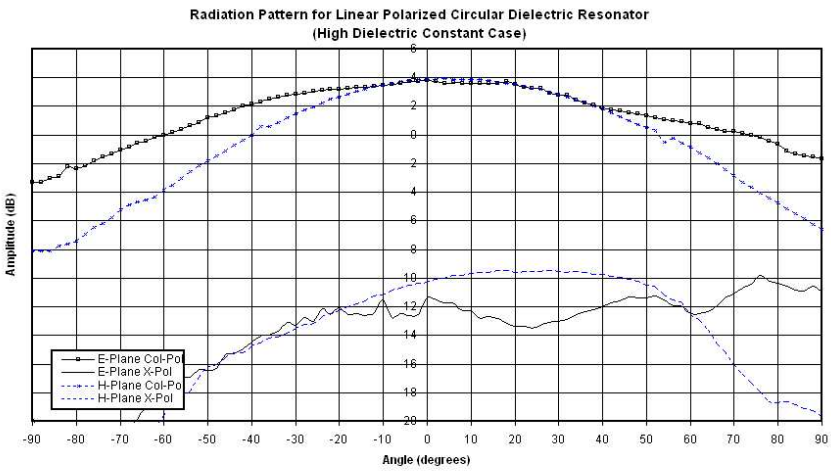

Figure 6.36: Measured far-field radiation pattern at 4.0 GHz for Cylindrical Dielectric Resonator Antenna ($\epsilon_r = 38.5$)

6.3.3 Comparison of Linear and Circular-Polarized Cylindrical Resonator Antennas

Schematics

Design parameters for the circular-polarized dielectric resonator antenna are shown in Figure 6.37. These parameters are optimized results based on *HFSS 8.5*. A summary of the specifications of the dielectric resonator and feeding substrate are presented in Table 6.13. As observed, both dielectric resonators have similar physical dimensions and material properties. This is to ensure a fair comparison of the antenna's performance. The only difference between the linear and circular-polarized antennas lies in the feeding design. To achieve single-feed circular polarization (CP) operation, the use of an inclined coupling slot at 45° [24] has been the popular method. Another way to achieve circular polarization is to use a cross slot of equal slot length [25]. In our analysis, the proposed single-feed CP design comprised of a meandering magnetic dipole. Circular polarization has been achieved by choosing a suitable size of the magnetic dipole length, which results in the excitation of two near-degenerate orthogonal modes of nearly equal amplitudes and 90° phase difference.

Specifications		
Predicted Frequency(GHz)	4.10	
Polarization	Linear	Circular
Resonator Permittivity, ϵ_r	10.2	10.2
Diameter(mm)	24	24
Height(mm)	7.62	7.62
Substrate Permittivity, ϵ_s	2.2	2.2
Substrate thickness, t (mils)	62	62

Table 6.13: Specifications of resonator and substrate used

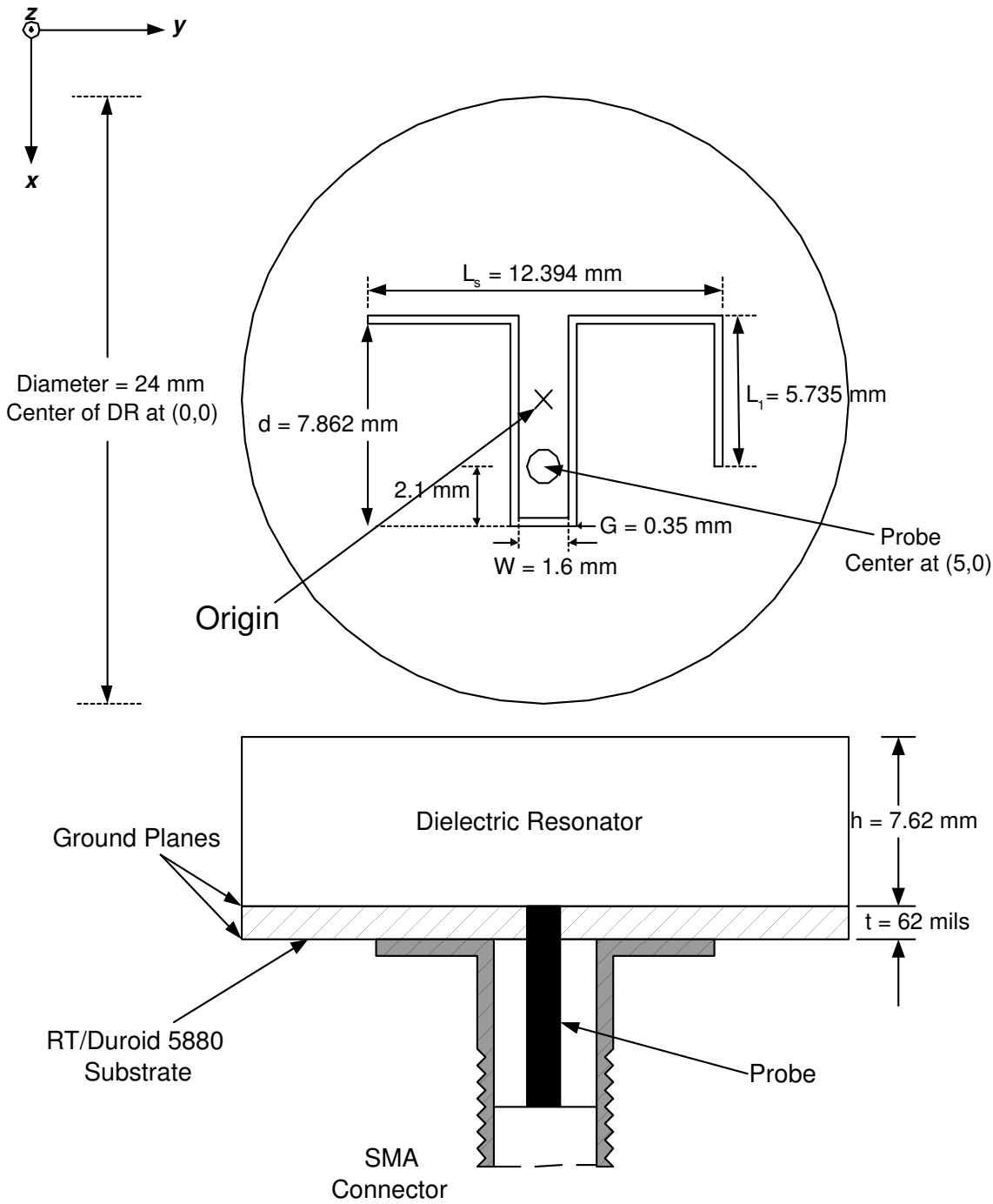

Figure 6.37: Design schematics for circular-polarized cylindrical DRA

Near-Field Analysis

Near-field analysis of the circular-polarized antenna is investigated using *HFSS 8.5* in a similar manner. The simulated E-fields, H-fields and current density are presented and analyzed. The geometry of the antenna structure simulated in *HFSS* is shown in Figure 6.38.

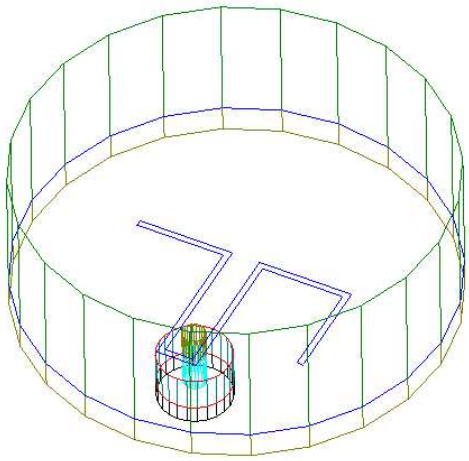

Figure 6.38: Circular-polarized antenna simulated using Ansoft HFSS

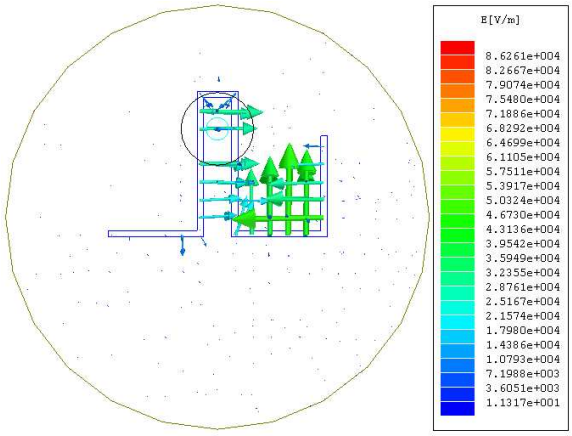

Figure 6.39: E-fields within the rectangular dielectric resonator simulated using Ansoft HFSS (3.88GHz)

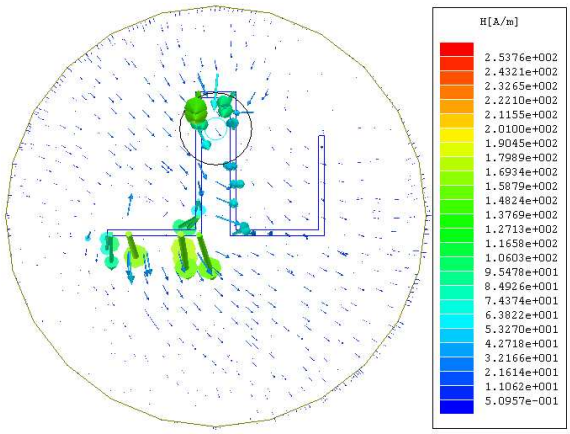

Figure 6.40: H-fields within the circular-polarized antenna simulated using Ansoft HFSS (3.88GHz)

From Figure 6.40, H-fields of the circular-polarized antenna resemble that of the desired $HEM_{11\delta}$. Unlike the H-fields of the linear-polarized antenna (Figure 6.13) which

is along the y-axis, the magnetic field of the circular-polarized antenna is inclined at about 45° to the y-axis. Also, the E-field of the linear-polarized is often in the vertical direction along the x-axis. However, a close observation of E-field for the circular-polarized antenna reveals that vertical and horizontal arms of the meandering dipole result in electric fields existing along x and y-axis together. These fields are responsible for splitting the fundamental resonant frequency of the dielectric resonator into two near-degenerate resonant modes with near-equal amplitudes and 90° phase difference. The position of the probe can also affect the amplitude of the signal and hence need to be positioned carefully.

The simulated current density for the circular polarized antenna is presented in Figure 6.41. Using the effective dielectric constant ($\epsilon_{eff} = 5.53$) obtained earlier, the guided wavelength ($\lambda_g = 32.88mm$) is calculated. Subsequently, the physical dimensions of the meandering magnetic dipole can be expressed in term of its electrical length as shown in Figure 6.42. Adding up all the vertical and horizontal arms, the optimized meandering magnetic dipole has a total length of $1.031\lambda_g$.

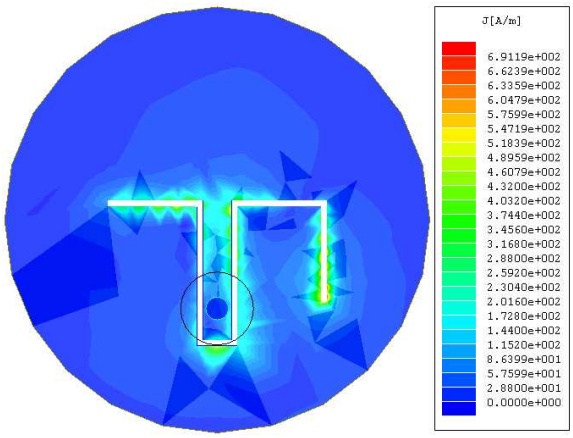

Figure 6.41: Simulated current density for circular-polarized antenna using Ansoft HFSS (3.88GHz)

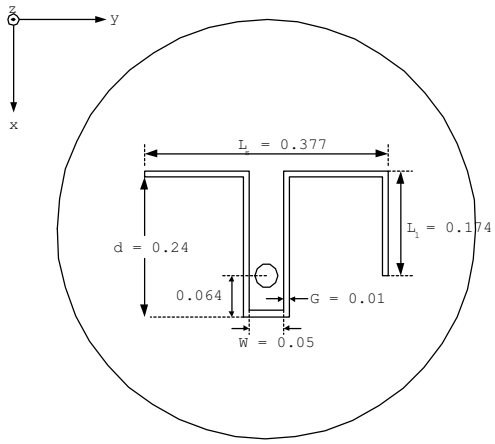

Figure 6.42: Electrical length (in λ_g) of the feed design for circular polarization

Measurement Results

Using the design parameters for the meandering magnetic dipole, the circular-polarized antenna is fabricated, measured and presented. Photos of the fabricated antenna are displayed in Figure (6.43-6.45)

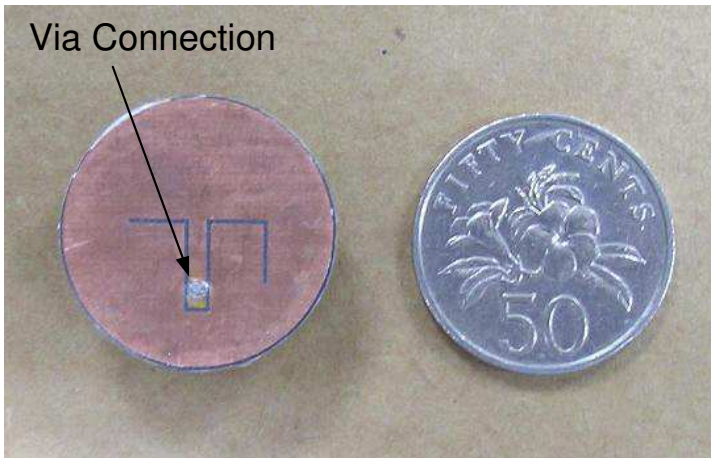

Figure 6.43: Top view of feeding substrate for Cylindrical Dielectric Resonator Antenna (Circular-Polarized)

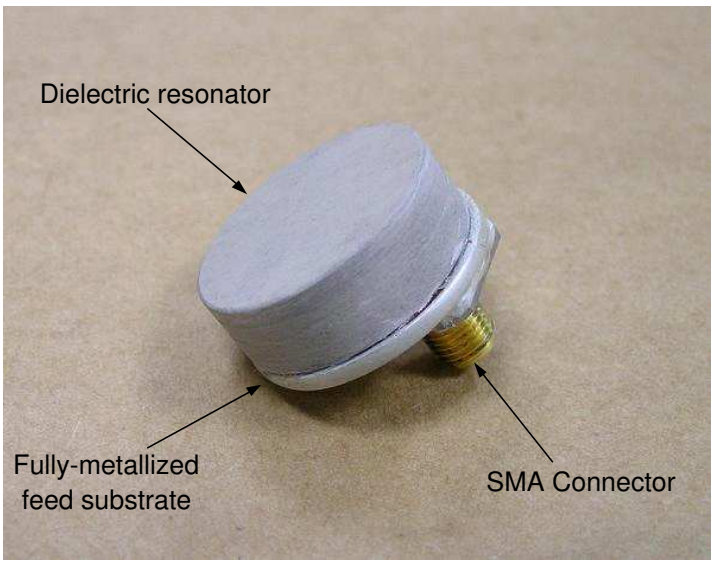

Figure 6.44: Three-dimensional view of Cylindrical Dielectric Resonator Antenna (Circular-Polarized) fabricated

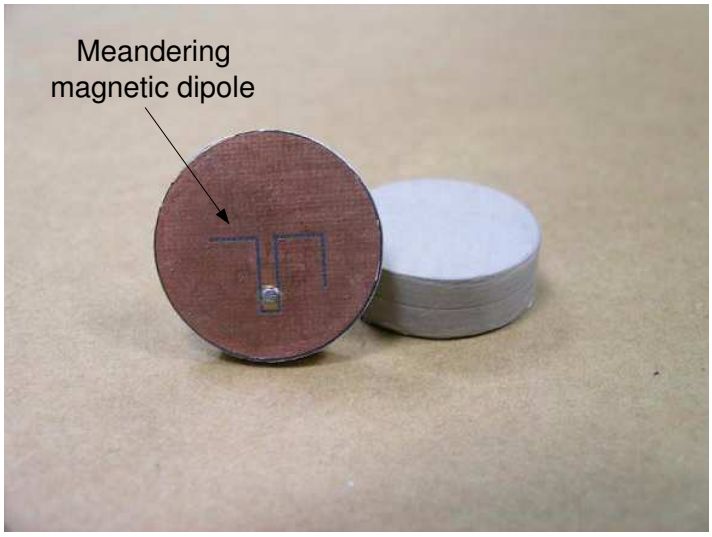

Figure 6.45: Photo showing the meandering magnetic dipole for circular-polarized antenna

The circular-polarized antenna has a simulated impedance bandwidth ranging from 3.60 GHz to 4.10 GHz. This corresponds to an impedance bandwidth of 13%. In contrast, the fabricated antenna has a larger impedance bandwidth of 24%, due to experimental optimization. A comparison of the simulated and measured return loss for the circular-polarized antenna is shown in Figure 6.46. The operating frequency of the antenna falls in the range of 3.41 - 4.36 GHz. On the other hand, the linear-polarized antenna operates in the range of 3.90 - 4.45 GHz and has a bandwidth of 13%. The near-field measurement for linear and circular-polarized antennas are summarized in Table 6.14.

Near-Field Measurement		
Polarization	Linear	Circular
Operating Frequency($\|S_{11}\| \geq 10dB$)	3.90 - 4.45 GHz	3.41 - 4.36 GHz
Impedance Bandwidth	0.50GHz (13%)	0.95GHz (24%)
Q-Factor	5.4	2.9

Table 6.14: Summary of near-field results for linear and circular-polarized dielectric resonator antennas

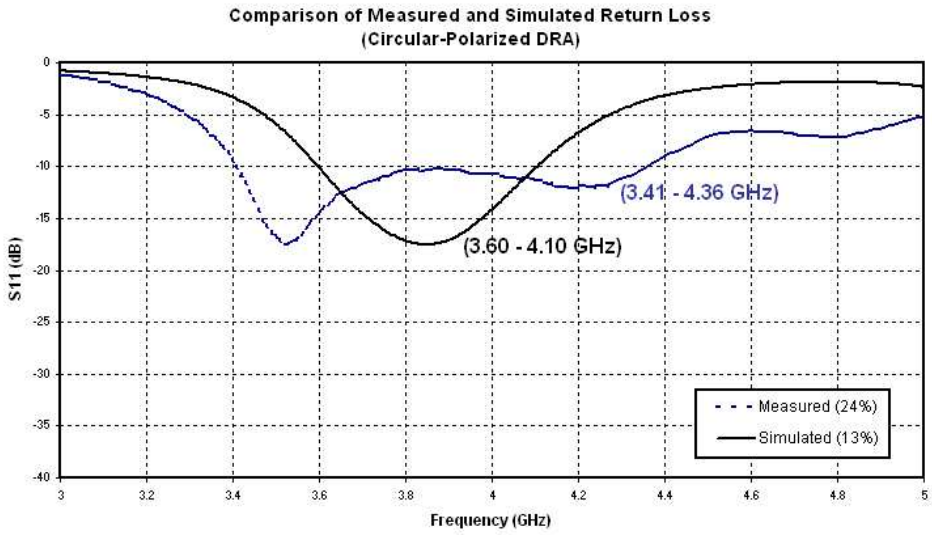

Figure 6.46: Measured return loss for Cylindrical Dielectric Resonator Antenna (Circular-Polarized)

Figure 6.47 shows the measured axial ratio of the CP radiation in the broadside direction. The axial ratio calculation is based on Equation 5.5.1. A large 3-dB CP bandwidth (3.80 - 4.52 GHz) of about 720MHz is obtained. However, as the antenna's impedance bandwidth falls in the range of 3.41 - 4.36 GHz, a bit of compromise in performance is needed to achieve an antenna with a good match ($|S_{11}| < 1/3$) and an acceptable axial ratio within the 3-dB CP bandwidth. Measured radiation patterns are also plotted in Figure 6.48. The E-plane is along the x-z plane while the H-plane is along the y-z plane. The radiation patterns of the circular-polarized antenna are less symmetrical than the linear-polarized antenna. The circular-polarized antenna is observed to have a gain of around 3 dBi in the broadside direction. The front-to-back ratio is measured to be 10.6 dB, which indicates the antenna radiates effectively in the broadside direction. Figure 6.49 shows the antenna gain in the broadside direction against operating frequency. The antenna gain in the range of 3.66 - 4.34 GHz is within 1.0 dB variation. The radiation efficiency for the circular-polarized antenna

(74%) is noted to be much lower than that of the linear-polarized antenna (94%).

A problem to deal with in design of a wide-band antenna is the antenna's radiation patterns. Often, antenna optimized for a wider impedance bandwidth needs to constantly take note of its radiation patterns. From past simulation work, it is observed that antennas usually achieve a wider bandwidth at the expense of a less symmetrical radiation patterns, with lots of scalloping. Even if simulation results show a smooth and symmetrical radiation pattern, the measured one may also suffers from scalloping. In the worst scenario, the antenna has no maximum in the boresight direction.

For the proposed circular-polarized antenna, the radiation patterns measured may have some scalloping but are still symmetrical. It also has the desirable main lobe in the broadside direction. The lower gain and radiation efficiency could be the result of having excite more modes for a wider impedance bandwidth.

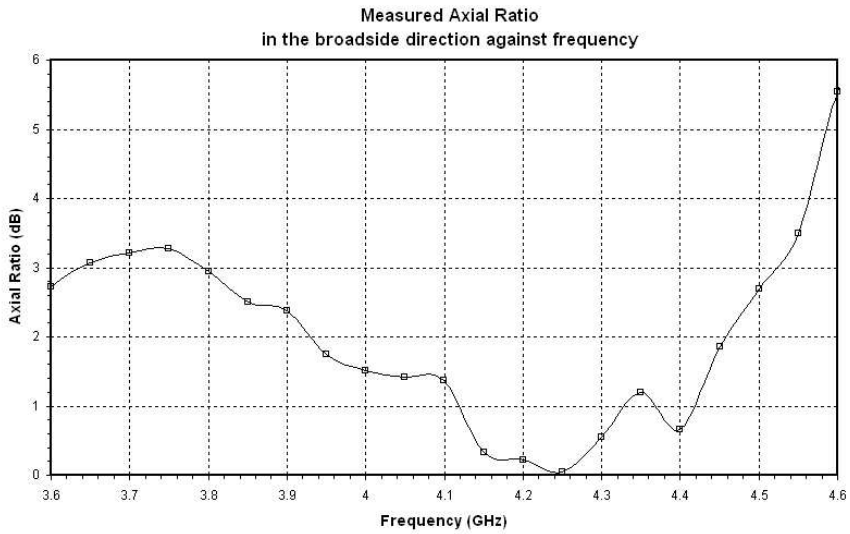

Figure 6.47: Measured axial ratio in the broadside direction against frequency

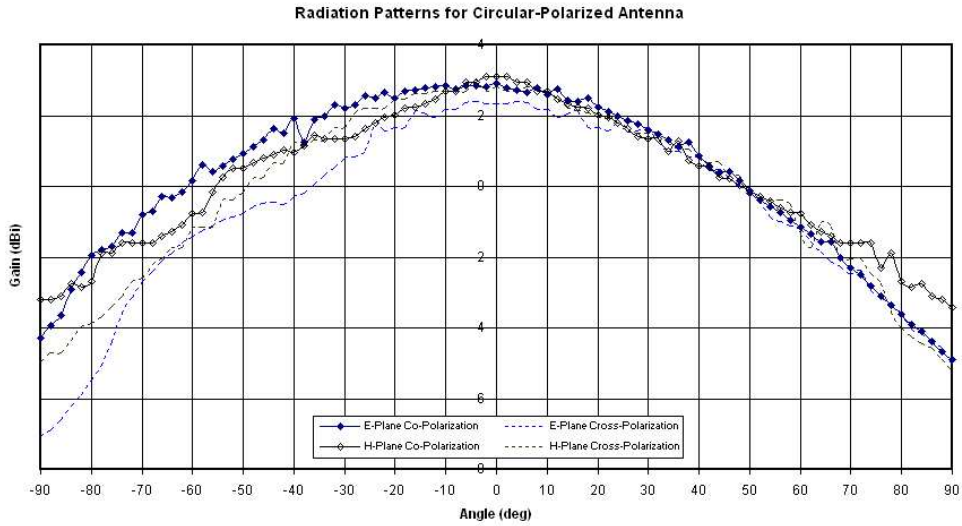

Figure 6.48: Measured radiation patterns for the circular-polarized antenna at 4.20 GHz

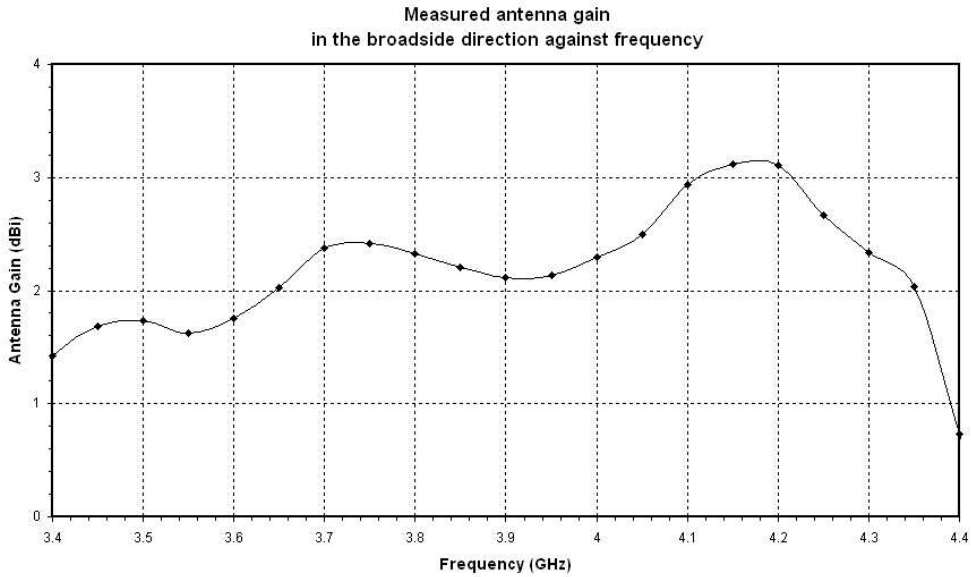

Figure 6.49: Measured antenna gain in the broadside direction against frequency

Far-Field Measurement		
Polarization	Linear	Circular
E-Plane Co-Polarization(dBi),E_{cPol}	4.20	2.93
E-Plane 3dB-Beamwidth(deg),Θ_E	115	112
H-Plane Co-Polarization(dBi),H_{cPol}	4.24	3.11
H-Plane 3dB-Beamwidth(deg),Θ_H	105	102
Forward-to-Backward Ratio(dB)	13.0	10.6
Directivity(dB)	4.23	4.52
Radiation Efficiency(%)	94	74

Table 6.15: Summary of measured radiation patterns for circular-polarized antenna at 4.20 GHz

6.3.4 Comparison of Two Methods for Measurement of DRAs Radiation Efficiency

In this section, two methods for the measurement of antenna radiation efficiency are computed using conventional gain/directivity method (G/D) and Wheeler cap method. Each of these methods was used to measure the efficiency of four different dielectric resonator antennas discussed previously.

The Gain/Directivity Method

One of the most popular way to measure antenna efficiency is to determine the gain G and the directivity D of the antenna. The efficiency η can then be computed as:

$$\eta = \frac{P_{rad}}{P_{in}} = \frac{G}{D} \tag{6.3.1}$$

where P_{rad} is the radiated power and P_{in} is the input power. In this method, the gain of the DR antenna was measured using a standard gain horn and the directivity is calculated from the radiation patterns. The simplest method requires the following procedures:

- Measure the two principal E and H-plane radiation patterns of the test antenna.

- Determine the half-power beamwidths (in degrees) of the E and H-plane patterns.

- Compute the directivity using:

$$D_o = \frac{32,400}{\Theta_E \Theta_H} \tag{6.3.2}$$

This method is a very crude estimation of the antenna's directivity. It is more accurate when the pattern exhibits only one major lobe and its minor lobes are negligible. The other method requires the antenna directivity be calculated from:

$$D = \frac{4\pi F(\theta,\phi)|_{max}}{\int_0^{2\pi}\int_0^{\pi} F(\theta,\phi)\ \sin\theta\ d\theta\ d\phi} \tag{6.3.3}$$

where $F(\theta,\phi)$ function represents the radiation patterns obtained by measurement. $F(\theta,\phi)|_{max}$ refers to the maximum radiation intensity measured and in this case refers to the boresight direction. This method requires tedious integration of the measured radiation patterns but is believed to be accurate for broad beam antennas. Measured radiation patterns are observed to be fairly similar and by assuming the pattern to be symmetrical with respect to ϕ, equation 6.3.3 can be reduced to a simpler form:

$$D = \frac{2F(0,0)}{\int_0^{\pi} F(\theta)\sin\theta d\theta} \tag{6.3.4}$$

The Wheeler Cap Method

This method was originated from Wheeler [26] and is first used by Newman *et al* [27] for measuring efficiency of electrically small loop antennas. This technique has since been popularly used for measuring the radiation efficiency of other electrically small antennas. The experimental set-up is shown in Figure 6.50 where the test antenna is completely enclosed by a metallic cylindrical container. The input impedance of the antenna at resonant frequency is then measured with and without the cap. The real part of the measured input impedance without the cap (R_1) and with the cap (R_2)

are noted and used for the computation of efficiency as follows:

$$\eta = \frac{R_1 - R_2}{R_1} = \frac{R_r}{R_r + R_L} \tag{6.3.5}$$

where R_r and R_L refer to the radiation resistance and radiation loss respectively.

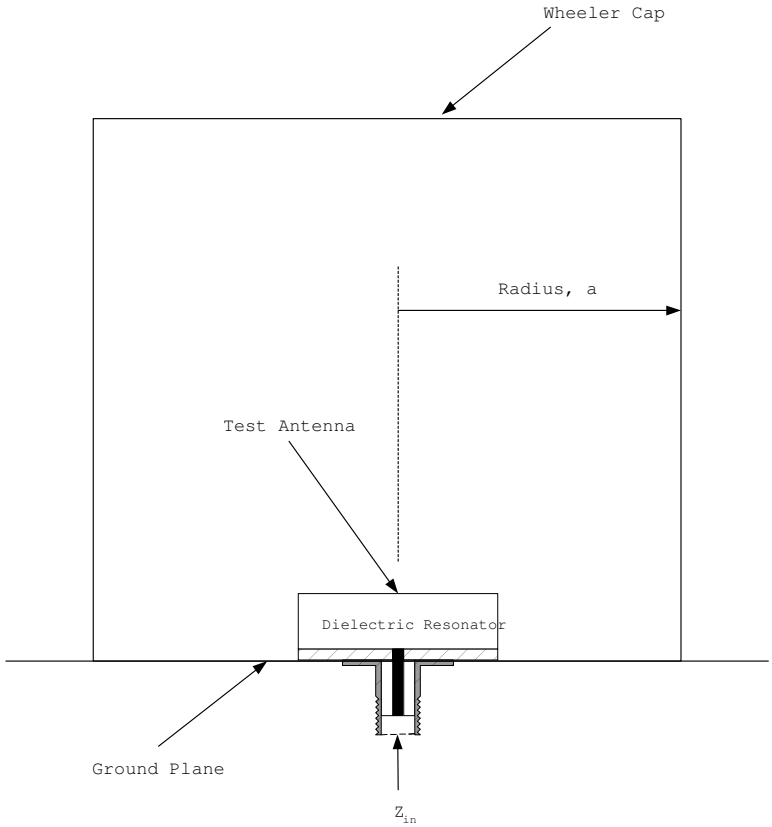

Figure 6.50: Set-up for measuring antenna radiation efficiency using the Wheeler cap method

The metallic cap has an effect of shorting out the radiation resistance, hence allowing R_L to be separated from R_r. It is suggested in Wheeler's paper [26] that a cap radius of about one sixth of a wavelength can be used. However, it was subsequently reported in [27] that the size of the cap and its shape are not so critical. In this investigation, a cylindrical cap with diameter of 21cm is used. It is found during measurement that it is very important to center the cap over the test antenna. In addition, copper tape has been used to ensure the cap are in good contact with the ground plane.

Comparison of Measurement Methods

The computed directivity and radiation efficiency are tabulated in Table 6.16 for comparison.

Case	Directivity (dB)		Radiation Efficiency (%)		
	Method 1	Method 2	Method 1	Method 2	Wheeler Cap Method
	$D_o = \frac{32{,}400}{\Theta_H \Theta_E}$	Gain Integration	G/D	G/D	
(a)	4.29	4.23	98	100	94
(b)	5.32	4.65	72	84	80
(c)	4.81	4.46	83	89	87
(d)	4.53	4.52	72	72	74

Table 6.16: Computed directivity and antenna efficiency using various methods for (a) Linear-polarized Circular DRA (ϵ_r=10.2) (b) Linear-polarized Circular DRA (ϵ_r=38.5) (c) Linear-polarized Rectangular DRA (ϵ_r=10.2) (d) Circular-polarized Circular DRA (ϵ_r=10.2)

From the above table, it is observed that radiation efficiency computed from G/D using method 2 generally gives a higher value than when method 1 is used. The directivity computed using gain integration method is believed to be more accurate then the directivity computed from method 1. However, the gain integration method is more tedious as it requires the use of computers, which can be difficult and time-consuming. The measured radiation patterns also lack repeatability due to the positioning of test antennas on the pedestal mount. The Wheeler cap method is a more popular choice here as it computes the antenna efficiency with more consistency and ease. The evaluated values are found to be generally lower than the ones computed using gain integration method.

Chapter 7

Conclusions and Recommendation for future work

7.1 Conclusions

In this thesis, a novel integrated antenna has been successfully fabricated and measured. The antenna has the advantage of being compact, suitable for Bluetooth (2.45GHz) and other wireless applications. Its fully-metallized substrate prevents RF chip from any interferences. Simulation and measured results have both verified the usefulness of using a complementary pair of magnetic dipole and magnetic loop to achieve wide impedance bandwidth of greater than 10%. The circular-polarized antenna, excited by means of a meandering magnetic dipole has also shown great potential. Measurement results reveal it has a broad 3-dB CP bandwidth of 18% and a wide operational frequency of 24%. The measured radiation patterns for the linear-polarized (LP) and circular-polarized (CP) antennas are symmetrical and smooth. The LP antenna achieved a high radiation efficiency of 94% and illustrate the importance of exciting the antenna close to the natural frequency of the DR.

To compute the resonant frequency of the dielectric resonator accurately, Tangential Vector Finite Element(TVFE) has been proposed. Comparison of computed eigenvalues with measured results reveal that TVFE method can predict eigenvalues to within 1% error. The strength of this method lies mainly in its robustness to

changes in the stated problem. Once the code for TVFE method has been written, changes in the structure analyzed can be easily integrated by means of modifying the mesh generated and redefined the necessary boundary conditions.

7.2 Limitations of TVFE method

The limitations and difficulties encountered in the process of formulating the problem using TVFE method includes:

(i) Extraction of the dielectric resonator's eigenvalues is a tedious process. Even though the computed eigenvalues are free from "spurious" modes, the eigenvalues obtained using TVFE comprised of 'cavity' type modes as well as 'dielectric resonator' type modes. The eigenvalues of the dielectric resonators are obtained by one to one comparison of eigenvalues between an empty cavity and when the DR is placed inside the cavity.

(ii) Radiation Q-factor (Q_{rad}) cannot be computed using this formulation. Eigenvalues of the resonator are obtained by imposing Dirichlet boundary condition on the cavity walls. Q_{rad} cannot be computed unless loss is incorporated in the problem formulation.

(iii) Accuracy of the computed eigenvalues depends much on the quality of the mesh generated. The higher the required accuracy, the more dense the mesh is required to be. The larger the structure, the more will be the number of unknowns. This means a longer computation time and more demanding on the capability of the computer. This problem becomes worst when a very high permittivity resonator which require denser mesh, is required to be analyzed.

7.3 Recommendation for future work

Future works that can be done on this project are as follows:

(i) TVFE method can be improved by imposing perfectly matched layers (PML) on the cavity walls. This would remove eigenvalues of the cavity, leaving behind the desired 'dielectric resonator' type modes. In addition, radiation Q-factor of the dielectric resonator can also be computed.

(ii) Low-profile DR antenna can be implemented. Preliminary simulation results show that low-profile antenna have shown the widest impedance bandwidth, with symmetrical radiation patterns.

(iii) The complementary pair of magnetic loop and magnetic dipole can be exported to design broadband microstrip antenna.

(iv) Active integrated antenna can also be implemented to achieve higher gain performance, yet with a wide operation bandwidth.

References

[1] A. P. Popov and M. D. Rotaru, "A novel integrated dielectric resonator antenna for circular polarization," in *2003 Electronic Components and Technology Conference*, pp. 470–473, 2003.

[2] R. K. Mongia and P. Bhartia, "Dielectric resonator antennas - a review and general design relations for resonant frequency and bandwidth," *International Journal of Microwave and Millimeter-Wave Computer-Aided Engineering*, vol. 4, no. 3, pp. 230–247, 1994.

[3] A. A. Kishk, A. W. Glisson, and J. P. Junker, "Study of broadband dielectric resonators," *Proceedings of the 1999 Antenna Applications Symposium*, pp. 45–68, September 1999.

[4] S. A. Long, M. W. McAllister, and L. C. Shen, "The resonant cylindrical dielectric cavity antenna," in *IEEE Transactions on Antennas and Propagation*, vol. AP-31, pp. 406–412, 1983.

[5] P. Guillon and Y. Garault, "Accurate resonant frequencies of dielectric resonators," in *IEEE Transactions on Microwave Theory and Techniques*, vol. 25, pp. 916–922, November 1977.

[6] A. Chatterjee, J. M. Jin, and J. L. Volakis, "Computation of cavity resonances using edge-based finite elements," in *IEEE Transactions on Microwave Theory and Techniques*, vol. 40, pp. 2106–2108, November 1992.

[7] Z. Wu, G. Drossos, M. A. Jusoh, J. Sha, and L. E. Davis, "Dielectric resonator antennas supported by 'infinite' and finite ground planes," in *10th International*

Conference on Antennas and Propagation, vol. 436, pp. 1486–1489, 14-17th April 1997.

[8] C. T. P. Song, P. S. Hall, H. Ghafouri-Shiraz, and D. Wake, "Packaging technique for gain enhancement of electrically small antenna designed on gallium arsenide," in *Electronics Letters*, vol. 36, pp. 1524–1525, 31st August 2000.

[9] K. P. Esselle, "A low-profile rectangular dielectric resonator antenna," *IEEE Transactions on Antennas and Propagation*, vol. 44, pp. 1296–1297, September 1996.

[10] S. B. Cohn, "Microwave bandpass filters containing high-q dielectric resonators," in *IEEE Transactions on Microwave Theory and Techniques*, vol. MTT-16, pp. 218–227, April 1968.

[11] T. Itoh and R. S. Rudokas, "New method for computing the resonant frequencies of dielectric resonators," in *IEEE Transactions on Microwave Theory and Techniques*, vol. 25, pp. 52–54, January 1977.

[12] R. K. Mongia and A. Ittipiboon, "Theoretical and experimental investigations on rectangular dielectric resonator antennas," *IEEE Transactions on Antennas and Propagation*, vol. 45, pp. 1348–1356, September 1997.

[13] D. Maystre, P. Vincent, and J. C. Mage, "Theoretical and experimental study of the resonant frequency of a cylindrical dielectric resonator," in *IEEE Transactions on Microwave Theory and Techniques*, vol. 31, pp. 846–848, October 1983.

[14] S. Maj and M. Pospieszalski, "A composite multilayered cylindrical dielectric resonator," in *IEEE MTT-S Int. Microwave Symp. Dig., San Francisco*, pp. 190–192, May 1984.

[15] J. V. Bladel, "Resonances of a 'pull-base' dielectric material," in *Proc. European Microwave Conf.,Paris*, pp. 428–432, 1978.

[16] A. W. Glisson, D. Kajfez, and J. James, "Evaluation of modes in dielectric resonators using surface integral equation formulation," in *IEEE Transactions on Microwave Theory and Techniques*, vol. 31, pp. 1023–1029, December 1983.

[17] A. W. Glisson and D. R. Wilton, "Simple and efficient numerical methods for problems of electromagnetic radiation and scattering from surfaces," in *IEEE Transactions on Antennas and Propagation*, vol. 28, pp. 593–603, September 1980.

[18] J. V. Bladel, "On the resonances of a dielectric resonator of very high permittivity," in *IEEE Transactions on Microwave Theory and Techniques*, vol. MTT-23, pp. 199–208, February 1975.

[19] J. Jin, *The Finite Element Method in Electromagnetics*. John Wiley and Sons, second ed., 2002.

[20] R. K. Mongia, C. L. Larose, S. R. Mishra, and P. Bhartia, "Accurate measurement of q-factors of isolated dielectric resonators," *IEEE Transactions on Microwave Theory and Techniques*, vol. 42, pp. 1463–1467, August 1994.

[21] M. Tsuji, H. Shigesawa, and K. Takiyama, "Analytical and experimental investigations on serveral resonant modes in open dielectric resonators," *IEEE Transactions on Microwave Theory and Techniques*, vol. 32, pp. 628–633, June 1984.

[22] D. Kajfez, A. W. Glisson, and J. James, "Computed modal field distribution for isolated dielectric resonators," *IEEE Transactions on Microwave Theory and Techniques*, vol. 32, pp. 1609–1616, December 1984.

[23] B. Lee and W. Choi, "Analysis of resonant frequency and impedance bandwidth for rectangular dielectric resonator antennas," *Antennas and Propagation Society International Symposium*, vol. 4, pp. 2084–2087, July 2000.

[24] K. P. Esselle, "Circularly polarized higher-order rectangular dielectric resonator antenna," *Electronics Letters*, vol. 32, pp. 150–151, Feburary 1996.

[25] T. Vlasits, E. Korolkiewicz, A. Sambell, and B. Robinson, "Performance of a cross-aperture coupled single feed circularly polarized patch antenna," *Electronics Letters*, vol. 32, pp. 612–613, March 1996.

[26] H. A. Wheeler, "The radiansphere around a small antenna," *Proc. IRE*, pp. 1325–1331, August 1959.

[27] E. H. Newmen, P. Bohley, and C. H. Walter, "Two methods for the measurement of antenna efficiency," *IEEE Transactions on Antennas and Propagation*, vol. AP-23, pp. 457–461, July 1975.

Appendix A

Derivations of a_j^e, b_j^e, c_j^e and d_j^e

A.1 Determinant of any order n

In order to derive the unknown coefficients a_j^e, b_j^e, c_j^e and d_j^e, the determinant of the matrix must first be found by the following approach:

$$Determinant\ D = \begin{vmatrix} a_{11} & a_{12} & \cdots & a_{1n} \\ a_{21} & a_{22} & \cdots & a_{2n} \\ \vdots & \vdots & \ddots & \vdots \\ a_{n1} & a_{n2} & \cdots & a_{nn} \end{vmatrix} \tag{A.1.1}$$

for $n \geq 2$:

$$\begin{aligned} D &= a_{j1}C_{j1} + a_{j2}C_{j2} + \cdots + a_{jn}C_{jn} \\ &= \sum_{k=1}^{n} (-1)^{j+k} a_{jk} M_{jk} \quad (j = 1, 2, \cdots, or\ n) \end{aligned} \tag{A.1.2}$$

or

$$\begin{aligned} D &= a_{1k}C_{1k} + a_{2k}C_{2k} + \cdots + a_{nk}C_{nk} \\ &= \sum_{j=1}^{n} (-1)^{j+k} a_{jk} M_{jk} \quad (k = 1, 2, \cdots, or\ n) \end{aligned} \tag{A.1.3}$$

where

$$C_{jk} = (-1)^{j+k} M_{jk} \tag{A.1.4}$$

Hence, using the above method, the volume of the tetrahedral element can be found

as follows:

$$
\begin{aligned}
Volume\ V^e &= \frac{1}{6}\begin{vmatrix} 1 & 1 & 1 & 1 \\ x_1 & x_2 & x_3 & x_4 \\ y_1 & y_2 & y_3 & y_4 \\ z_1 & z_2 & z_1 & z_4 \end{vmatrix} \\
&= \frac{1}{6}\sum_{k=1}^{4}(-1)^{1+k}a_{1k}M_{1k} \\
&= \frac{1}{6}[(-1)^2M_{11} + (-1)^3M_{12} + (-1)^4M_{13} + (-1)^5M_{14}] \\
&= \frac{1}{6}[M_{11} - M_{12} + M_{13} - M_{14}] \qquad \text{(A.1.5)}
\end{aligned}
$$

where

$$
M_{11} = \begin{vmatrix} x_2 & x_3 & x_4 \\ y_2 & y_3 & y_4 \\ z_2 & z_3 & z_4 \end{vmatrix} = x_2(y_3z_4 - y_4z_3) - x_3(y_2z_4 - y_4z_2) + x_4(y_2z_3 - y_3z_2)
$$

$$
M_{12} = \begin{vmatrix} x_1 & x_3 & x_4 \\ y_1 & y_3 & y_4 \\ z_1 & z_3 & z_4 \end{vmatrix} = x_1(y_3z_4 - y_4z_3) - x_3(y_1z_4 - y_4z_1) + x_4(y_1z_3 - y_3z_1)
$$

$$
M_{13} = \begin{vmatrix} x_1 & x_2 & x_4 \\ y_1 & y_2 & y_4 \\ z_1 & z_2 & z_4 \end{vmatrix} = x_1(y_2z_4 - y_4z_2) - x_2(y_1z_4 - y_4z_1) + x_4(y_1z_2 - y_2z_1)
$$

$$
M_{14} = \begin{vmatrix} x_1 & x_2 & x_3 \\ y_1 & y_2 & y_3 \\ z_1 & z_2 & z_3 \end{vmatrix} = x_1(y_2z_3 - y_3z_2) - x_2(y_1z_3 - y_3z_1) + x_3(y_1z_2 - y_2z_1)
$$

A.2 Comparison of Coefficients

Subsequently, the unknown coefficients can be found by expansion of the determinants:

Evaluation of a_j^e:

$$
\begin{aligned}
a^e &= \frac{1}{6V^e}\begin{vmatrix} \phi_1^e & \phi_2^e & \phi_3^e & \phi_4^e \\ x_1^e & x_2^e & x_3^e & x_4^e \\ y_1^e & y_2^e & y_3^e & y_4^e \\ z_1^e & z_2^e & z_3^e & z_4^e \end{vmatrix} \\
&= \frac{1}{6V^e}(a_1^e\phi_1^e + a_2^e\phi_2^e + a_3^e\phi_3^e + a_4^e\phi_4^e) \qquad \text{(A.2.1)}
\end{aligned}
$$

$$
\begin{aligned}
Using\ D &= \sum_{k=1}^{n}(-1)^{j+k}a_{jk}M_{jk} \qquad (Let\ j=1,\ n=4) \\
&= \sum_{k=1}^{4}(-1)^{1+k}a_{1k}M_{1k} \\
&= (-1)^2a_{11}M_{11} + (-1)^3a_{12}M_{12} + (-1)^4a_{13}M_{13} + (-1)^5a_{14}M_{14} \\
&= a_{11}M_{11} - a_{12}M_{12} + a_{13}M_{13} - a_{14}M_{14} \qquad \text{(A.2.2)}
\end{aligned}
$$

where

$$
M_{11} = \begin{vmatrix} x_2^e & x_3^e & x_4^e \\ y_2^e & y_3^e & y_4^e \\ z_2^e & z_3^e & z_4^e \end{vmatrix} = x_2^e(y_3^ez_4^e - y_4^ez_3^e) - x_3^e(y_2^ez_4^e - y_4^ez_2^e) + x_4^e(y_2^ez_3^e - y_3^ez_2^e)
$$

$$
M_{12} = \begin{vmatrix} x_1^e & x_3^e & x_4^e \\ y_1^e & y_3^e & y_4^e \\ z_1^e & z_3^e & z_4^e \end{vmatrix} = x_1^e(y_3^ez_4^e - y_4^ez_3^e) - x_3^e(y_1^ez_4^e - y_4^ez_1^e) + x_4^e(y_1^ez_3^e - y_3^ez_1^e)
$$

$$
M_{13} = \begin{vmatrix} x_1^e & x_2^e & x_4^e \\ y_1^e & y_2^e & y_4^e \\ z_1^e & z_2^e & z_4^e \end{vmatrix} = x_1^e(y_2^ez_4^e - y_4^ez_2^e) - x_2^e(y_1^ez_4^e - y_4^ez_1^e) + x_4^e(y_1^ez_2^e - y_2^ez_1^e)
$$

$$
M_{14} = \begin{vmatrix} x_1^e & x_2^e & x_3^e \\ y_1^e & y_2^e & y_3^e \\ z_1^e & z_2^e & z_3^e \end{vmatrix} = x_1^e(y_2^ez_3^e - y_3^ez_2^e) - x_2^e(y_1^ez_3^e - y_3^ez_1^e) + x_3^e(y_1^ez_2^e - y_2^ez_1^e)
$$

and since

$$a_{11} = \phi_1^e \qquad a_{12} = \phi_2^e$$
$$a_{13} = \phi_3^e \qquad a_{14} = \phi_4^e \tag{A.2.3}$$

we obtain

$$\begin{aligned} D &= \phi_1^e M_{11} - \phi_2^e M_{12} + \phi_3^e M_{13} - \phi_4^e M_{14} \\ \therefore \quad a^e &= \frac{1}{6V^e} D = \frac{1}{6V^e}(a_1^e\phi_1^e + a_2^e\phi_2^e + a_3^e\phi_3^e + a_4^e\phi_4^e) \end{aligned}$$

By comparing of coefficients, the following results are obtained:

$$a_1^e = M_{11} \qquad a_3^e = M_{13}$$
$$a_2^e = -M_{12} \qquad a_4^e = -M_{14} \tag{A.2.4}$$

Evaluation of b_j^e:

$$\begin{aligned} b^e &= \frac{1}{6V^e}\begin{vmatrix} 1 & 1 & 1 & 1 \\ \phi_1^e & \phi_2^e & \phi_3^e & \phi_4^e \\ y_1^e & y_2^e & y_3^e & y_4^e \\ z_1^e & z_2^e & z_3^e & z_4^e \end{vmatrix} \\ &= \frac{1}{6V^e}(b_1^e\phi_1^e + b_2^e\phi_2^e + b_3^e\phi_3^e + b_4^e\phi_4^e) \end{aligned} \tag{A.2.5}$$

$$\begin{aligned} Using\ D &= \sum_{k=1}^{n}(-1)^{j+k} a_{jk} M_{jk} \quad (Let\ j = 2,\ n = 4) \\ &= \sum_{k=1}^{4}(-1)^{2+k} a_{2k} M_{2k} \\ &= (-1)^3 a_{21}M_{21} + (-1)^4 a_{22}M_{22} + (-1)^5 a_{23}M_{23} + (-1)^6 a_{24}M_{24} \\ &= -a_{21}M_{21} + a_{22}M_{22} - a_{23}M_{23} + a_{24}M_{24} \\ &= a_{21}(-M_{21}) + a_{22}M_{22} + a_{23}(-M_{23}) + a_{24}M_{24} \end{aligned} \tag{A.2.6}$$

where

$$
\begin{aligned}
M_{21} &= \begin{vmatrix} 1 & 1 & 1 \\ y_2^e & y_3^e & y_4^e \\ z_2^e & z_3^e & z_4^e \end{vmatrix} = (y_3^e z_4^e - y_4^e z_3^e) - (y_2^e z_4^e - y_4^e z_2^e) + (y_2^e z_3^e - y_3^e z_2^e) \\
M_{22} &= \begin{vmatrix} 1 & 1 & 1 \\ y_1^e & y_3^e & y_4^e \\ z_1^e & z_3^e & z_4^e \end{vmatrix} = (y_3^e z_4^e - y_4^e z_3^e) - (y_1^e z_4^e - y_4^e z_1^e) + (y_1^e z_3^e - y_3^e z_1^e) \\
M_{23} &= \begin{vmatrix} 1 & 1 & 1 \\ y_1^e & y_2^e & y_4^e \\ z_1^e & z_2^e & z_4^e \end{vmatrix} = (y_2^e z_4^e - y_4^e z_2^e) - (y_1^e z_4^e - y_4^e z_1^e) + (y_1^e z_2^e - y_2^e z_1^e) \\
M_{24} &= \begin{vmatrix} 1 & 1 & 1 \\ y_1^e & y_2^e & y_3^e \\ z_1^e & z_2^e & z_3^e \end{vmatrix} = (y_2^e z_3^e - y_3^e z_2^e) - (y_1^e z_3^e - y_3^e z_1^e) + (y_1^e z_2^e - y_2^e z_1^e)
\end{aligned}
$$

and since

$$
\begin{aligned}
a_{21} &= \phi_1^e & a_{22} &= \phi_2^e \\
a_{23} &= \phi_3^e & a_{24} &= \phi_4^e
\end{aligned}
\tag{A.2.7}
$$

we obtain

$$
\begin{aligned}
D &= \phi_1^e(-M_{21}) + \phi_2^e M_{22} + \phi_3^e(-M_{23}) + \phi_4^e M_{24} \\
\therefore \quad b^e &= \frac{1}{6V^e} D = \frac{1}{6V^e}(b_1^e\phi_1^e + b_2^e\phi_2^e + b_3^e\phi_3^e + b_4^e\phi_4^e)
\end{aligned}
$$

By comparing of coefficients, the following results are obtained:

$$
\begin{aligned}
b_1^e &= -M_{21} & b_3^e &= -M_{23} \\
b_2^e &= M_{22} & b_4^e &= M_{24}
\end{aligned}
\tag{A.2.8}
$$

Evaluation of c_j^e:

$$
\begin{aligned}
c^e &= \frac{1}{6V^e}\begin{vmatrix} 1 & 1 & 1 & 1 \\ x_1^e & x_2^e & x_3^e & x_4^e \\ \phi_1^e & \phi_2^e & \phi_3^e & \phi_4^e \\ z_1^e & z_2^e & z_3^e & z_4^e \end{vmatrix} \\
&= \frac{1}{6V^e}(c_1^e\phi_1^e + c_2^e\phi_2^e + c_3^e\phi_3^e + c_4^e\phi_4^e) \qquad \text{(A.2.9)}
\end{aligned}
$$

$$
\begin{aligned}
Using\ D &= \sum_{k=1}^{n}(-1)^{j+k}a_{jk}M_{jk} \quad (Let\ j=3,\ n=4) \\
&= \sum_{k=1}^{4}(-1)^{3+k}a_{1k}M_{1k} \\
&= (-1)^4a_{31}M_{31} + (-1)^5a_{32}M_{32} + (-1)^6a_{33}M_{33} + (-1)^7a_{34}M_{34} \\
&= a_{31}M_{31} + a_{32}(-M_{32}) + a_{33}M_{33} + a_{34}(-M_{34}) \qquad \text{(A.2.10)}
\end{aligned}
$$

where

$$
\begin{aligned}
M_{31} &= \begin{vmatrix} 1 & 1 & 1 \\ x_2^e & x_3^e & x_4^e \\ z_2^e & z_3^e & z_4^e \end{vmatrix} = (x_3^ez_4^e - x_4^ez_3^e) - (x_2^ez_4^e - x_4^ez_2^e) + (x_2^ez_3^e - x_3^ez_2^e) \\
M_{32} &= \begin{vmatrix} 1 & 1 & 1 \\ x_1^e & x_3^e & x_4^e \\ z_1^e & z_3^e & z_4^e \end{vmatrix} = (x_3^ez_4^e - x_4^ez_3^e) - (x_1^ez_4^e - x_4^ez_1^e) + (x_1^ez_3^e - x_3^ez_1^e) \\
M_{33} &= \begin{vmatrix} 1 & 1 & 1 \\ x_1^e & x_2^e & x_4^e \\ z_1^e & z_2^e & z_4^e \end{vmatrix} = (x_2^ez_4^e - x_4^ez_2^e) - (x_1^ez_4^e - x_4^ez_1^e) + (x_1^ez_2^e - x_2^ez_1^e) \\
M_{34} &= \begin{vmatrix} 1 & 1 & 1 \\ x_1^e & x_2^e & x_3^e \\ z_1^e & z_2^e & z_3^e \end{vmatrix} = (x_2^ez_3^e - x_3^ez_2^e) - (x_1^ez_3^e - x_3^ez_1^e) + (x_1^ez_2^e - x_2^ez_1^e)
\end{aligned}
$$

and since

$$
\begin{aligned}
a_{31} &= \phi_1^e & a_{32} &= \phi_2^e \\
a_{33} &= \phi_3^e & a_{34} &= \phi_4^e \qquad \text{(A.2.11)}
\end{aligned}
$$

we obtain

$$\begin{aligned} D &= \phi_1^e M_{31} + \phi_2^e(-M_{32}) + \phi_3^e M_{33} + \phi_4^e(-M_{34}) \\ \therefore \quad c^e &= \frac{1}{6V^e} D = \frac{1}{6V^e}(c_1^e\phi_1^e + c_2^e\phi_2^e + c_3^e\phi_3^e + c_4^e\phi_4^e) \end{aligned}$$

By comparing of coefficients, the following results are obtained:

$$\begin{aligned} c_1^e &= M_{31} & c_3^e &= M_{33} \\ c_2^e &= -M_{32} & c_4^e &= -M_{34} \end{aligned} \tag{A.2.12}$$

Evaluation of d_j^e:

$$\begin{aligned} d^e &= \frac{1}{6V^e} \begin{vmatrix} 1 & 1 & 1 & 1 \\ x_1^e & x_2^e & x_3^e & x_4^e \\ y_1^e & y_2^e & y_3^e & y_4^e \\ \phi_1^e & \phi_2^e & \phi_3^e & \phi_4^e \end{vmatrix} \\ &= \frac{1}{6V^e}(d_1^e\phi_1^e + d_2^e\phi_2^e + d_3^e\phi_3^e + d_4^e\phi_4^e) \end{aligned} \tag{A.2.13}$$

$$\begin{aligned} Using\ D &= \sum_{k=1}^{n}(-1)^{j+k} a_{jk} M_{jk} \quad (Let\ j = 4,\ n = 4) \\ &= \sum_{k=1}^{4}(-1)^{4+k} a_{1k} M_{1k} \\ &= (-1)^5 a_{41} M_{41} + (-1)^6 a_{42} M_{42} + (-1)^7 a_{43} M_{43} + (-1)^8 a_{44} M_{44} \\ &= a_{41}(-M_{41}) + a_{42} M_{42} + a_{43}(-M_{43}) + a_{44} M_{44} \end{aligned} \tag{A.2.14}$$

where

$$
\begin{aligned}
M_{41} &= \begin{vmatrix} 1 & 1 & 1 \\ x_2^e & x_3^e & x_4^e \\ y_2^e & y_3^e & y_4^e \end{vmatrix} = (x_3^e y_4^e - x_4^e y_3^e) - (x_2^e y_4^e - x_4^e y_2^e) + (x_2^e y_3^e - x_3^e y_2^e) \\
M_{42} &= \begin{vmatrix} 1 & 1 & 1 \\ x_1^e & x_3^e & x_4^e \\ y_1^e & y_3^e & y_4^e \end{vmatrix} = (x_3^e y_4^e - x_4^e y_3^e) - (x_1^e y_4^e - x_4^e y_1^e) + (x_1^e y_3^e - x_3^e y_1^e) \\
M_{43} &= \begin{vmatrix} 1 & 1 & 1 \\ x_1^e & x_2^e & x_4^e \\ y_1^e & y_2^e & y_4^e \end{vmatrix} = (x_2^e y_4^e - x_4^e y_2^e) - (x_1^e y_4^e - x_4^e y_1^e) + (x_1^e y_2^e - x_2^e y_1^e) \\
M_{44} &= \begin{vmatrix} 1 & 1 & 1 \\ x_1^e & x_2^e & x_3^e \\ y_1^e & y_2^e & y_3^e \end{vmatrix} = (x_2^e y_3^e - x_3^e y_2^e) - (x_1^e y_3^e - x_3^e y_1^e) + (x_1^e y_2^e - x_2^e y_1^e)
\end{aligned}
$$

and since

$$
\begin{aligned}
a_{41} &= \phi_1^e & a_{42} &= \phi_2^e \\
a_{43} &= \phi_3^e & a_{44} &= \phi_4^e
\end{aligned}
\tag{A.2.15}
$$

we obtain

$$
\begin{aligned}
D &= \phi_1^e(-M_{41}) + \phi_2^e M_{42} + \phi_3^e(-M_{43}) + \phi_4^e M_{44} \\
\therefore \quad d^e &= \frac{1}{6V^e} D = \frac{1}{6V^e}(d_1^e \phi_1^e + d_2^e \phi_2^e + d_3^e \phi_3^e + d_4^e \phi_4^e)
\end{aligned}
$$

By comparing of coefficients, the following results are obtained:

$$
\begin{aligned}
d_1^e &= -M_{41} & d_3^e &= -M_{43} \\
d_2^e &= M_{42} & d_4^e &= M_{44}
\end{aligned}
\tag{A.2.16}
$$

Appendix B

Matlab Codes implementing FEM

B.1 Main

```
Function cavity025

%=======================================================
%Assign nodal values to variables after using GiD mesher
%=======================================================
Global  = load('Global_0.25.txt');
element = load('element_0.25.txt');
G_edge  = load('G_edge025.txt');
fedge   = load('fedge025.txt');

sizeElement = size(element);
sizeGlobal  = size(Global);
sizefedge   = size(fedge);

N_elements = sizeElement(1);
gnodes     = sizeGlobal(1);
num_edge   = sizefedge(1);

%Initialization
%==============
Detm = ones(4);
a    = zeros(1,4);
b    = zeros(1,4);
c    = zeros(1,4);
d    = zeros(1,4);
u    = ones(1,4);
eps  = ones(1,N_elements);
mu   = ones(1,N_elements);
L    = zeros(1,6);
in1  = [1 1 1 2 4 3]; %Contain local node
in2  = [2 3 4 3 2 4]; %Contain local node
in3  = [in1;in2];
I    = in3';
E    = zeros(num_edge); %From the fedge_222.txt
F    = zeros(6);
Ee   = zeros(6);
FF   = zeros(num_edge);
% G_edge(e,k) where k can be 1,2,3,4,5 and 6.

%Loop through all elements:
%==========================
for e=1:N_elements

%Allocate the vaue of the permittivity
%=====================================
```

```
    qe=eps((e));

%Compute the Element matrix entries:
%==================================
%Global(element(e,i),j) where j =1(x-coord), 2(y-coord) and 3(z-coord)
%i = 1(1st Gnode),2(2nd Gnodes),3(3rd Gnodes) and 4(4th Gnodes)
%of eth element
%will give the coordinates of the global nodes.

   %Generate the 4 coordinates for each element
   x1=Global(element(e,1),1);
   x2=Global(element(e,2),1);
   x3=Global(element(e,3),1);
   x4=Global(element(e,4),1);
   x = [x1 x2 x3 x4];

   y1=Global(element(e,1),2);
   y2=Global(element(e,2),2);
   y3=Global(element(e,3),2);
   y4=Global(element(e,4),2);
   y = [y1 y2 y3 y4];

   z1=Global(element(e,1),3);
   z2=Global(element(e,2),3);
   z3=Global(element(e,3),3);
   z4=Global(element(e,4),3);
   z = [z1 z2 z3 z4];

   M_Vol = [u;x;y;z]; %assemble into matrix form
   Dt    = det(M_Vol);%Calculate the determinant of the matrix
   Ve    = Dt/6; %Elemental volume

   %Calculate the length of eth edge
   %================================
   L(1) = sqrt((x1-x2)^2+(y1-y2)^2+(z1-z2)^2);
   L(2) = sqrt((x1-x3)^2+(y1-y3)^2+(z1-z3)^2);
   L(3) = sqrt((x1-x4)^2+(y1-y4)^2+(z1-z4)^2);
   L(4) = sqrt((x2-x3)^2+(y2-y3)^2+(z2-z3)^2);
   L(5) = sqrt((x2-x4)^2+(y2-y4)^2+(z2-z4)^2);
   L(6) = sqrt((x3-x4)^2+(y3-y4)^2+(z3-z4)^2);

   %Evaluate the coefficient values
   %===============================
   a(1) =  x2*(y3*z4-z3*y4)-x3*(y2*z4-z2*y4)+x4*(y2*z3-z2*y3);
   a(2) = -x1*(y3*z4-z3*y4)+x3*(y1*z4-z1*y4)-x4*(y1*z3-z1*y3);
   a(3) =  x1*(y2*z4-z2*y4)-x2*(y1*z4-z1*y4)+x4*(y1*z2-z1*y2);
   a(4) = -x1*(y2*z3-z2*y3)+x2*(y1*z3-z1*y3)-x3*(y1*z2-z1*y2);

   b(1) = -(y3*z4-z3*y4)+(y2*z4-z2*y4)-(y2*z3-z2*y3);
   b(2) =  (y3*z4-z3*y4)-(y1*z4-z1*y4)+(y1*z3-z1*y3);
   b(3) = -(y2*z4-z2*y4)+(y1*z4-z1*y4)-(y1*z2-z1*y2);
   b(4) =  (y2*z3-z2*y3)-(y1*z3-z1*y3)+(y1*z2-z1*y2);

   c(1) =  (x3*z4-z3*x4)-(x2*z4-z2*x4)+(x2*z3-z2*x3);
   c(2) = -(x3*z4-z3*x4)+(x1*z4-z1*x4)-(x1*z3-z1*x3);
   c(3) =  (x2*z4-z2*x4)-(x1*z4-z1*x4)+(x1*z2-z1*x2);
   c(4) = -(x2*z3-z2*x3)+(x1*z3-z1*x3)-(x1*z2-z1*x2);

   d(1) = -(x3*y4-y3*x4)+(x2*y4-y2*x4)-(x2*y3-y2*x3);
   d(2) =  (x3*y4-y3*x4)-(x1*y4-y1*x4)+(x1*y3-y1*x3);
   d(3) = -(x2*y4-y2*x4)+(x1*y4-y1*x4)-(x1*y2-y1*x2);
   d(4) =  (x2*y3-y2*x3)-(x1*y3-y1*x3)+(x1*y2-y1*x2);

   % i and j refer to unknown edges
   for i=1:6
      for j=1:6
         i1 = I(i,1);
```

```
      i2 = I(i,2);
      j1 = I(j,1);
      j2 = I(j,2);
      edgei  = sign(G_edge(e,i));
      edgej  = sign(G_edge(e,j));
      del_Ni = edgei*L(i)*[c(i1)*d(i2)-d(i1)*c(i2) ;
                           d(i1)*b(i2)-b(i1)*d(i2) ;
                           b(i1)*c(i2)-c(i1)*b(i2)]/(6*Ve)^2;
      del_Nj = edgej*L(j)*[c(j1)*d(j2)-d(j1)*c(j2) ;
                           d(j1)*b(j2)-b(j1)*d(j2) ;
                           b(j1)*c(j2)-c(j1)*b(j2)]/(6*Ve)^2;
      Ee(i,j)= 4*Ve*dot(del_Ni,del_Nj);
      E(abs(G_edge(e,i)),abs(G_edge(e,j))) = E(abs(G_edge(e,i)),abs(G_edge(e,j))) + Ee(i,j);
   end;
end;

%Evaluate the Matrix F
%=====================
for i=1:4
   for j=1:4
         fe(i,j)=b(i)*b(j)+c(i)*c(j)+d(i)*d(j);
   end;
end;

f11=fe(1,1);
f12=fe(1,2);
f13=fe(1,3);

f14=fe(1,4);

f21=fe(2,1);
f22=fe(2,2);
f23=fe(2,3);
f24=fe(2,4);

f31=fe(3,1);
f32=fe(3,2);
f33=fe(3,3);
f34=fe(3,4);

f41=fe(4,1);
f42=fe(4,2);
f43=fe(4,3);
f44=fe(4,4);

edge1 = sign(G_edge(e,1));
edge2 = sign(G_edge(e,2));
edge3 = sign(G_edge(e,3));
edge4 = sign(G_edge(e,4));
edge5 = sign(G_edge(e,5));
edge6 = sign(G_edge(e,6));

F(1,1) = edge1*edge1*(L(1))^2*(f22 - f12 + f11)/(360*Ve);
F(1,2) = edge1*edge2*(L(1)*L(2))*(2*f23 - f21 - f13   + f11  )/(720*Ve);
F(1,3) = edge1*edge3*(L(1)*L(3))*(2*f24 - f21 - f14   + f11  )/(720*Ve);
F(1,4) = edge1*edge4*(L(1)*L(4))*(  f23 - f22 - 2*f13 + f12  )/(720*Ve);
F(1,5) = edge1*edge5*(L(1)*L(5))*(  f22 - f24 - f12   + 2*f14)/(720*Ve);
F(1,6) = edge1*edge6*(L(1)*L(6))*(  f24 - f23 - f14   + f13  )/(720*Ve);

F(2,1) = F(1,2);
F(2,2) = edge2*edge2*(L(2))^2*(f33 - f13 + f11)/(360*Ve);
F(2,3) = edge2*edge3*(L(2)*L(3))*(2*f34 - f13 - f14   + f11  )/(720*Ve);
F(2,4) = edge2*edge4*(L(2)*L(4))*(  f33 - f23 - f13   + 2*f12)/(720*Ve);
F(2,5) = edge2*edge5*(L(2)*L(5))*(  f23 - f34 - f12   + f14  )/(720*Ve);
F(2,6) = edge2*edge6*(L(2)*L(6))*(  f34 - f33 - 2*f14 + f34  )/(720*Ve);

F(3,1) = F(1,3);
F(3,2) = F(2,3);
```

```
   F(3,3) = edge3*edge3*(L(3))^2*(f44 - f14 + f11)/(360*Ve);
   F(3,4) = edge3*edge4*(L(3)*L(4))*(f34 - f24 - f13   + f12  )/(720*Ve);
   F(3,5) = edge3*edge5*(L(3)*L(5))*(f24 - f44 - 2*f12 + f14  )/(720*Ve);
   F(3,6) = edge3*edge6*(L(3)*L(6))*(f44 - f34 - f14   + 2*f13)/(720*Ve);

   F(4,1) = F(1,4);
   F(4,2) = F(2,4);
   F(4,3) = F(3,4);
   F(4,4) = edge4*edge4*(L(4))^2*(f33 - f23 + f22)/(360*Ve);
   F(4,5) = edge4*edge5*(L(4)*L(5))*(f23 - 2*f34 -   f22 + f24)/(720*Ve);
   F(4,6) = edge4*edge6*(L(4)*L(6))*(f34 -   f33 - 2*f24 + f23)/(720*Ve);

   F(5,1) = F(1,5);
   F(5,2) = F(2,5);
   F(5,3) = F(3,5);
   F(5,4) = F(4,5);
    F(5,5) = edge5*edge5*(L(5))^2*(f22 - f24 + f44)/(360*Ve);
   F(5,6) = edge5*edge6*(L(5)*L(6))*(f24 - 2*f23 - f44 + f34)/(720*Ve);

   F(6,1) = F(1,6);
   F(6,2) = F(2,6);
   F(6,3) = F(3,6);
   F(6,4) = F(4,6);
   F(6,5) = F(5,6);
   F(6,6) = edge6*edge6*(L(6))^2*(f44 - f34 + f33)/(360*Ve);


   %Assemble the Element matrices F into the Global FEM System:
   %=========================================================
    for i=1:6
      for j=1:6
         FF(abs(G_edge(e,i)),abs(G_edge(e,j))) = FF(abs(G_edge(e,i)),abs(G_edge(e,j))) + F(i,j);
      end;
   end;

end;

%Apply Boundary Conditions
%=========================
%TM modes
iedge    = load('iedge025.txt'); %need bedge1 to generate the result
non_cond = iedge'; Fmatrix  = FF(non_cond,non_cond); Ematrix  =
E(non_cond,non_cond);

eig_squares=eig(Ematrix,Fmatrix);
eig_values_indices=find(eig_squares >=0 );
eig_values=sqrt(eig_squares(eig_values_indices));
eign_values=sort(eig_values)
```

B.2 Define global edges

```
%==============================================================================
%
%This program assign numbering(ROWs of fedge) to each of the elements.
%The algorithm is such that it will not allocate a numbering to the same edge.
%
%==============================================================================

Function fedge025

%Load Files
element = load('element_0.25.txt');

%Initialization
%===============
sizeElement = size(element);
n_ele = sizeElement(1);
nsize = 6*n_ele;
edge  = zeros(nsize,2);; %Use upper limit of 999 first
fedge = zeros(10,2);
temp  = zeros(nsize,2);
elem1 = [1 1 1 2 4 3];
elem2 = [2 3 4 3 2 4];
same  = 0;

%Assign unknown egdes
%====================
i=1;
for e=1:n_ele %6x440 = 2640 => zeros(60,2)

   %Set up the unknown edge elements
    if e==1
    for j=1:6
        edge(i,1)=element(e,elem1(j));
        edge(i,2)=element(e,elem2(j));
        i=i+1;
        end;
   else
      for j=1:6
        temp(i,1)=element(e,elem1(j));
        temp(i,2)=element(e,elem2(j));
        i=i+1;
      end;
      i=i-1;
   end;

   %Compare if the edges are repeated

   if e>1
    %Set up the limits for the looping
      lim1 = i-6;
    lim2 = i-5;
    lim3 = i;

      for p=lim2:lim3

         same=0; %Initialize back to zero
         %Loop through the previous element to see if repetitions occur
         for k=1:lim1

            temp1=temp(p,1);
            temp2=temp(p,2);
            edge1=edge(k,1);
            edge2=edge(k,2);

            if temp1==edge1
```

```
                if temp2==edge2
                    same = 1;
                end;
            end;

            if temp1==edge2
                if temp2==edge1
                    same = 1;
               end;
            end;

         end;
         %same
         if same==0
            edge(p,1)=temp1;
            edge(p,2)=temp2;
         end;
      %Terminate the loop generating the temp variable
    end;
    i=i+1; %Is to ensure the next temp element is assigned
   %For the if Loop
    end;
%For all the element
end;

%To take away rows that are repeated
n = 1;
for k=1:nsize
   if edge(k,1)~=0
      if edge(k,2)~=0
         %if edge(k,1)>=edge(k,2)
            fedge(n,1)=edge(k,1);
            fedge(n,2)=edge(k,2);
            n=n+1;
         %else
         %   fedge(n,1)=edge(k,2);
         %  fedge(n,2)=edge(k,1);
          %  n=n+1;
         %end;
      end;
   end;
end;
edge;
fedge;
tfedge = fedge';
tedge  = edge';

fid = fopen('fedge025.txt','w');
fprintf(fid,'%6i  %6i\n',tfedge);
fclose(fid);

fid = fopen('edge025.txt','w');
fprintf(fid,'%6i  %6i\n',tedge);
fclose(fid);
```

B.3 Global edges for each elements

```
%==============================================================================
%
%This program assign numbering(ROWs of fedge) to each of the elements.
%The algorithm is such that it will not allocate a numbering to the same edge.
%Required fedge1.m to generate fedge_222.txt and edge_222.txt
%
%==============================================================================

Function G_edge025

%Load Files
element = load('element_0.25.txt');
edge    = load('edge025.txt');
fedge   = load('fedge025.txt');

%Initialization
%===============
sizeElement = size(element);
n_ele = sizeElement(1);
nsize = 6*n_ele;
temp  = zeros(nsize,2);
elem1 = [1 1 1 2 4 3];
elem2 = [2 3 4 3 2 4];
G_edge= zeros(6,n_ele);
notfound=0;

I1=size(edge);  %1332 with zeros at rows where repetition of edges occur
I2=size(fedge); %341

i=1;
k=1;
r=1;

for e=1:n_ele
   for j=1:6
    temp(i,1)=element(e,elem1(j));
      temp(i,2)=element(e,elem2(j));
      temp1=temp(i,1);
      temp2=temp(i,2);
      k=1;
      notfound=0;
      %============================
      while notfound==0,
         fedge1=fedge(k,1);
         fedge2=fedge(k,2);
        if temp1==fedge1
            if temp2==fedge2
                G_edge(r,e)=k;
               notfound=1;
               r=r+1;
               if r>6
                  r=1;
               end;
            end;
        end;

        if temp2==fedge1
            if temp1==fedge2
                G_edge(r,e)=-k;
               notfound=1;
               r=r+1;
               if r>6
                  r=1;
               end;
            end;
```

```
         end;
         k=k+1;
         if k>I2(1)
            k=I2(1);
         end;
      end;
      %============================
    i=i+1;
   end;

end;

G_edge;

fid = fopen('G_edge025.txt','w'); %Need to take transpose of this text file
fprintf(fid,'%6i  %6i  %6i  %6i  %6i  %6i\n',G_edge);
fclose(fid);
```

B.4 Edges on the boundary

```
%-----------------------------------------------------------------------------
%This program is written to find edges at the boundary

Function bedge025

%Define the x,y,z limitation of the rect cavity
xlim=[0 1];
ylim=[0 0.5];
zlim=[0 0.75];

%Initialize matrix indices
i=1;
j=1;
k=1;
l=1;
m=1;
p=1;
q=1;
r=1;
same1=0;
same2=0;

Global = load('Global_0.25.txt');
fedge  = load('fedge025.txt');
G1     = size(Global);
G2     = size(fedge);
bnode    = zeros(1,5);
inode  = zeros(1,5);
iedge  = zeros(1,5);
bedge  = zeros(1,5);

ZY1   = zeros(1,5);
ZY2   = zeros(1,5);
ZX1   = zeros(1,5);
ZX2   = zeros(1,5);
XY1   = zeros(1,5);
XY2   = zeros(1,5);

for n=1:G1(1)
%Find Nodes on ZY-Plane
   if Global(n,1)==xlim(1)
      ZY1(i)=n;
      i=i+1;
   end;

   if Global(n,1)==xlim(2)
      ZY2(j)=n;
      j=j+1;
   end;
%Find Nodes on ZX-Plane
   if Global(n,2)==ylim(1)
      ZX1(k)=n;
      k=k+1;
   end;

   if Global(n,2)==ylim(2)
      ZX2(l)=n;
      l=l+1;
   end;
%Find Nodes on XY-Plane
   if Global(n,3)==zlim(1)
      XY1(m)=n;
      m=m+1;
   end;
```

```
   if Global(n,3)==zlim(2)
      XY2(p)=n;
      p=p+1;
   end;

end;

I1=size(ZY1);
I2=size(ZY2);
I3=size(ZX1);
I4=size(ZX2);
I5=size(XY1);
I6=size(XY2);

%Find edges on the boundaries
for e=1:G2(1)

   for j=1:I1(2)
    if fedge(e,1)==ZY1(j)
        same1=1;
      end;
      if fedge(e,2)==ZY1(j)
        same2=1;
      end;
   end;

   if same1~=same2
      same1=0;
      same2=0;
   end;

   for j=1:I2(2)
    if fedge(e,1)==ZY2(j)
        same1=1;
      end;
      if fedge(e,2)==ZY2(j)
        same2=1;
      end;
   end;

   if same1~=same2
      same1=0;
      same2=0;
   end;

   for j=1:I3(2)
    if fedge(e,1)==ZX1(j)
        same1=1;
      end;
      if fedge(e,2)==ZX1(j)
        same2=1;
      end;
   end;

   if same1~=same2
      same1=0;
      same2=0;
   end;

   for j=1:I4(2)
    if fedge(e,1)==ZX2(j)
        same1=1;
      end;
      if fedge(e,2)==ZX2(j)
        same2=1;
      end;
   end;
```

```
   if same1~=same2
      same1=0;
      same2=0;
   end;

   for j=1:I5(2)
    if fedge(e,1)==XY1(j)
        same1=1;
      end;
      if fedge(e,2)==XY1(j)
        same2=1;
      end;
   end;

   if same1~=same2
      same1=0;
      same2=0;
   end;

   for j=1:I6(2)
    if fedge(e,1)==XY2(j)
        same1=1;
      end;
      if fedge(e,2)==XY2(j)
        same2=1;
      end;
   end;

  if same1~=same2
      same1=0;
      same2=0;
   end;

   if same1==1
      if same2==1
        bedge(q)=e;
         q=q+1;
         same2=0;
      end;
      same1=0;
   else
      iedge(r)=e;
      r=r+1;
   end;

end;

%Set up an array containing nodes at the boundary
fid = fopen('iedge025.txt','w');
fprintf(fid,'%6i\n',iedge);
fclose(fid);

fid = fopen('bedge025.txt','w');
fprintf(fid,'%6i\n',bedge);
fclose(fid);
```